Improving Access to Laparoscopic Bilateral Tubal Ligation in LMICs: A Novel Lifting Device with an Integrated Imaging System

ME51035: MSc Thesis

Gijsbertus den Butter

TUDelft

Improving Access to Laparoscopic Bilateral Tubal Ligation in LMICs: A Novel Lifting Device with an Integrated Imaging System

by

Gijsbertus den Butter

to obtain the degree of Master of Science
at the Delft University of Technology,
to be defended publicly on Thursday January 25, 2024 at 14:00 AM CET.

TUDelft

Abstract

Background: Bilateral tubal ligation (BTL) is the most common method of contraception worldwide because it is safe and effective. However, its accessibility remains unequal among women in rural India, in part due to a lack of laparoscopic equipment. Rural hospitals therefore resort to gas insufflation-less laparoscopic surgery (GILLS) because it requires less complex equipment. The pneumoperitoneum is replaced by an abdominal wall lift (AWL) device, but these devices suffer from limitations concerning visibility and working space.

Methods: Initiated by the identified medical needs in rural India, a novel AWL device with an integrated imaging system is designed based on methods from literature and input from local end-users. It is a stainless steel hollow circular hook housing an LED lighting system and a 5 MP camera module. It can be connected to any laptop with a USB-A port. The device substitutes for both the traditional AWL device and currently used laparoscopes. The design is exemplified by a fully functional aluminium prototype used for verification and validation.

Results: The selected camera module is the key technology of this design because it provides state-of-the-art imaging at an unmatched price point. The lighting system used for the prototype does not provide enough light, has an asymmetric illumination distribution, and generates too much heat. A structural strength test showed that the strength of the prototype exceeds the material-adjusted design load by 30%. Furthermore, the prototype is cost-effective, lightweight, compatible with current AWL systems, and has limited waterproofness. User tests with an expert rural surgeon confirmed that this design has the potential to improve surgical outcomes of BTL and other procedures, and can increase access to specialized medical care in rural India.

Conclusions: It is strongly recommended to continue the development of this AWL device. The focus points should be the shape and size of the loop (and related cost-effective production techniques), a new lighting system, and the waterproofness of the device. Collaboration with rural surgeons and local biomedical engineers is crucial for context-driven development and implementation.

Keywords: Gasless Laparoscopy - GILLS - Abdominal Wall Lift Device - LMIC - Global Surgery

Acknowledgements

Completing this MSc thesis marks the culmination of my journey in Mechanical Engineering at the Delft University of Technology, and it is with immense gratitude that I express my appreciation to those who have been involved in this endeavour.

First and foremost, I would like to thank my daily supervisor, Roos Oosting, whose unwavering support and guidance initiated this project. I am also grateful to Jenny Dankelman for seamlessly stepping into the role of my daily supervisor in the latter part of this project. Their guidance and mentorship ensured the smooth progression of my work. I am truly appreciative of their collective efforts.

I owe a debt of gratitude to my parents and brothers for their unyielding support throughout this academic journey. Special thanks go to Jolinda, whose unwavering support made this journey much more manageable. Her belief in me fueled my determination to excel.

I would also like to acknowledge the collaborative spirit of my fellow student, Rafael. Our shared experiences and joint efforts, particularly in setting up and conducting experiments, greatly enriched the research process. I am grateful for the camaraderie and teamwork we developed during this period. Appreciation also goes to the students in the Global Surgery Group for their valuable contributions and collective enthusiasm, creating a stimulating environment.

Lastly, I express my thanks to God for providing strength, wisdom, and perseverance throughout this academic pursuit. In reflection on my journey, I am reminded of Psalm 111:2, "Great are the works of the Lord; they are pondered by all who delight in them."

To everyone who played a part in this journey, your support has been pivotal, and I am sincerely grateful for the impact you have had on the completion of this thesis.

<div align="right">

Gijsbertus den Butter
Delft, January 2024

</div>

Contents

1

Introduction

1.1. Introduction

This MSc thesis is part of the research conducted by the Global Surgery Group, led by Professor Jenny Dankelman and Roos Oosting. The Global Surgery group aims to enhance the availability of minimally invasive surgery (MIS) in low- to middle-income countries (LMICs) through the context-driven design of medical equipment, an approach developed by Oosting et al. (2018) [1].

This MSc thesis was initiated after a local end-user, Indian expert GILLS surgeon J. Gnanaraj, identified the need for a better lift device and better imaging equipment in low-resource settings for gasless laparoscopic tubal ligation procedures. This medical need served as the start of this design project, aiming to address the existing challenges and ultimately resulting in the development of a novel Proof of Technology (POT) prototype.

This introduction will explain the current state of the art of MIS and specifically its application to bilateral tubal ligation (BTL) procedures. These procedures in the context of low-resource settings will be described in the subsequent section, based on Phase 1 of the context-driven design approach. Furthermore, the use of gas insufflation-less laparoscopic surgery (GILLS) technique and the abdominal wall-lifting (AWL) devices necessary for this technique will be described. Together, these five topics provide the background for this thesis project.

1.2. Minimally Invasive Surgery: Laparoscopy

Minimally invasive surgery (MIS) has revolutionized the field of surgery in high-income countries (HICs) since it was first performed in 1987 by Philippe Mouret [2]. MIS minimizes the trauma inflicted on patients during surgical procedures while ensuring optimal clinical outcomes. This transformative paradigm of MIS has redefined surgical practices in many medical disciplines, such as laparoscopic surgery, neurosurgery, orthopaedic surgery, and thoracic surgery [3]. The following section will explain the concept of laparoscopic surgery (also called laparoscopy).

Laparoscopy refers to all minimally invasive surgeries within the abdominopelvic cavity. Some common laparoscopic procedures are cholecystectomy (gallbladder removal), appendectomy (appendix removal), and adrenalectomy (adrenal gland removal). Four small keyhole incisions of 10 [mm] suffice to perform these procedures, which is in great contrast to the 200 [mm] midline incision required in traditional laparotomy (open surgery).

The hallmark of laparoscopy lies in its ability to achieve comparable therapeutic efficacy to traditional open surgery, while simultaneously offering numerous clinical benefits. These clinical benefits are well-documented and include reduced postoperative pain, shorter hospital stays, and faster recovery times. The smaller incisions result in less blood loss, reduced risk of infection, and minimized scarring. Patients undergoing laparoscopic procedures often experience less trauma to surrounding tissues and organs, leading to fewer complications, improved clinical outcomes, and better overall patient satisfaction. [4, 5, 6, 7]

Before the start of a conventional laparoscopic procedure, the patient must be prepared. The preparation consists of the four following steps, which are also shown in Figure 1.1.

1. The patient is placed on a surgical table in the Trendelenburg position, supine on the table with their head declined below their feet at a small angle. The patient is then put under general anaesthesia and intubated, which ensures the patient is unconscious and does not experience pain or discomfort throughout the procedure.

2. Surgeons access the abdominopelvic cavity and introduce carbon dioxide gas to inflate the abdomen to approximately 15 mmHg, using specialised instruments like the Veress needle pictured in Figure 1.1 (between steps 1 and 2). The carbon dioxide gas helps create a working space by pushing the abdominal wall away from the organs, also known as pneumoperitoneum.

3. Trocars, which act as gas-tight ports, are introduced in three or four small incisions. The trocars typically have an inner diameter of 5-15 [mm]. The surgeon starts with a small incision near the umbilicus, known as the primary incision or supraumbilical port.

4. The laparoscope is inserted first through the primary incision. It comprises a camera and light source at the tip of a 10 [mm] tube, and transmits high-quality images to a monitor. Under direct vision of the laparoscope, the other ports are placed and specialized instruments are inserted through these ports to perform the surgery.

The instruments used are grasping tools, scissors, staplers, electrocautery devices, or suction-irrigation devices. These instruments are specifically designed for laparoscopy, with long 5 or 10 [mm] shafts and miniaturised tip mechanisms to accommodate the inner diameter of the trocars. Their complexity makes these instruments expensive even by HIC's standards [8].
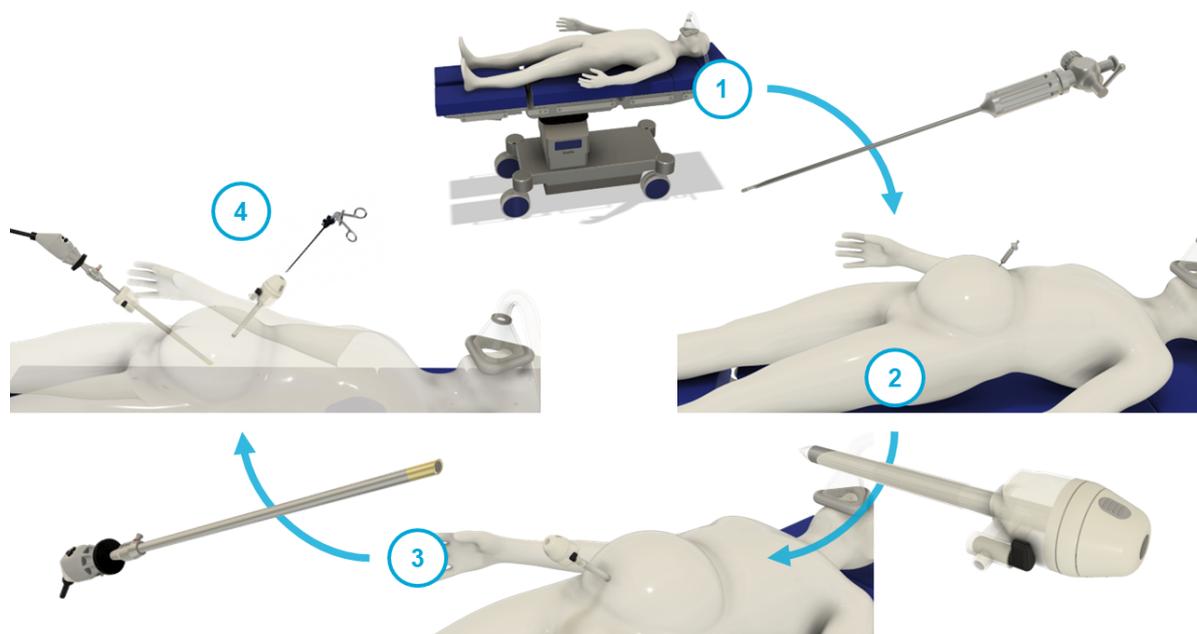
Figure 1.1: Rendered view of the four main steps of the preparation for conventional laparoscopic surgery:
1) Patient is put under general anaesthesia at the start of the procedure.
2) Abdomen is inflated with carbon dioxide gas using a Veress needle.
3) Trocars are introduced into the inflated abdomen through small incisions.
4) The laparoscope and hand instruments are inserted through the trocars.

The surgeon manipulates these instruments through the trocars to perform the surgery while watching the magnified images from the laparoscope on the monitor, allowing for precise movements. A typical surgeon's position during laparoscopy is shown in Figure 1.2 [1]. After the completion of the laparoscopic procedure, any removed tissue or organs may be extracted from the abdomen through the

---

[1]https://vigoshospital.com/laparoscopic-surgery/

trocars. The carbon dioxide gas is then released from the abdominopelvic cavity, and the trocars are removed under direct visualization. The incisions are closed using sutures, clips, or adhesive strips.
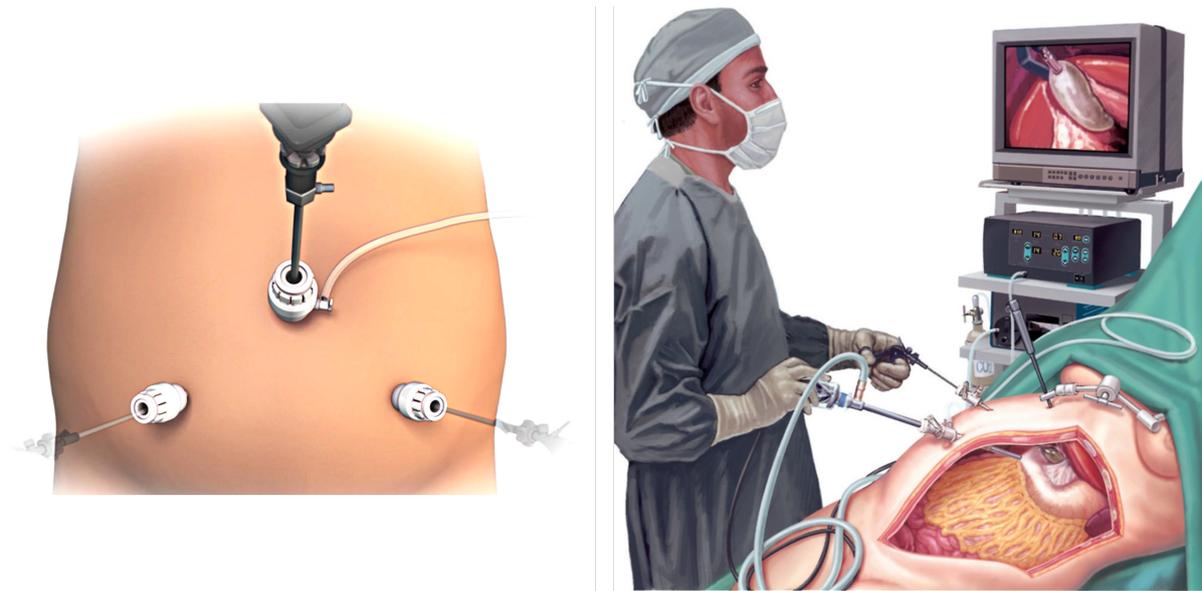
Figure 1.2: Illustration of trocar placement during laparoscopic surgery (left) and surgeon position whilst performing laparoscopic surgery (right). The surgeon's right hand holds the laparoscope, images whereof are shown on the monitor.[1] Note that contrary to this illustration, laparoscopic procedures are usually performed by two surgeons.

1.3. Laparoscopic Bilateral Tubal Ligation

Bilateral tubal ligation (BTL) is the procedure of focus in this thesis. Bilateral in BTL means that both Fallopian tubes are permanently occluded, and it is the most common method of contraception worldwide [9, 10]. The current state of the art is to perform BTL laparoscopically, as it is immediately effective and allows a rapid return to activity [11].

BTL is a relatively simple procedure and can be classified as minor surgery. The working principle is shown in Figure 1.3 [2]. Before the start of a tubal ligation procedure, preparatory steps are taken as described in Section 1.2. Anaesthesia is typically general, after which the abdomen is inflated to introduce the laparoscope and hand instruments used for the occlusion through the inserted trocars. The laparoscope is always placed near the umbilicus, whereas the hand instruments are usually inserted at a point lower on the abdomen. The surgeon may employ various techniques to occlude the Fallopian tubes, such as placing clips or rings on the tubes, cutting, tying, or cauterizing the tubes with an electrical current using electrosurgery.

By physically obstructing both Fallopian tubes, BTL prevents the eggs released by the ovaries from reaching the uterus, thereby preventing fertilization and subsequent pregnancy. However, BTL does not negatively impact the menstrual cycle or hormone production. BTL is considered a highly reliable form of contraception. The risk of failure varies by technique, with the cumulative 10-year probability of pregnancy highest for spring clips ($36.5/1000$ procedures), then cauterisation ($24.8/1000$), and lowest for silicone bands ($17.7/1000$) [12]. Laparoscopic BTL is considered a safe procedure, with low rates of mortality ($1\text{-}2/100000$) and major complications ($0.9/100$), most of which are caused by hypoventilation and cardiopulmonary arrest while administering general anaesthesia [11].

---

[2]https://hhma.org/healthadvisor/aha-fsterl-art/
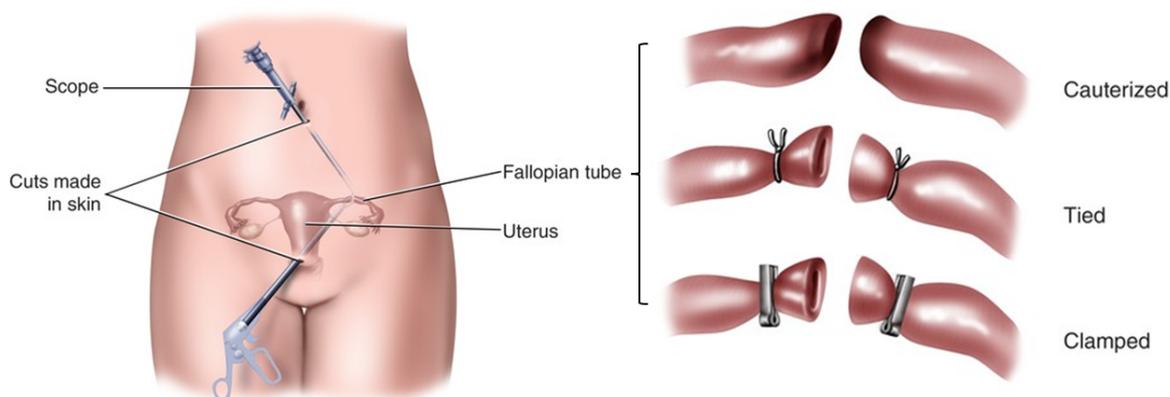
Figure 1.3: Illustration of laparoscopic tubal ligation.[2] Two instruments suffice for this procedure, with the scope always placed at the umbilicus. There are multiple ways to occlude the Fallopian tubes, three of which are shown on the right.

1.4. Context in LMICs: India

BTL is the most common method of contraception worldwide because it is safe and effective, yet its accessibility remains unequal among women globally [13]. 155 million women of reproductive age in LMICs who want to avoid pregnancy do not have access to any form of modern contraception [14]. This unavailability of modern contraception is causally related to the economic development of countries. The proportion of women of reproductive age without access to modern contraception is 14% in upper-middle-income countries, 31% in lower-middle-income countries, and 51% in low-income countries [15]. As a result, 43% of the estimated 206 million pregnancies in LMICs are unintended, and women with an unmet need for modern contraception account for 84% of these unintended pregnancies [15].

Promoting the use of effective and less user-dependent modern contraception, such as permanent methods, could substantially reduce maternal mortality in LMICs [16]. This confirms the need for increased access to BTL in LMICs, and specifically laparoscopic BTL because the distinct advantages of laparoscopy over open surgery may be even more pronounced in LMICs [17]. The primary benefit lies in significantly shorter postoperative hospital stays, which may be crucial in LMICs where families heavily rely on a single-wage earner. Additionally, laparoscopic procedures minimize the risk of infections, which is particularly important in LMICs where the spread of bacteria and viruses is more prevalent.

Women in rural India, the LMIC region of focus, also suffer from limited access to tubal ligation services [18]. The specific context of laparoscopic BTL procedures in India that will be considered during this thesis is described in the following subsections. It serves as input for the problem definition in Chapter 2 and the design specifications in Chapter 3.

Barriers encountered

Several significant barriers hinder the widespread implementation of laparoscopic tubal ligation in rural regions. On a cultural level, misconceptions about tubal ligation, concerns about its permanence, fear of surgical procedures, perceived side effects, religious beliefs, and partner disapproval prevent women from getting BTL [14]. On a structural level, lack of equipment, untrained staff, inaccurate information from healthcare providers, and financial costs form the most significant barriers [19].

This thesis concentrates on the structural barriers that hinder the widespread implementation of laparoscopic BTL in rural India. Rural hospitals struggle with infrastructure, personnel, equipment, and supplies [20]. The high costs of equipment hinder access, and maintenance is challenging. Accreditation requirements based on high-income standards make it difficult for rural hospitals to meet the necessary standards, exacerbating the access gap. Despite these challenges, rural practitioners have found innovative solutions, but lack of formal assessment and research capacity hinder widespread adoption [21].

The high costs of laparoscopic procedures are mainly caused by the high upfront cost of laparoscopic equipment. Indian rural hospitals face a lot of pressure to keep the cost per procedure low

because out-of-pocket payments (OOPs) are still the major source of healthcare spending [22], also for BTL procedures in India [23]. Well-meant donations of surgical equipment do not solve this problem either because the technology from HICs does not fit the resources and services available in the low-resource setting. Consequently, an estimated 70% of medical equipment donated from HICs does not work in rural hospitals according to the World Health Organization (WHO) [24].

Availability of medical equipment is limited by inadequate access to maintenance and spare parts, and a lack of consumables [25]. For example, rural healthcare facilities struggle to source items such as air filters and CO_2 gas to enable laparoscopic surgery. Even necessities such as access to clean water and reliable electricity supply might be lacking, exacerbating the challenges faced in these settings. Consequently, hospitals in rural India are limited in their ability to provide effective laparoscopic surgical interventions.

Structure of the healthcare system

India is the world's most populous country with approximately 1.4 billion people[3]. It is classified as a lower-middle income country by the World Bank[4], and is a recipient of Official Development Assistance (ODA)[5]. Approximately 70% of the population live in rural areas and as such rely on one of India's 33.662 rural hospitals for medical care [26].

These rural hospitals suffer most from the aforementioned structural barriers yet women in rural India are most likely to opt for permanent sterilisation [27]. Data shows that Indian rural hospitals are vital in providing permanent sterilisation services to a large part of the population[28]. They are increasingly starting to offer laparoscopy as a method of surgery for BTL to improve the safety of the procedures. This leads to the focus of this thesis, which is laparoscopic BTL procedures in rural hospitals in India.

Aspects of safe surgery

This section inventories the four aspects of safe surgery as outlined in the roadmap for context-driven design: team, surgical equipment, infrastructure, and operating theatre processes [1]. Determining the availability of these aspects in the local context of laparoscopic BTL procedures in rural hospitals in India will augment the design requirements.

Interviews revealed that the average surgical team in Indian rural hospitals during minor laparoscopic procedures consists of a single surgeon and one or two nurses who act as operating assistants. The nurses typically have not learned about laparoscopy during their education. The presence of anesthesiologists or biomedical engineering technicians is a rarity in these settings and is only found in larger urban hospitals.

The surgical teams have only limited access to laparoscopic equipment and associated supplies. Most often an older or improvised model laparoscope is present. Since 2018, some studies have been published on the design of laparoscopic equipment for use in low-resource settings. Most of these studies focus on the imaging system because that is the most expensive piece of laparoscopic equipment. An overview of these studies is shown in Figure 1.4.

However, other laparoscopic equipment is scarce, basic, and sometimes even improvised. Moreover, disposable items are re-used multiple times [21]. Specialised laparoscopic hand instruments are not available hence surgical teams must work with hand instruments originally intended for open surgery. Gas insufflators and the required CO_2 gas are often not available either. In response, rural hospitals have adopted gas insufflation-less laparoscopic surgery (GILLS) as it works better with traditional instruments and does not require gas insufflation, as will be explained in Section 1.5.

The infrastructure is typical of low-resource settings. Most Indian rural hospitals have access to water, but the quality and cleanliness are not guaranteed. The electricity network is often unstable. A minority of the hospitals have backup generators; however, these generators only power a few critical areas of the hospital and their voltage peaks can cause damage to equipment [29].

---

[3] https://www.un.org/development/desa/dpad/publication/un-desa-policy-brief-no-153-india-overtakes-china-as-the-worlds-most-populous-country/
[4] https://datahelpdesk.worldbank.org/knowledgebase/articles/906519-world-bank-country-and-lending-groups
[5] https://www.oecd.org/dac/financing-sustainable-development/development-finance-standards/daclist.htm

Most Indian rural hospitals have no access to one or several operating theatre processes. As mentioned in the description of the team, often no maintenance processes are in place. No dedicated storage space is present, and equipment is stored on the floor or room-side tables. Sterilisation is done with heavy chemicals such as Cidex and only seldom using an autoclave. General anaesthesia is also not available in most Indian rural hospitals as it requires specialised equipment and the presence of a trained anesthesiologist.
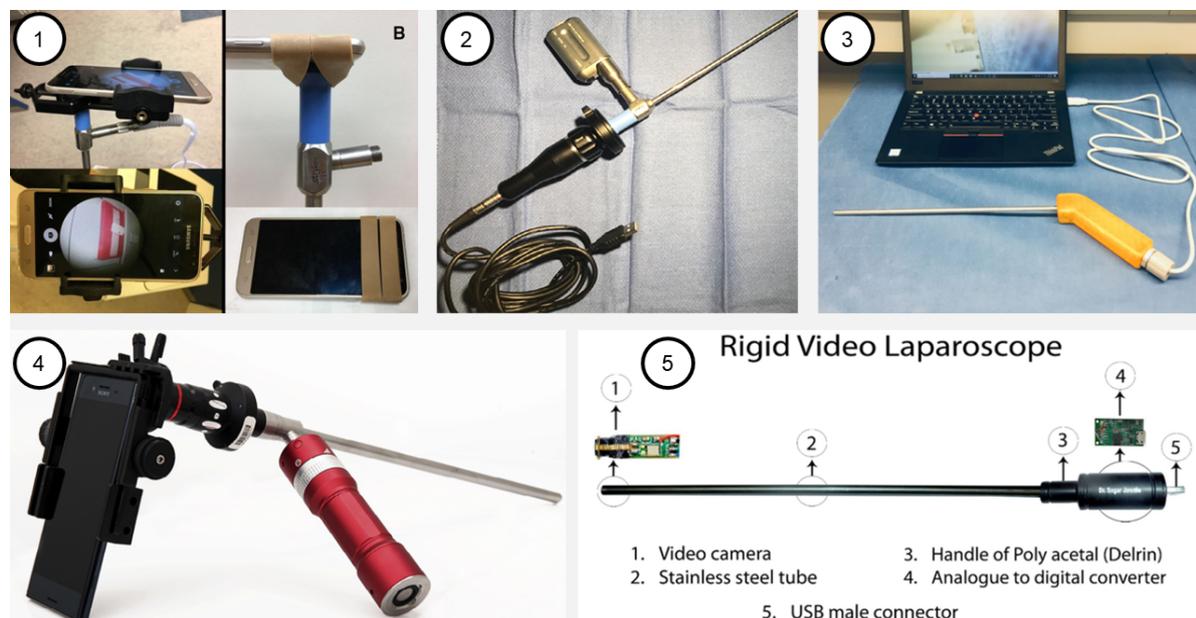
Figure 1.4: An overview of the current research on laparoscopes designed for use in rural hospital settings:
1) Affordable Laparoscopic Camera System (ALCS) consisting of a Stryker telescope and a Samsung Galaxy J3. [30]
2) A low cost rapidly deployable minimally invasive surgical system (RDMIS) that uses a USB-compatible camera. [31]
3) The ReadyView laparoscope, consisting of an integrated camera and LED light source compatible with any laptop. [32]
4) Laparoscope created by coupling a $0°$ 10-mm telescope via a commercially available adapter with an Apple iPhone 6s. [33]
5) Rigid video laparoscope combining the telescope, light source and camera into one low-cost device. [34]

1.5. Gas Insufflation-less Laparoscopic Surgery

In the face of the barriers to laparoscopic BTL, some rural hospitals in India have resorted to Gas Insufflation-less Laparoscopic Surgery (GILLS) as an alternative approach to the traditional laparoscopic surgery technique [35]. GILLS eliminates the need for pneumoperitoneum, the process of inflating the abdominal cavity with carbon dioxide gas (step 2 in Figure 1.1), which is a standard practice in conventional laparoscopy.

Instead of insufflation, GILLS relies on abdominal wall-lifting (AWL) devices to create the required working space in the abdominopelvic cavity. Figure 1.5 [6] shows the basic principle of GILLS, using a circular hook lift device. After the insertion of the circular hook, the abdominal wall is simply lifted to create a working space for the surgeon. The surgery can then be performed similarly to conventional laparoscopy, by creating extra ports for the laparoscope and other instruments.

It is important to note that GILLS has limitations compared to conventional laparoscopic surgery, such as increased technical difficulty, poorer visualization, and longer operative times. Early research conducted in HICs concluded that GILLS had no real benefits over conventional laparoscopy and had some clear disadvantages, which was a long-held view in the MIS community [36, 37].

However, more recently the benefits of this technique for low-resource settings have received more attention and research is being done on designing lifting devices [38, 39]. Several studies remark that if conventional gas laparoscopy is accessible, it should be the standard of care, but for surgeons who do not have access to gas laparoscopy, GILLS remains a viable alternative [39, 40].

---

[6]https://the-14.com/five-billion-people-cant-afford-surgery-a-team-of-innovators-could-soon-change-this/

GILLS offers several advantages over conventional laparoscopy in low-resource settings. Firstly, GILLS eliminates the need for an insufflation system and gas supply. This not only reduces the cost of the procedure but also eliminates having to constantly monitor and replenish the supply of carbon dioxide gas. Moreover, it avoids the complications associated with carbon dioxide insufflation, such as respiratory compromise, ametabolic acidosis, hypoxemia, and hypercapnia [41]. GILLS also eliminates the potential for gas embolism, a rare but potentially life-threatening complication where carbon dioxide gas enters a blood vessel, obstructing blood flow and causing tissue ischemia [42].

Secondly, GILLS requires less expensive equipment compared to traditional laparoscopy. GILLS is compatible with standard hand instruments, designed for open surgery, whereas conventional laparoscopy requires specialised laparoscopic hand instruments as described in Section 1.2 [43].

Thirdly, the use of pneumoperitoneum during conventional laparoscopy requires general anaesthesia [44]. In contrast, spinal anaesthesia suffices for GILLS. The advantage is that spinal anaesthesia can be carried out by the operating surgeon, removing the need for a specialist anaesthetist, and does not require the logistics of providing anaesthetic gasses. GILLS thereby broadens the accessibility of laparoscopic surgery in low-resource settings.
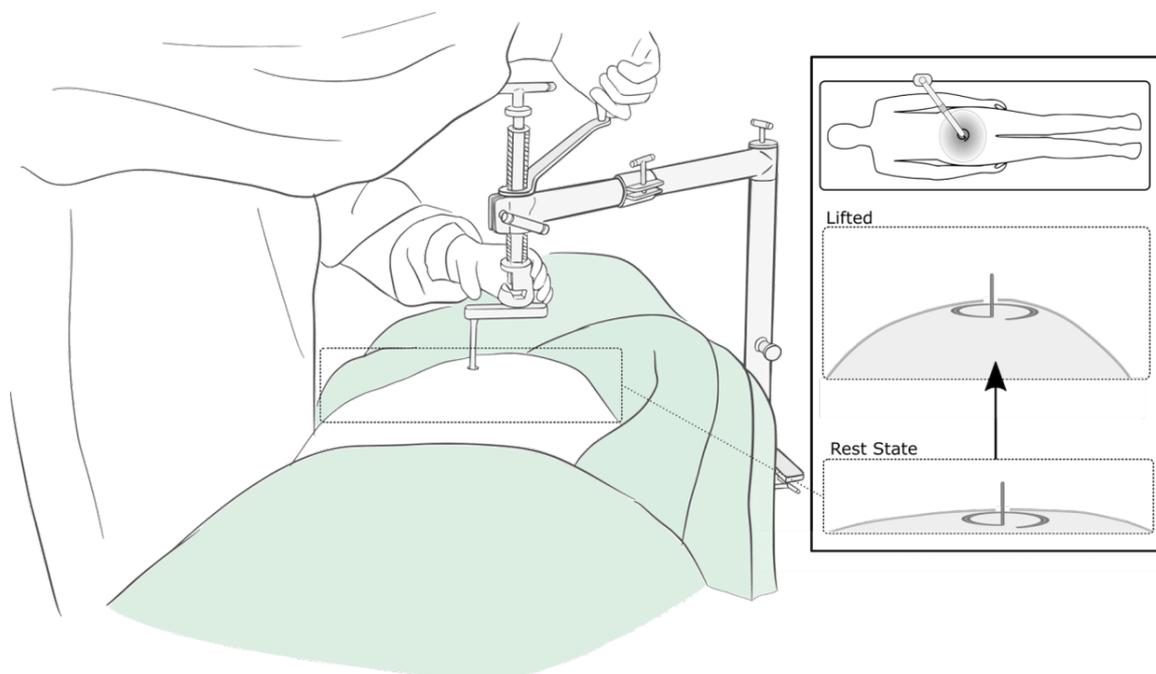
Figure 1.5: Illustration of gas-insufflation less laparoscopic surgery (GILLS) using the RAIS system.[6]

1.6. Abdominal Wall-Lifting Devices

During GILLs, the required working space in the abdominopelvic cavity is created by an abdominal wall-lifting (AWL) device. Research into AWL devices started around 1991 [44]. Since then, many iterations of the AWL device have been published and tested. This section gives an overview of the development of AWL devices. The devices are organized by four main working principles: devices using wires, devices using mechanical (moving) components, devices using a loop-shaped rod, and other experimental devices. The main benefits and drawbacks of every design will be shortly discussed to highlight new design opportunities.

Wire-based AWL devices

The first prototypes of AWL devices originated in Japan, where research on them was published in 1993. These early prototype AWL devices used wires to lift the abdominal wall and create a working space inside the abdomen. Wires were connected through incisions in the abdomen. Two examples are shown in Figure 1.6. The drawbacks of such systems are that the wires interfere with the surgeon's working space and that they can be difficult to set up.

(a) Araki et al. (1993) [45]

(b) Hashimoto et al. (1993) [46]
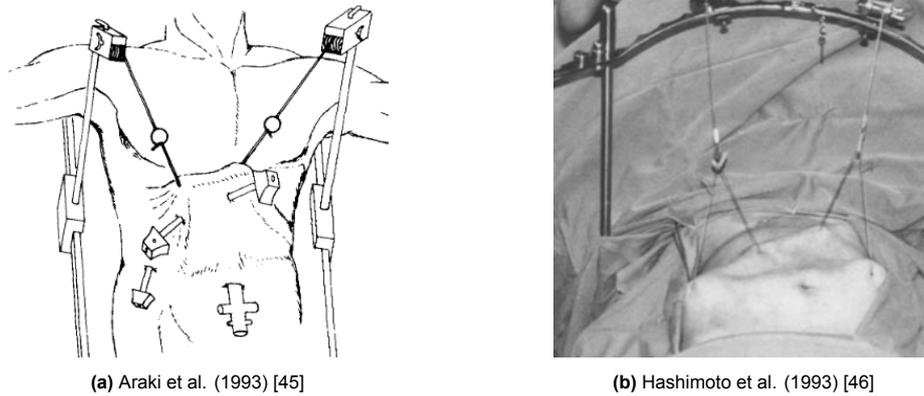
Figure 1.6: The first two AWL devices in literature use wires to lift the abdominal wall.

Two more AWL devices using wires appeared almost 20 years later. An AWL device that utilises a single wire to lift a port inserted at the umbilicus was published in 2014 [47]. It was specifically designed for gasless single-incision laparoscopy. Another AWL device, consisting of a row of wires, was published by Brun et al. for gasless laparoscopic diaphragmatic hernia repair [48]. Both devices are shown in Figure 1.7.

(a) Ikeda et al. (2014) [47]

(b) Brun et al. (2022) [48]
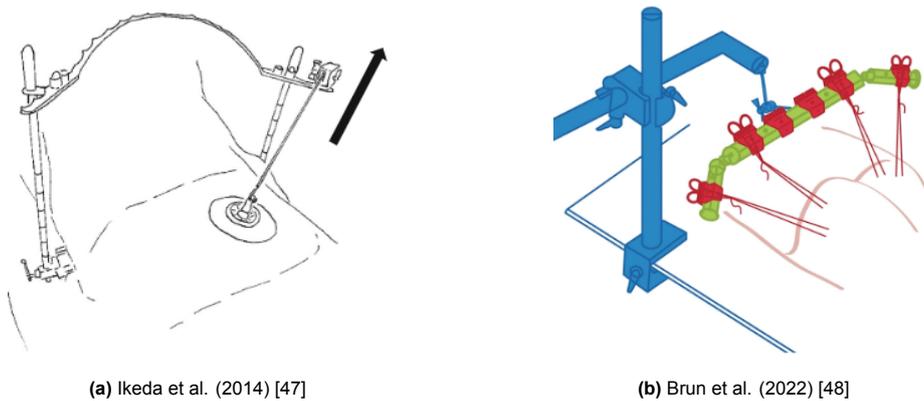
Figure 1.7: Two more AWL devices that use wires to lift the abdominal wall.

However, all wire-based AWL devices face the problem of tenting; The abdominal wall is only lifted very close to the lift device, in the shape of a tent, which limits the surgeon's visibility and leads to high tissue tension. The following three working principles all focus on reducing tenting.

Mechanical AWL devices

Soon after the first prototypes of AWL devices appeared in 1993, other working principles were tried to lift the abdominal wall. A very popular area of research was the use of mechanically expanding mechanisms. The first three attempts are shown in Figure 1.8. They all work the same: The AWL device consists of two or three legs that are inserted as one and can expand sideways once inside the abdomen. This hooks the abdomen from the inside, allowing it to be lifted by a wire or rod from above.

(a) Angelini et al. (1997) [49] **(b)** Tintara et al. (1998) [50] **(c)** Akira et al. (2005) [51]
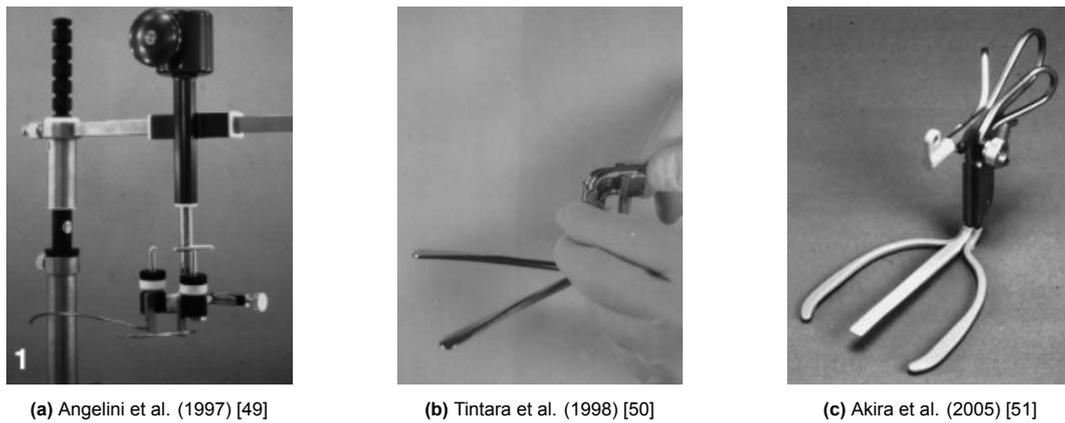
Figure 1.8: Three early attempts at mechanical AWL devices.

A new wave of research on mechanically expanding AWL devices appeared in 2013, shown in Figure 1.9. These three devices also share their working principle: multiple legs are stored in the longitudinal direction of the device and expand once inside the abdomen. These devices are more sophisticated because they use up to 8 legs and can be inserted into the abdomen straight from above. However, they are relatively expensive and uncomfortable to use, according to expert GILLS surgeon J. Gnanaraj.

(a) Wu et al. (2013) [52] **(b)** Ostdiek et al. (2013) [53] **(c)** Wu et al. (2014) [54]

Figure 1.9: Three prototypes of mechanical AWL devices that expand inside the abdomen.

Loop-shaped AWL devices

Loop-shaped AWL devices represent the current state of the art of AWL devices. The circular lifting devices require only a single incision, lift without much tenting, have no moving parts, and can be easily connected to a single retractor arm that minimizes interference with other equipment.

The first prototypes of loop-shaped AWL devices appeared in 1996, and the working principle of all devices that were to follow remained the same. They are shown in Figure 1.10. The loop can be rotated into the abdomen through a single incision to grab a circular piece of the abdominal wall, which can then be lifted. This significantly increases the functional operative field compared to other AWL devices [55].
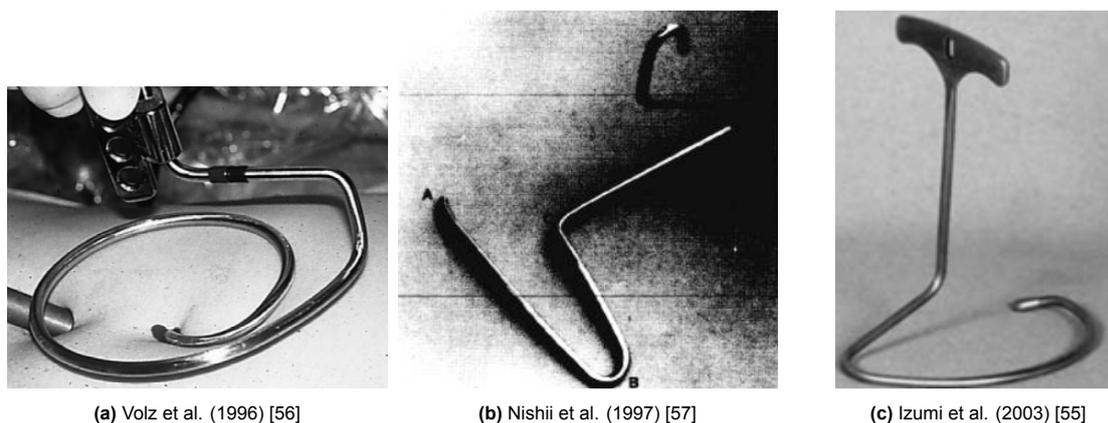
(a) Volz et al. (1996) [56] **(b)** Nishii et al. (1997) [57] **(c)** Izumi et al. (2003) [55]

Figure 1.10: Three early prototypes of AWL devices that use loop-shaped rods to lift the abdomen.

Several years later Kruschinski et al. revolutionized the field op GILLS with the Abdo-Lift, shown on the left in Figure 1.11 [58]. The focus of this design was usability in low-resource settings. The device comes as a complete package: a loop-shaped lift device, an easily adjustable retractor arm, and a modular table connector. This complete, easy-to-use AWL device marked a big step forward for GILLS.

Very recently, two similar, loop-shaped AWL devices appeared: the Keyloop [39] and the RAIS [38]. These two designs focus on usability in low-resource settings as well, and both have successfully been tested in clinical practice in multiple LMICs. According to expert GILLS surgeon J. Gnanaraj, a similar device to the the three designs in Figure 1.11 is the most used AWL device in India: the STAAN abdominal wall lift device.
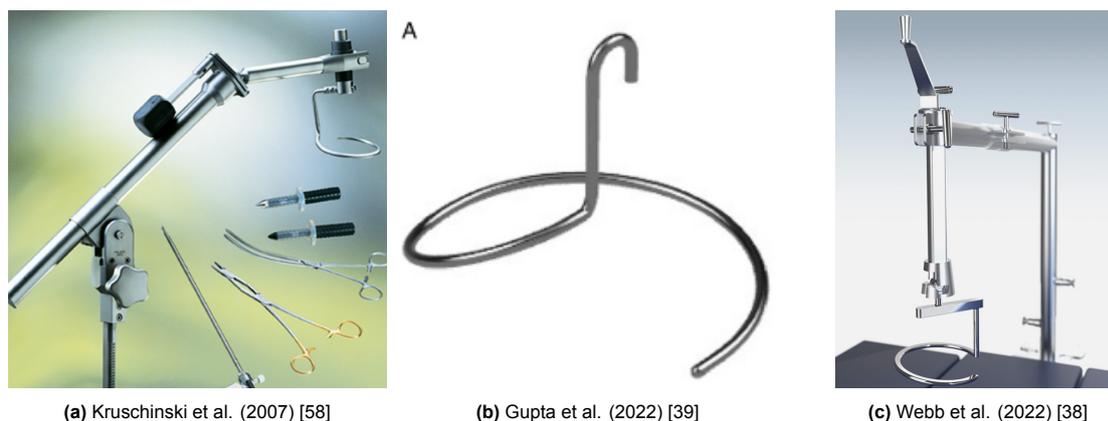
(a) Kruschinski et al. (2007) [58] **(b)** Gupta et al. (2022) [39] **(c)** Webb et al. (2022) [38]

Figure 1.11: The three loop-shaped AWL devices that represent the current state of the art.

Other experimental AWL devices

Apart from these three main working principles, some more uncommon designs have been explored in the past. Soon after the invention of the first AWL device in 1993, two separate papers were published on AWL devices that used inflatable balloons [59, 60]. The balloon was inflated after insertion into the abdomen, hooking the abdominal wall from inside and allowing it to be lifted. However, these devices did suffer from tenting.

In the same year, Nakamura et al. revealed an AWL device that lifted the abdomen from the side, instead of from the top as usual [61]. It is shown on the right on Figure 1.12 Two metal fishing rods would be inserted into the abdomen from the side and tilted upwards. The bow of the rods provided a dome-shaped working space, with no interference from above. Notwithstanding these advantages, the device was difficult to set up and required multiple additional incisions to insert every rod.

(a) Viani et al. (1995) [59]   (b) Chang et al. (1996) [60]   (c) Nakamura et al. (1996) [61]
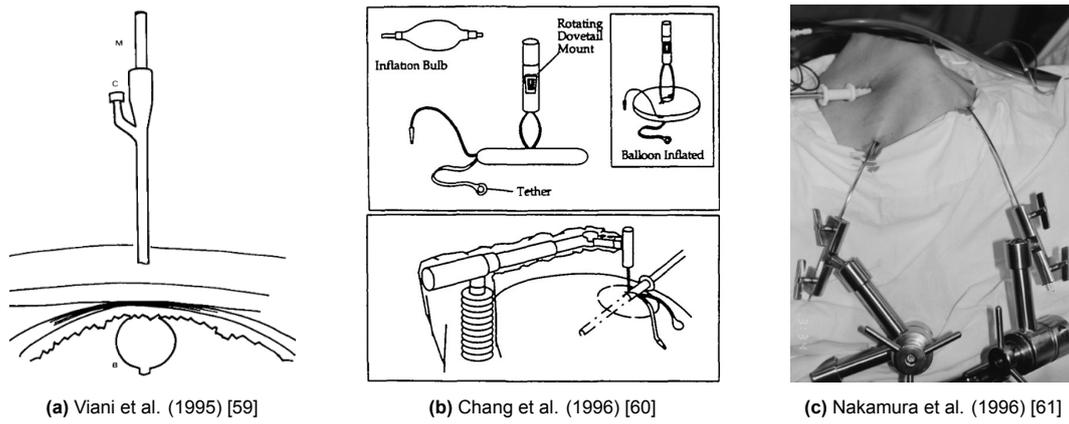
Figure 1.12: Three experimental AWL devices from the beginning of AWL device research.

Another idea that was teased in two papers was to lift the abdomen from the outside, without having to create an incision for the AWL device. Both Udwadia et al. and Naito et al. published such a device based on suction [62, 63], shown in Figure 1.13. The abdominal wall could be attached to the AWL device by suction, through a rigid shell or an array of cups, and then lifted. Neither of these two devices has been tested on human patients.

Finally, Schaller et al. revealed an AWL device in 2009 that works like a press [64]. Two rods are inserted into the abdomen, then connected by a patch of plastic inside, which presses on the internal organs to lift the abdominal wall. It is shown in the middle of Figure 1.13.

(a) Udwadia et al. (2005) [62]   (b) Schaller et al. (2009) [64]   (c) Naito et al. (2018) [63]
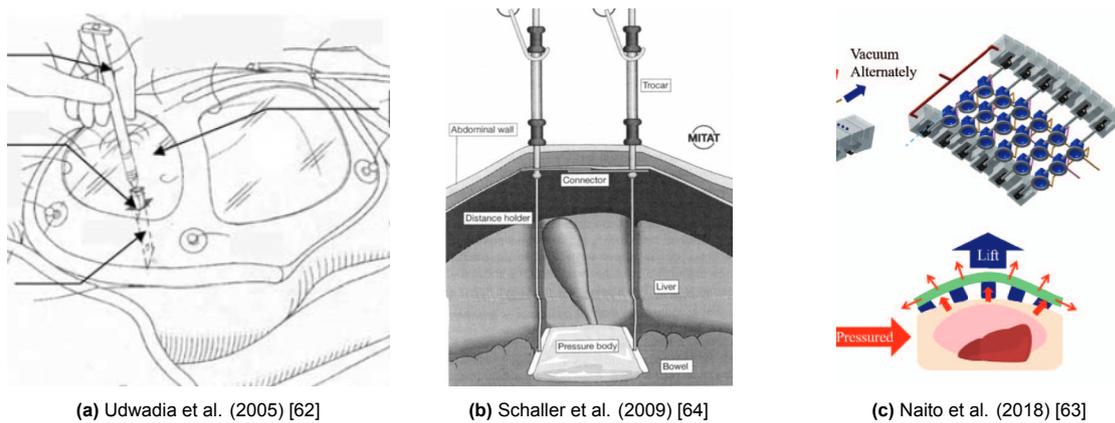
Figure 1.13: Three more experimental AWL devices. None of these have been tested on human patients.

It is important to note that neither of the current lifting devices is without problems, as will be discussed in the problem analysis in the next chapter. Limitations with respect to visibility and working space remain prominent, and hence this thesis will explore a new context-driven design of the AWL device for BTL procedures in India.

<div style="text-align: right">

2

</div>

<div style="text-align: right">

Project definition

</div>

2.1. Problem Analysis

The current state of the art of AWL devices is a circular lifting device connected to a single mechanical retractor arm. Examples are the RAIS system, the KeyLoop, and the Abdo-lift, as shown in Figure 1.11 [38, 39, 58]. In Indian clinical practice, the similar-looking STAAN device is most commonly used [65]. These devices are the result of 30 years of development and solve many of the problems associated with early prototypes of AWL devices. Tenting has been significantly reduced, the lift devices require only a single incision, and the single mechanical retractor minimizes interference with other equipment.

Despite these advancements, difficulties remain during GILLS procedures related to the use of the AWL device, which increases the average time per procedure. The problems were identified by a careful review of the scientific literature on GILLS and by speaking with an expert in the field of GILLS, J. Gnanaraj, who performed hundreds of GILLS procedures in low-resource settings himself and published several articles on the topic.

The main issue that affects surgeons during GILLS BTL procedures in low-resource settings is the lack of visibility inside the abdominopelvic cavity. As explained in Section 1.2, during conventional laparoscopy surgeons view the inside of the abdomen using a laparoscope. Imaging from state-of-the-art laparoscopes in HICs is so good that visibility is similar to open surgery. GILLS procedures require laparoscopes for imaging too, but three factors cause a reduction in overall visibility when performing these in low-resource settings.

1. The first factor is one of the key limitations associated with GILLS, namely the restricted working space inside the abdominopelvic cavity. By using an AWL device, the working space created in the abdomen is usually less compared to gas insufflation [66]. This can limit the surgeon's range of motion and manoeuvrability, which in turn limits the positioning of the laparoscope.
2. The positioning of the laparoscope is further affected by the second factor, untrained personnel. In low-resource settings, it is very common that the laparoscope is handled by a nurse or operating assistant while a single surgeon performs the procedure. Significant time is lost in every procedure because the surgeon has difficulty instructing untrained personnel how to hold, orient, or move the laparoscope.
3. The third factor is that surgeons in low-resource settings typically must use laparoscopes of lesser quality compared to HICs due to the limited availability of state-of-the-art laparoscopes [67]. State-of-the-art laparoscopes offer better visualisation than the laparoscopes used in low-resource settings, often older or context-specific models with a $0°$ viewing angle, due to a wider field of view, higher image quality, and the ability to rotate around the lateral axis to look around the tip of the laparoscope.

   Furthermore, the laparoscopes used in low-resource settings struggle to sufficiently light the area of surgery without overheating. As a result, some context-specific laparoscopes, as shown in Figure 1.4, only reach 20% of the illumination values of state-of-the-art laparoscopes [32].

Other issues with the current AWL devices relate to their outer dimensions.

4. The loop shape is not a one-size-fits-all solution. For some devices, depending on the length and weight of the patient, a differently sized loop has to be used for the procedure, with four different sizes to choose from [39].
5. The AWL device is inserted by blind entry. That means that the surgeon does not see the device as it is being inserted. Any sharp edges in the design can potentially cause internal injury.

.

2.2. Project Goal

After exploring GILLS BTL procedures in rural hospitals in India using the current state-of-the-art AWL devices, a novel area of development was identified; Increasing the surgeon visibility while eliminating the use of the laparoscope. The goal for this graduation project is:

Design, build, and test a context-driven AWL device with an integrated imaging system for gas insufflation-less laparoscopic bilateral tubal ligation in low-resource settings, that substitutes for both the current lifting device and the laparoscope, and is cost-effective, robust, user-friendly, and compatible with current mechanical retractors.

2.3. Project Scope

The scope of the project is to enhance surgeon visibility by designing a new context-driven AWL device with an integrated imaging system. This system should create the working space and replace the laparoscope during laparoscopic BTL procedures, eliminating problems related to laparoscope quality and positioning.

It is important to note that the focus of the project is only on one specific part of the complete AWL device, the lifting device, and not on the mechanical retractor. A typical AWL device consists of a lifting device and a mechanical retractor. Figure 2.1 shows a render of the RAIS system, where the two parts are coloured; The lifting device is shown in green and the mechanical retractor in red.

The lifting device that will be designed in this project should be compatible with commercially available mechanical retractors, such as the arm of the RAIS system as shown in Figure 1.5 and Figure 2.1.

The lifting device will specifically be designed for the context of GILLS BTL procedures in rural hospitals in India, which differs from typical HIC settings in terms of financial resources and access to maintenance, spare parts and consumables. For such context-driven design, it is important to involve the user through collaborative prototyping to ensure that the designed solution will fit the context of use. [1]
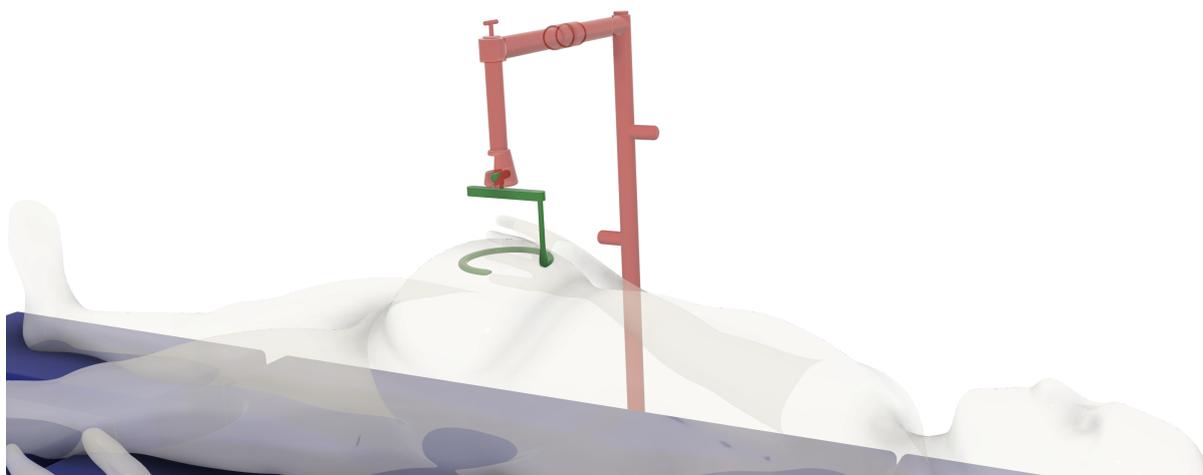
Figure 2.1: Render of a complete AWL device, the RAIS system. The focus of this project is on the lifting device (green), and not on the mechanical retractor arm (red).

2.4. Project Outline

This report consists of five distinctive design phases. The first phase is the identification of the design goals, presented in this chapter and Chapter 3. Secondly, Chapter 4 and Chapter 5 present the process of concept generation and selection. Based on the chosen concept, the final design is presented in Chapter 6 and all the subsystems are explained in the subsequent Chapters 7 - 10. Chapter 11 describes the two prototypes that were built during this project. The fourth phase is verification and validation, presented in Chapters 12 - 14. The final phase is the discussion and conclusion in Chapter 15 and Chapter 16 respectively.

3

Design specifications

3.1. Design drivers

The design drivers are the parameters that the design of the lifting device aims to optimize. Based on scientific literature and interviews with experts, four main design drivers were identified that govern the development of a lifting device that meets the specific needs of rural hospitals in India. These design drivers and their rationale are listed below. The exact specifications will be listed in Section 3.2.

- **Surgeon visibility:** This is the main design driver for this project. Visibility is crucial for the surgeon to perform accurate and precise BTL procedures but is often lacking in low-resource settings, for several reasons as outlined in Section 2.1. Designing a lifting device that enhances visibility will allow surgeons to make better-informed decisions, reduce the risk of errors, and improve overall surgical outcomes.
- **Cost-effectiveness:** The lifting device should be cost-effective, an essential requirement for any medical device designed for low-resource settings. Keeping the device's upfront cost, running costs, and maintenance costs low makes it accessible to healthcare facilities in low-resource settings. It enables wider adoption and implementation, increasing the potential impact of the device in low-resource settings.
- **Robustness:** This design driver refers to the device's ability to withstand the challenges and demands of laparoscopic surgery in resource-constrained environments. A robust design ensures that the design is sturdy, durable, reliable, dust- and waterproof, and can cope with power grid outages.
- **User-friendliness:** The usability of the lifting device is crucial for its successful implementation. The user interface should be designed to accommodate the often undertrained staff in hospitals in low-resource settings. Additionally, compatibility with existing mechanical retractors is required to ensure seamless integration.

3.2. Requirements

The problem analysis, design goal, and design drivers led to a set of functional requirements and performance criteria, listed in this section and summarised in Table 3.1. The list is deliberately limited to 13 requirements to confine the scope of the project. These requirements are the most critical aspects that the lifting device should adhere to. Each requirement has a corresponding performance criterion that quantifies the requirement.

- **Abdominal wall lifting:** The primary purpose of this device is to lift the abdominal wall. The maximum load on the lifting device reported across multiple studies is 13.6 [kg] [39]. This is consistent with research into the maximum acceptable force on the abdominal wall, which is 130 [N]. Trauma occurs from 150 - 170 [N] [68]. The lifting device should be able to sustain the maximum load, i.e. it should be able to lift 140 [N] without permanent deformation.

- **Visibility:** The main design driver from Section 3.1 is surgeon visibility. It consists of two parts: Operational volume and image quality. The operational volume should be at least equal to the volume created during traditional laparoscopy.

  Secondly, the quality of imaging should be comparable to a state-of-the-art laparoscope from 10 years ago, based on input from expert GILLS surgeon J. Gnanaraj. This will be objectively measured using four image quality factors: (perceived) sharpness, noise, colour, and distortion [69]. The field of view and light intensity should also be comparable.

- **Product surface temperature:** To avoid tissue damage due to heat burns, the device has a maximum surface temperature of $41°$ [C]. This limit is based on IEC 60601-2-37, the guidelines from the International Electrotechnical Commission (IEC) for medical electrical equipment part 2-37: Particular requirements for the basic safety and essential performance of ultrasonic medical diagnostic and monitoring equipment.

- **Low upfront purchase price:** A direct result of the second design driver, the device should be a low-cost purchase. Currently, a complete AWL device such as the RAIS system costs approximately $1200[1]. Furthermore, context-specific laparoscopes cost at least $300 [34]. Hence the maximum purchase price for this lifting device is set to €250, to ensure a competitive market position.

- **Use of supplies:** As mentioned in Chapter 1, healthcare facilities in low-resource settings struggle to source single-use items and supplies. Therefore, the lifting device may use no other resources or supplies than the basics: water and electricity. The water should not need to be sterile, and neither should the device require continuous electricity from the power grid.

- **Dust- & waterproof:** The device is in constant contact with human bodily material (HBM) and must therefore be completely dustproof and waterproof. This ensures no HBM enters the device, which is essential for maintaining its functionality, preventing damage, and promoting patient safety. The required level is IP67, for which it is required that the device is submerged in water for 30 minutes with its highest point at least 150 [mm] below the surface.[2]

- **Cleaning & sterilisation:** In between every GILLS procedure, reusable equipment has to be cleaned. This significantly reduces the risk of infection and cross-contamination. Hospitals in low-resource settings typically use immersion in chemicals, which the lifting device should be able to withstand. Autoclave sterilisation is deliberately not included because the intended users are low-resource hospitals typically without autoclaves [70], which in turn allows for a simpler and therefore cheaper device.

- **Weight:** The device may not be too heavy, as that might make it inconvenient to work with. The maximum weight is set at 1 [kg] based on input from expert GILLS surgeon J. Gnanaraj.

- **Insertion diameter:** All current lifting devices have to be inserted into the abdominopelvic cavity in some way. If the new design requires insertion as well, the diameter of insertion may be no more than 12 [mm]. This corresponds to the diameter currently needed to insert a lifting device and laparoscope at the umbilicus [39].

- **Compatibility with extractors:** As mentioned in Chapter 2, the lifting device should be compatible with currently existing retractors. The focus will be on the state-of-the-art retractor arm from the RAIS system, as it is similar to the arm used for the STAAN device.

- **Data & power connection:** The power connection, and data connection if required, should be widely compatible with infrastructure in low-resource settings. For that reason, the power and data should be transferable using a USB-A connection. Since this connection port is universal, any surgeon can operate the lifting device using a laptop.

- **Adaptability to patients:** Patients come in many different lengths and weights. To accommodate the majority of the Indian female population with one device, it should be designed for the average Indian female patient with a height of 1.52 [m] and corresponding weight between 46-58 [kg]. [71]

- **Intuitiveness:** The device should have a clear and intuitive interface to accommodate the often untrained personnel in low-resource settings. This is to be achieved by testing prototypes in close interaction with local end users. Furthermore, the lifting device with an integrated imaging system

---

[1]https://theconversation.com/five-billion-people-cant-afford-surgery-a-team-of-innovators-could-soon-change-this-185081
[2]https://clarionuk.com/resources/ip-ratings/

will be user-tested on this aspect by having expert GILLS surgeon J. Gnanaraj compare it to the current setup (lifting device and laparoscope) during a simulated GILLS BTL procedure.

Secondly, the production of the device should fit the local production capabilities and have a clear step-by-step workflow such that it can be repeated.

The requirements are grouped per category in Table 3.1, which are recognisable by the identifier in the first column. Identifier **P** are the three requirements relating to performance, which represent the three core functions of the device: lifting the abdomen and viewing inside of it, while not overheating. Identifier **C** relates to costs, **R** to robustness, **D** to dimensions, **M** to modularity, and **E** to ergonomics. The categories are ranked by importance from high to low. The second column is the requirement, and the third column specifies the corresponding performance criteria.

Table 3.1: Requirements and corresponding performance criteria for the design of the lifting device.

ID	Requirement	Performance criteria
P1	Abdominal wall lifting	Must be able to sustain 140 [N] distributed lifting force
P2	Visibility	Must provide better visibility compared to current setup
P3	Product temperature	Surface-temperature may not exceed $41°$ [C]
C1	Low upfront purchase price	Must cost less than €250
C2	Use of supplies	May use only the basic supplies (water & electricity)
R1	Dust- & waterproof	Must be dust- & waterproof at IP level 67
R2	Cleaning & sterilisation	Must withstand chemical sterilisation
D1	Weight	May weigh no more than 1 [kg]
D2	Insertion diameter	Must fit through a 12 [mm] diameter circular incision
M1	Compatibility with extractors	Must be compatible with RAIS lift arm
M2	Data-/power-connection	Must use USB-A port for power and data transmission
M3	Adaptability to patients	Must adapt to patients around 1.52 [m] and 46-58 [kg]
E1	Intuitiveness	Must have a clear and intuitive interface & production workflow

4

Concept generation

4.1. Morphological analysis

Innovative and accessible solutions are imperative to address the challenges faced by surgeons performing GILLS BTL procedures in rural hospitals in India. This chapter proposes four concept solutions to meet the requirements from Chapter 3. These four concepts were generated through morphological analysis, which will be described in this section.

Morphological analysis is a product design method that breaks down a product into parameters and then systematically recombines them in different ways to generate concepts [72]. The parameters for the AWL device are based on its three core functions, which are represented by the requirements relating to performance in Section 3.2. It was decided to exclude thermal control from the morphological analysis because it is highly dependent on the final configuration of the lifting device. Three parameters for the morphological analysis were identified based on the remaining two core functions.

1. Attachment: First and foremost, the new lifting device should attach the mechanical retractor to the abdominal wall such that it can be lifted and create a working space for the surgeons.
2. Viewing: The second core function is that the lifting device should provide surgeons with a view inside the abdomen during the procedure, effectively replacing the laparoscope.
3. Lighting: This parameter also follows from the second core function. Since no natural light source is present inside the abdomen, an artificial source of light needs to be provided.

Five conceptual solutions were generated for each of these three parameters. The solutions are based on technologies from previous research, commercially available medical devices, or non-medical applications.

Putting these solutions for the different parameters in a morphological table allows for studying the interdependency of the solutions. The complete morphological table with 14 conceptual solutions is shown in 4.1. In Section 4.2, these conceptual solutions are combined into four cumulative concepts.

4.2. Four concepts

Four concepts were created based on the morphological Table 4.1. Every concept combines different options for the three parameters. The concepts will be worked out in more detail in this section, and the concept with the most potential will be selected in the next Chapter 5.

Table 4.1: Morphological table.

Function:	Attachment	Viewing	Lighting
Option 1	Circular hook	Opening	Optical fibres
Option 2	Expanding hook [52]	Lens system	LED strip
Option 3	Balloon device	Central camera	Lens system [73]
Option 4	External suction	Steerable camera	Fluorescent material
Option 5	Rod-based system	Distributed cameras	
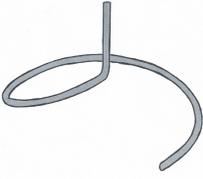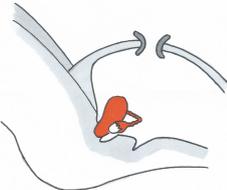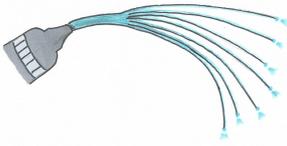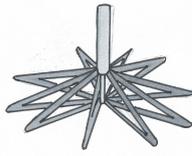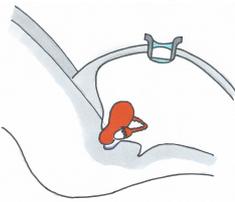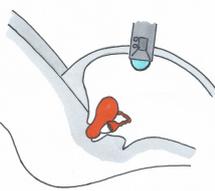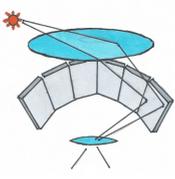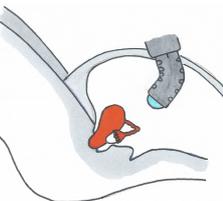
Concept 1: Circular hook with a central camera and LED light strip

The first concept combines attachment option 1 (circular hook), viewing option 3 (central camera), and lighting option 2 (LED strip). The lifting device is a circular hook with a wide-view camera placed at the bottom end of the vertical shaft. The circular hook is equipped with LED lights, providing a ring of light around the camera, much like commercially available ring lights do[1]. This gives more diffused, evenly distributed light on the subject which reduces glare and the appearance of harsh shadows.

The rationale for this concept is to complement the current state-of-the-art AWL device with cheap off-the-shelf electronics. The camera and LED strip can be connected to any laptop via USB and no additional supplies would be needed.

---

[1]https://thriveproductstudio.com/ring-lights-product-photography/
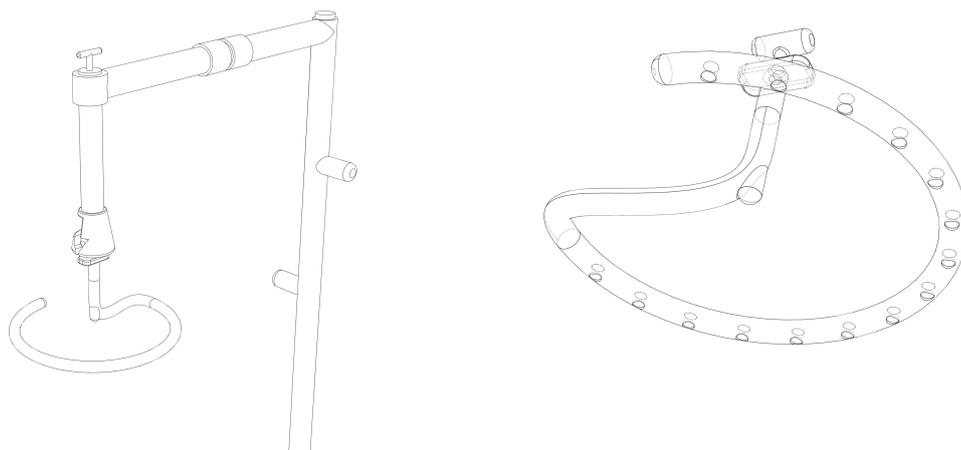
Figure 4.1: Concept 1: Circular hook with a central camera and LED light strip.

Concept 2: Expanding hooks with a steerable camera and optical fibre lighting

The second concept combines attachment option 2 (expanding hook), viewing option 4 (steerable camera), and lighting option 1 (optical fibres). For the expansion mechanism, a system was chosen with two legs that can be rotated to open sideways. The device is inserted with closed legs that open once inside to create a working space. The steerable camera is connected to the lifting device and sits right behind the two legs. It has three degrees of freedom: rotation, tilt (upward/downward) and longitudinal motion (forward/backward). The light is transported through optical fibres to two light bars, one in each leg, lighting the working space from above.

The rationale for this concept is to use moving parts to compensate for the lack of operational volume. Mechatronics control the laparoscopic camera. The frame with the expanding legs would be custom-built. The camera could be connected to any laptop using USB, and the lighting requires a laparoscopic light source. No additional supplies would be needed.
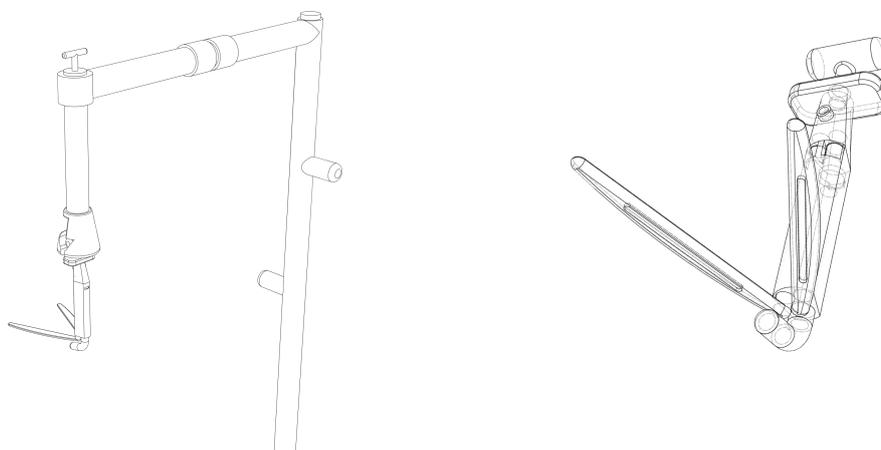
Figure 4.2: Concept 2: Expanding hooks with a steerable camera and optical fibre lighting.

Concept 3: Balloon with distributed cameras and reflectors

The third concept combines attachment option 3 (balloon device), viewing option 5 (distributed cameras), and lighting option 4 (fluorescent material). The lifting device is inserted as a deflated balloon, and once inside it is inflated to the shape shown in Figure 4.3. The gaps in the balloon allow for instruments to pass through. The convex side of the balloon supports the abdominal wall. The concave side is made of reflective material and holds several small cameras. These cameras can provide imaging from multiple angles or combine into a 360-degree view.

The rationale of this concept was to combine unconventional techniques. The system with multiple cameras would require specialised hardware and software because the imaging from multiple cameras

would have to be processed by the device before sending it to a monitor. Furthermore, pressurized air is needed to inflate the balloon.
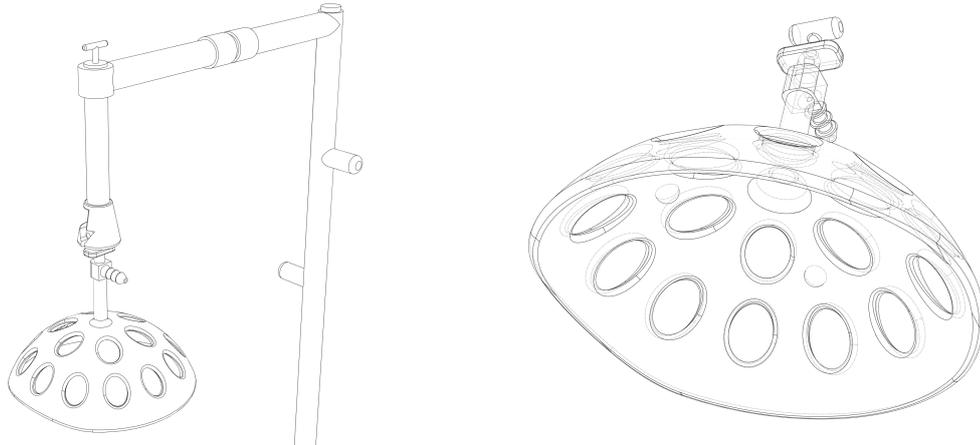
Figure 4.3: Concept 3: Balloon with distributed cameras and reflectors.

Concept 4: Suction cups with a large central opening

The fourth concept combines attachment option 4 (external suction), viewing option 1 (opening), and lighting option 5 (none). The abdominal wall is attached to the lifting device by three suction cups, surrounding a 30 [mm] port. That port size is similar to single incision laparoscopy [74]. It is important to note that this concept would likely still require the use of a traditional laparoscope.

The rationale for this concept was to make the lifting device as minimally invasive as possible. The device would need to power its suction cups through an external or internal pressure pump. However, no other electronics and no supplies would be required.
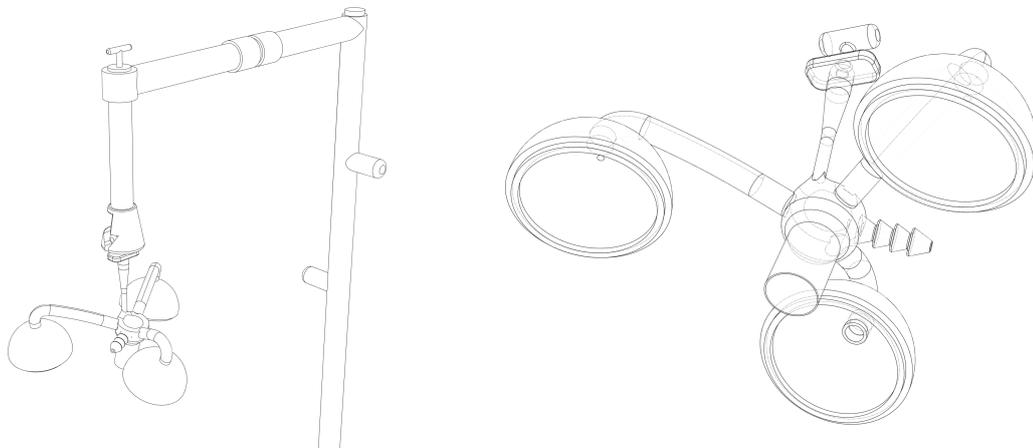
Figure 4.4: Concept 4: Suction cups with a large central opening.

<div style="text-align: right; font-size: 4em;">5</div>

Concept selection

5.1. Criteria

The next step in the designing process is to systematically evaluate the four concepts proposed in Chapter 4. A Harris profile is used to provide a clear comparison between the different concepts [75]. After assigning scores, an informed decision can be made about the potential of every concept.

The concepts are scored on eight criteria. These criteria are based on the requirement categories from Section 3.2. The criteria differ from the requirements such that the concepts, without any technical specifications, can be compared to each other. A score indicates how much potential a concept has to meet certain criteria. The eight criteria are ranked in order of importance below:

1. Lifting capability: The concept should have the potential to sustain a lifting force of 200 [N].
2. Visibility: The concept's imaging system should be able to replace the laparoscope.
3. Purchase price: The concept's cost should be less than €250, and cheaper is better.
4. Use of supplies: The concept may consume only basic supplies in small quantities.
5. Robustness: The concept should have minimal points of failure.
6. Dimensions: The concept should be small and lightweight.
7. Modularity: The concept should work with any power supply and monitor.
8. Ergonomics: The concept should be intuitive to work with.

5.2. Evaluation

The four concepts are scored on the eight criteria from Section 5.1 in a Harris profile. The Harris profile does not give scores in terms of numbers but in quantitative terms with (- -) being bad, (-) moderate, (+) good and (+ +) excellent. The list below explains the score of every concept on each of the eight criteria. The resulting Harris profile is shown in Figure 5.1.

1. Lifting capability was evaluated as good (+) when the concept was expected to be able to lift 200 [N], and as bad (--) if it is likely unable to do so. Concepts 1 and 2 received a good (+) score for this criterion because they are proven working principles. Concept 3 received excellent (++) as well since it has a strong structural shape. Concept 4 received a moderate (-) score, because higher lifting forces may require unfeasibly high suction forces.
2. Visibility was evaluated as good (+) when the concept was expected to replace the laparoscope, or bad (--) if it was not. Concepts 2 and 3 received an excellent (++) score because the steerable camera and distributed cameras might outperform currently used laparoscopes in i.e. depth perception [76]. Concept 1 received a good (+) score. Concept 4 was scored as bad (--) because it still requires the use of a traditional laparoscope.
3. Purchase price was evaluated as good (+) when the concept can likely be manufactured for less than €250. This only holds for concept 1, which uses off-the-shelf electronics and a custom frame. The steerable camera from concept 2 and the multiple suction cups from concept 4 are expected

to be more expensive, but still reasonably priced, hence the moderate (-) score. Even more expensive is concept 3, consequently scored as bad (--), because it requires special materials, a custom mould, and multiple cameras.

4. Use of supplies was evaluated by the amount of electricity required. Only a small amount, for the camera and lighting system, was evaluated as good (+), which is the case for concepts 1 and 2. Concepts 3 and 4 require additional power for the inflation and suction systems respectively, and were therefore awarded a moderate (-) score.

5. Robustness was evaluated by assessing potential points of failure. Concept 3 was rated a bad (--) score because it has multiple cameras and an inflation system. Furthermore, leakage of the balloon would directly necessitate a conversion to open surgery. Concept 2 was rated moderate (-) because it has multiple moving parts (a steerable, a multiple DOF camera and expanding legs) but no points of leakage. Concept 1 was rated as good (+) because it does not have moving parts, and extraction of the lifting device in case of emergency is easy. Concept 4 was rated excellent (++) because it has no parts inside the abdomen, and a failure of one suction cup still leaves two other cups to lift the abdominal wall.

6. Dimensions were evaluated by estimating the weight and size of the concepts. Concept 4 was rated as bad (--) because it has multiple large suction cups, and the suction pump adds to the weight. Concept 1 was rated moderate (-) because the metal frame makes it heavier than other concepts. Concept 2 was rated good (+) because it has a compact frame with an expansion mechanism that allows efficient storage. Concept 3 was rated excellent (++) because the deflated balloon would take up little space and be relatively lightweight.

7. Modularity was evaluated as excellent (++) if a concept works using any laptop as a monitor, and bad (--) if it requires custom control options, imaging software, or power supply. Concept 1 requires a single USB connection to power its LED lights and feed imaging and was therefore rated as excellent (++). Concept 4 was rated good (+) because it only requires a custom power supply. Concept 2 was rated moderate (-) because it requires a laparoscopic light source and control software for the moving tip. Concept 3 was rated bad (--) because it requires a custom power supply and imaging software to process multiple imaging feeds.

8. Ergonomics was evaluated by assessing the difficulty of each concept's functioning. Concept 4 was rated as excellent (++) because no camera system is present and suction cups could be placed with a certain amount of freedom. Concept 1 is rated good (+) because it is a plug-and-play device that works with any laptop, and requires only a few buttons for the lighting on the device. Concept 3 was rated moderate (-) because it would require hospital staff to be proficient with its custom imaging software. Concept 2 was rated bad (--) because it would require even more extensive training on the control of the multiple DOF camera.

	Concept 1				Concept 2				Concept 3				Concept 4			
	--	-	+	++	--	-	+	++	--	-	+	++	--	-	+	++
Lifting capability			■				■				■			■		
Visibility			■				■				■			■		
Purchase price			■			■			■					■		
Use of supplies			■				■			■				■		
Robustness			■			■			■							■
Dimensions		■					■					■	■			
Modularity				■		■			■						■	
Ergonomics			■		■					■						■
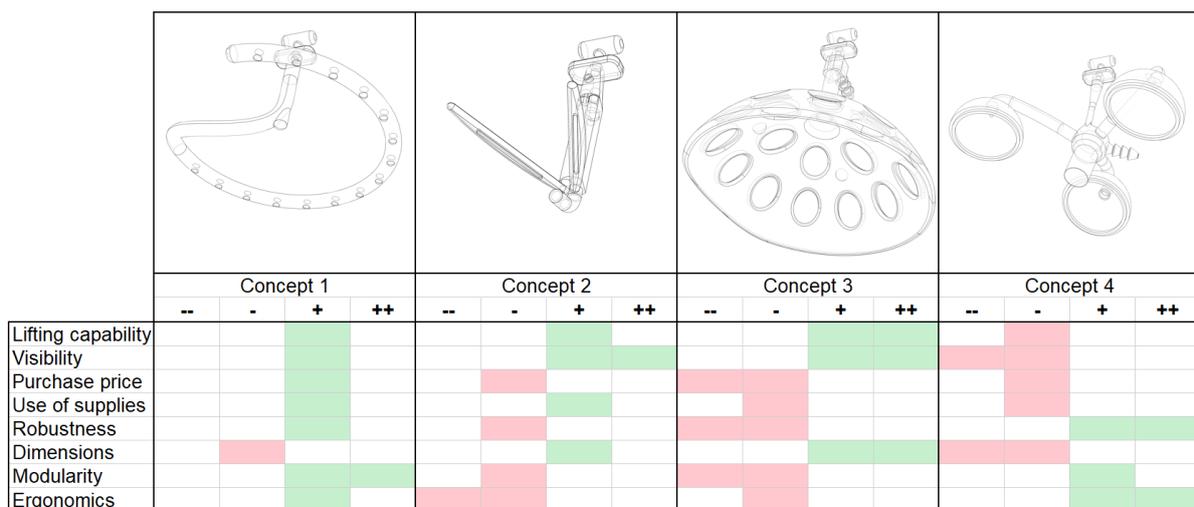
Figure 5.1: Harris profile of the four concepts.

5.3. Selection

The complete Harris profile in Figure 5.1 shows that the lifting device based on a circular hook with a central camera and LED light strip is the most promising concept. This concept scores good or excellent on seven of the eight criteria and wins by performing well in every aspect. Therefore, the upcoming chapters concerning the final design will be focused on this concept. The final design based on this concept is presented in Chapter 6.

The other concepts fall short for several reasons. Concept 2, the expanding hooks with a steerable camera and optical fibre lighting, scores excellent on the two most important criteria. However, it also scores moderate or bad on four other criteria. The expansion mechanism had potential, but the steerable camera would be too hard to implement in low-resource settings that are typically short on skilled staff. Concepts 3 and 4 are even more inconsistent, with multiple excellent scores and multiple bad scores. The increased technical complexity of these concepts' inflation/suction systems does not match the low-resource setting of this thesis.

One caveat with the concept generation and selection processes (morphological analysis and Harris profile) is that the scores in the Harris profile are dependent on the combinations made in the morphological analysis. For example, if Concept 2 had used a central camera instead of a steerable camera, its Harris score for ergonomics would be (+) instead of (--).

Therefore, the concept selection was substantiated using feedback from two expert rural surgeons, Dr P. Odula and Dr J. Gnanaraj. Both surgeons stressed the importance of using a loop-shaped lifting device. This shape is the result of many years of development and has been successfully used in thousands of procedures. A wide-view camera (possibly 360 degrees) was the preferred option, closely followed by a moving camera. The technology used for the lighting system should mainly be cheap. This feedback confirmed the choice for Concept 1, though possibly with a moving camera.

6

Design outline

The final design of the lifting device is shown in Figure 6.1. It is a stainless steel hollow circular hook that houses a 5 MP camera module and an LED lighting system. This lifting device substitutes for both the traditional lifting device and the currently used laparoscopes. It can be connected to any laptop with a USB-A port and does not require custom software.

Figure 6.1: Render of the final design of the lifting device.

The electronic system of the lifting device is described in Chapter 7. The outer dimensions and structural design are described in Chapter 8 and Chapter 9 respectively. The production & assembly process is described in Chapter 10, with the production of two prototypes exemplified in Chapter 11. The lifting device's performance is verified in chapters 12 and 13, and validated in Chapter 14. Chapter 15 discusses the results of this study.

6.1. Electronic system

The electronic system of this lifting device consists of two main hardware components, an imaging system and an LED lighting system. The PCB of the camera module and the resistor for the LED strip are housed in the 3D-printed electronics housing. They are connected to a single USB-A connection.

The imaging system is an OmniVision 5693 CMOS camera module with a 5 MP sensor and a fixed-focus, $120°$ FOV lens system. The camera module originates from the smartphone industry and has the industry-standard 8.5x8.5 [mm] baseplate dimension, with a height of 5.8 [mm]. As of December 2023, it costs less than €20. It has a $110°$ field of view, making it ideally suited for capturing the whole surgical field from above. Verification of the imaging system shows that its quality is close to current state-of-the-art 4K laparoscopic systems. The high-quality imaging, at this price point, is one of the strengths of this lifting device.

The LED lighting system is a custom LED circuit using multiple COB chips rated at 65 [lm] per chip, connected in parallel to a communal resistor. This configuration places the heat-generating resistor

outside of the loop. However, for the aluminium prototypes, a pre-assembled LED strip was used. It is a commercially available 12 [V] 480 [LEDs/m] COB strip, 8 [mm] wide, with a $180°$ beam angle. A step-up converter converts the 5 [V] from the laptop USB-A port to 12 [V]. The strip generates too much heat (due to the individual resistor layout) and insufficient light.

6.2. Dimensions & Structure

The shape of the lifting device is calculated using methods from research. The radius of the loop of the lifting device is 70 [mm], and the loop itself has a diameter of 12 [mm]. The loop has a $\frac{3}{4}$ circumference and slopes upwards toward the upright by an angle of $20°$. This ensures easier insertion and a better angle for the camera which is positioned perpendicular to the loop. The upright provides a 65 [mm] clearance between the insertion point and the electronics housing. The connector is in line with the frame for strength and ease of positioning.

The structure of the lifting device is based on a 12x1 [mm] tubular load-bearing frame from stainless steel 17-4 PH. The ends of the tube are capped by a machined endcap and a machined RAIS connector. The electronics housing is 3D-printed from Nylon. For the prototype presented in Section 6.3, aluminium 6060-T66 was used for all metal parts and the housing and endcap were 3D-printed from PLA.

The structure has 24 holes for the LED system in the loop with a diameter of 5.5 [mm], spaced at approximately 10 [mm]. Furthermore, it has a 7.5 [mm] diameter opening for the camera and an extra one for assembly. The electronics are inserted through a slot opening in the upright, with a width of 9 [mm] and a height of 16 [mm]. The structure is designed to handle a distributed load of 140 [N] and indirect verification using the aluminium prototype confirms it has the required structural strength. The structure is sealed by polyolefin heat shrink for waterproofness, with a small cutout for the protective lens over the camera sensor.

6.3. Production & Prototyping

The production and assembly process of the lifting device was one of the main focus points of the project, exemplified by a 1:1 completely functional aluminium prototype, shown in Figure 6.2.

The tubular load-bearing is bent into shape using rotary draw bending with two custom-produced bending dies. For the prototype, a wooden compression bending die was used to bend an annealed, sand-filled aluminium tube by hand. The holes in the frame are drilled at their exact location using custom 3D-printed jigs. The machined parts are produced by a combination of turning and milling. The prototype's housing has a chrome coating. The heat shrink is applied using a heat gun. The electronics are positioned using guidewires and secured using small 3D-printed holders. The prototype is used for all verification and validation procedures.

Figure 6.2: Pictures of one of the aluminium prototypes of the lifting device.

7

Electronic system

7.1. Applicable requirements

This chapter marks the start of the detailed design process of the concept selected in Chapter 5, the circular hook with a central camera and LED strip. In four consecutive chapters, every subsystem of the lifting device will be presented. The electronic components required for this device are investigated first because their position, dimensions, and other requirements drive the design.

The three main electronic components of the device are depicted in Figure 7.1, a simplified line drawing of the lifting device. The device should provide imaging of the complete surgical field using a single camera, denoted by A. In Figure 7.1 it is centrally placed, but its exact position is determined in Chapter 8. Secondly, the device should provide light using LED's. Thirdly, the camera signal, camera power supply, and LED power supply should be processed outside the abdominopelvic cavity and wired together to a single USB-A connection, denoted by C. It is a female receptacle in the drawing, but could also be a male plug. The best choices for these three electronic subsystems are described in separate sections below.
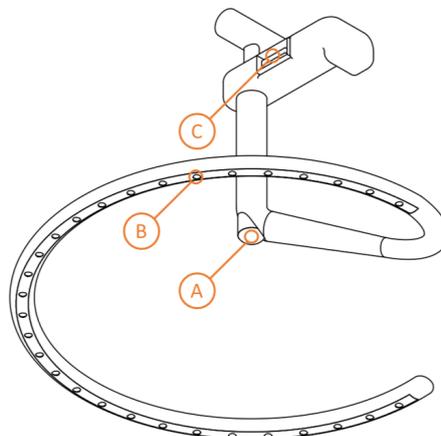
Figure 7.1: The three main electrical components of the design: **A)** Camera, **B)** LED strip, **C)** USB connection

The aim of the electronics is specified in the project goal in Section 2.2: to provide a clear view of the surgical field that substitutes for the laparoscope. This aim is further specified in the design specifications in Chapter 3. The five requirements that apply to the electronics are listed below. The rationale for every requirement has two parts, one for the camera and one for the LED lighting.

- **P2** Visibility: The chosen camera should provide better visibility than a state-of-the-art laparoscope from 10 years ago. This will be verified by objectively testing the camera and comparing it

to multiple laparoscopes on four imaging quality factors in Chapter 12.

The quality of the imaging provided by the camera is highly dependent on the lighting. There are four main parameters to consider: intensity, angle, hardness, and colour/temperature. These four parameters and their optimum for this lifting device will be explored in Section 7.3

- **P3** Product temperature: The surface temperature of the device may not exceed $41°$ at any point. Since the camera sensor will likely be positioned close to the surface of the device, its temperature may not exceed $41°$.

The light source will likely be positioned close to the surface of the device as well, and consequently, its temperature may not exceed $41°$. The temperature of the LEDs can be regulated by controlling the electrical input.

- **C1** Low upfront purchase price: The complete device should be low-cost, and that applies to the camera as well. The camera's purchase cost may not exceed 25% of the total cost, i.e. €60.

For the lighting system, choosing LED lighting ensures that this requirement is met.

- **D2** Insertion diameter: The part of the lifting device that enters the abdomen, which will contain the camera sensor, may not exceed a diameter of 12 [mm]. Consequently, the camera's outer dimensions near the sensor must be such that it fits inside a 10 [mm] cylinder, based on Chapter 9.

Similarly, the LED lights will be part of the lifting device that enters the abdomen. Consequently, the LED's outer dimensions must be such that it fits inside a 10 [mm] cylinder.

- **M2** Data-/power-connection: The requirements specify that the data connection and power connection must go through a single USB-A port. The chosen camera must thus contain a PCB that converts the signal to USB format.

The chosen LED lighting system must also be powered through a standard USB-A connection, which can provide a maximum of 7.5 [W], delivered as 1.5 [A] at 5 [V].[1]

7.2. Camera

The most eye-catching feature of the lifting device is its integrated camera. This camera should provide visibility of the surgical field during BTL procedures such that no laparoscope is needed anymore. This section will which type of camera best fits the requirements from Section 7.1.

For clarity, "camera" and "camera sensor" are two separate terms. The cameras considered for this application generally consist of two parts. The first part is the camera sensor, which contains the image sensor and lens(es). The second part is a printed circuit board (PCB) which processes the signal from the image sensor. Some cameras combine the sensor and PCB, and some cameras have the sensor split from the PCB (Figure 7.2 for example[2]) connected by a Flat Flex Cable (FFC).
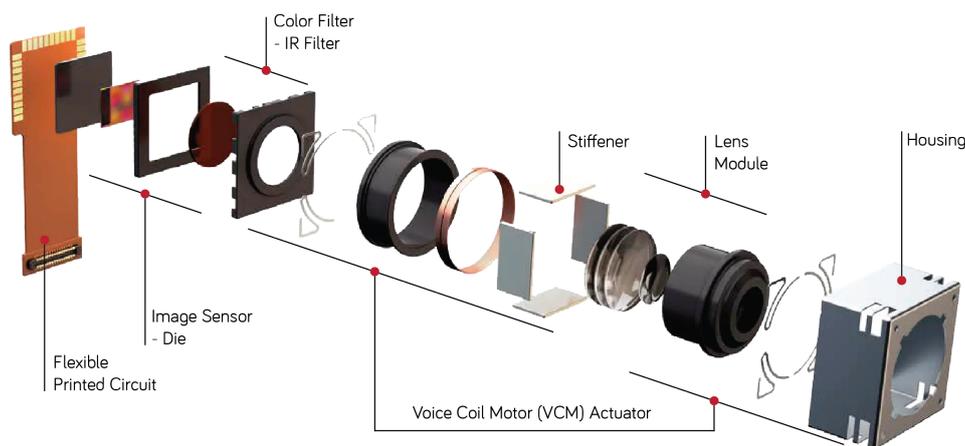
Figure 7.2: Example of a CMOS auto-focus camera sensor[1].

---

[1]https://metalicon.com/usb-fast-charging/
[2]https://prostech.vn/industries/electronics-industries/sensor-device/image-sensor-camera-module/

Variety of cameras

The camera should be a commercially available, off-the-shelf part (also called a module), as that makes production easier and better allows for repairs. A huge variety of such camera modules is available online. An example of a camera module and its different parts is shown in Figure 7.2. This section makes several distinctions between different types of camera modules and indicates which properties are most likely to fulfil the applicable requirements.

Type of sensor

The main hardware distinction between camera modules is the type of sensor. Sensors are characterised by their size and type of technology. The image quality of camera sensors increases with sensor size. There are two types of technologies commonly employed in digital camera sensors: Charge Couple Device (CCD) and Complementary Metal-Oxide Semiconductor (CMOS). [77, 78]

CCD sensors operate on the principle of charge transfer. In a CCD sensor, incident light photons strike individual photosensitive elements (pixels), generating electrons in response to the photon energy. These accumulated electrons are then shifted and transferred in a serial or parallel manner to a readout amplifier at the sensor's periphery. This charge is converted into a voltage signal, amplified, and digitized to create a digital image. [79]

CCD sensors have traditionally been the preferred choice for imaging applications due to their superior sensitivity and lower noise levels. They excel in capturing high-quality images in low-light conditions and also offer excellent dynamic range, allowing them to record subtle variations in light intensity accurately [80]. However, CCD sensors tend to be slower, more power-hungry, generate more heat during operation, and are generally more expensive compared to current CMOS sensors. This limits their utility in this lifting device.

In contrast, CMOS sensors integrate active amplification and signal processing at the pixel level. Each pixel in a CMOS sensor comprises a photodetector and an amplifier, allowing it to capture and amplify the incoming light's signal individually [81]. This architecture offers advantages in terms of speed and power efficiency and is suitable for existing large-scale integrated circuit production processes, hence the production cost is low. Furthermore, while sensitivity and noise performance traditionally lagged behind CCD sensors, advancements in CMOS technology have narrowed this gap.

CMOS sensors have gained prominence in recent years [82]. Their smaller size, lower power consumption, and faster readout speeds make CMOS sensors well-suited for portable devices. It is now the sensor type of choice for the smartphone and tablet industry [83]. The development and mass production of CMOS sensors for the smartphone and tablet industry means high-quality, reliable sensors are available at very low cost.

In conclusion, CMOS sensors are more suitable for the camera module of this lifting device because they are cheaper, faster and generate less heat during use.

Focus mechanism

The focusing mechanism in camera sensors plays an important role in capturing sharp and clear images. Two approaches are commonly used: fixed-focus and auto-focus. [84]

Fixed-focus, as the name suggests, refers to a camera sensor with a predetermined, fixed focal distance that is set during the manufacturing process. The lens elements are positioned at a specific distance from the image sensor. This results in a compact, lightweight design. Furthermore, fixed-focus cameras handle vibrations better and are better for RGB depth alignment.

However, fixed-focus cameras have limitations when it comes to capturing subjects at varying distances. They are at their best for scenarios where the typical shooting distance is known in advance.

On the other hand, auto-focus is a dynamic and adaptive focusing system that continuously adjusts the lens position to ensure sharpness for objects at varying distances from the camera. Auto-focus cameras utilize various techniques to measure the distance between the camera and the subject: phase detection, contrast detection, or the use of ultrasonic waves. These methods enable the camera to calculate the required lens position for optimal focus.

However, auto-focus sensors are more complex than fixed-focus sensors and thus more expensive. Additionally, the focus mechanism (typically piezoelectric or voice coil motors) consumes extra power and can produce a lot of heat during operation.

In conclusion, fixed-focus camera sensors are more suitable for the camera module of this lifting device because the approximate shooting distance is known (will be calculated in Chapter 8) and the sensors are cheaper and generate less heat during use.

PCB placement

Camera sensors produce an analogue voltage signal in response to photons hitting the pixels, proportional to the intensity of the incident light. This analogue voltage signal is converted into a digital signal using an analogue-to-digital converter (ADC) inside the sensor. The next step is to convert this signal from its RAW format to JPEG using digital signal processing (DSP) [85], where digital image signal parameters are optimized through a series of algorithms.

The DSP requires a PCB. As briefly touched upon in the introduction of this section, some cameras have the PCB directly connected to the camera. The camera is a single part which can be directly connected to a USB cable. Such a configuration is shown in Figure 7.3a. Some camera modules, produced specifically for endoscopes, even have LED lights surrounding the sensor, as shown in Figure 7.3b.

If the camera does not have an integrated DSP, the signal has to be transmitted by DVP or MIPI interface. This signal is processed and converted for USB connection by a separate PCB. This configuration is shown in Figure 7.3c.

(a) Camera with integrated PCB   **(b)** Camera with integrated PCB & LEDs   **(c)** Camera with separate PCB

Figure 7.3: Three possible configurations for small camera modules.

The PCB is the element of the camera module that generates the most heat (assuming a CMOS fixed-focus camera sensor) because it contains components such as DSP processors, memory chips, and voltage regulators that all have resistive losses. Hence, it is advantageous to split the PCB from the sensor. The heat-generating PCB can be put in a section of the lifting device outside of the abdominopelvic cavity, while the camera sensor itself is inside of the abdominopelvic cavity. Furthermore, the PCB is usually larger in dimension than the sensor. Splitting the sensor from the PCB can therefore help to keep the dimensions of the lifting device inside the abdominopelvic cavity small.

Resolution & frame rate

Requirement P2 on visibility has many factors that can only be determined by testing the camera. However, a requirement for the resolution can be set using guidelines from the World Laparoscopy Hospital (WLH). Resolution refers to the number of pixels that the camera sensor can capture, expressed in megapixels (MP). The WLH states that Full HD imaging (1920 x 1080 pixels) offers a superior viewing experience for surgeons [3]. This requires a camera with a resolution of at least 2 MP.

Additionally, a requirement for the amount of frames per second (FPS) can be set. FPS is the frequency at which consecutive images are recorded, i.e. the number of pictures that are recorded every second. The two most common options are camera sensors that record at 30 FPS or at 60

---

[3]https://www.laparoscopyhospital.com/HD-Endoscopic-Camera.html

FPS. The WLH states that video streaming at 60 FPS may be the highest standard readily available for acquiring and displaying images. However, 30 FPS will suffice for this lifting device for several reasons. The main advantage of 60 FPS is to reduce motion blur, but the camera is not expected to move much during procedures. On top of that, 30 FPS sensors have higher video quality in dim light conditions, generate less heat, and are generally less expensive.

The surgeon's visibility can be further increased by choosing a camera sensor with a wide field of view (FOV). Camera FOV is the maximum amount of area that a camera can capture in a single frame. A camera sensor with a wider FOV captures more of the surgical field.

Selected camera

Based on the four distinctions made above, the camera module for the lifting device should use a CMOS sensor, with a fixed-focus lens system, and a separate PCB for the DSP such that the camera module has only its sensor inside the abdominopelvic cavity. The sensor should have a wide FOV, a resolution of at least 2 MP (to capture full HD), and record video at 30 FPS. These camera properties ensure the selection of a camera that is most likely to meet the five applicable requirements.

The two largest manufacturers of CMOS sensors are Sony with its IMX-series and Omnivision with its OV-series, which together hold a 40% market share [4]. Their camera sensors are integrated into many smartphones, tablets, and laptops. Camera modules with their sensors are widely offered online. The cheapest option is to directly import a camera module from the country of origin, Mainland China. Many Chinese vendors offer camera modules with a USB-A connection that can be ordered per piece. The price ranges from €10 to approximately €150 per piece, with discounts possible for batch orders.

Inquiries with Chinese vendors resulted in two camera modules with the most potential. Both modules are designed to the small form factor (SFF) standard for use in embedded systems, such as several smartphones released in 2017. They are shown in Figure 7.4. Both sensors use the same physical PCB, although the default board settings differ.

The first camera module is equipped with a 5693 CMOS sensor from OmniVision that has a resolution of 5 MP. The size of the sensor is $1/4$ inch diagonally, or 6.35 [mm]. It has a fixed focus lens system with a FOV of $120°$. It can record Full HD 1080p video at 30 FPS or 720p at 60 FPS. It has a maximum power consumption of 300 [mW] at a voltage of 5 [V]. The sensor, which measures 8.5 x 8.5 x 5.8 [mm], is split from the PCB by a 165 [mm] long and 8 [mm] wide FFC. The small sensor and long FFC make this camera module well-suited for use in laparoscopic settings: The sensor can be placed in a small diameter instrument inside the abdominopelvic cavity where it does not generate a lot of heat, while the PCB can stay on the outside. This camera module can be imported from Mainland China for approximately €20 as of September 2023[5]. Due to the small sensor size and low purchase price, this sensor was ordered to be used for prototyping.

Another advantage of this camera module is that the sensor's lens is made of plastic. Traditional laparoscopes use many glass lenses which are susceptible to fracture if the device is dropped because glass is a brittle material. However, the lens of this camera module is made from Mitsui Chemical's APEL™, a ductile plastic with excellent optical properties.

The second camera module is equipped with an IMX 258 CMOS sensor from Sony that has a resolution of 12 MP. This sensor is slightly larger at $1/3.06$ inch diagonally, or 8.3 [mm]. It has a fixed focus lens system with a FOV of $135°$. It can record Full HD 1080p video at 60 FPS. It has a maximum power consumption of 300 [mW] at a voltage of 5 [V]. The sensor, which measures 8.5 x 8.5 x 7.6 [mm], is split from the PCB by a 160 [mm] long and 8 [mm] wide FFC. The dimensions are therefore similar between the two camera modules, but the height of this sensor is 35% bigger compared to the OmniVision 5693. The lens of the sensor is also made from APEL™.

The price of this camera module is approximately €50 as of September 2023[6], which is significantly more expensive but still within the requirements. It was decided to not use this camera module for initial prototyping. Nevertheless, for further prototyping, a switch from the OmniVision camera module to the Sony camera module should be considered.

---

[4] https://evertiq.com/design/33804
[5] aliexpress.com/item/1005005178412080.html
[6] aliexpress.com/item/1005005583033827.html
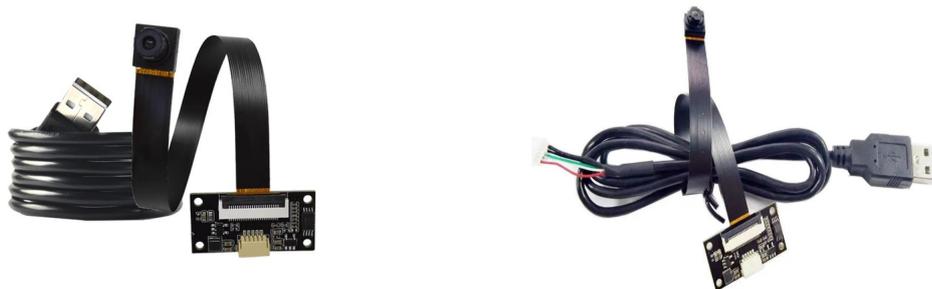
(a) OmniVision 5693 CMOS sensor, fixed-focus, 5 MP, $120°$ FOV   (b) Sony IMX 258 CMOS sensor, fixed-focus, 12 MP, $135°$ FOV

Figure 7.4: The two USB-compatible camera modules that best meet the applicable requirements.

7.3. LED lighting

Laparoscopic devices have to provide their own source of lighting since the inside of the abdominopelvic cavity is devoid of light. Traditional laparoscopes achieve this using fiber-optic cables in the tip, surrounding the lens [86]. The cables are connected to a fiber-optic light source which supplies white light. Such an expensive system is necessary because there is little space at the tip of the laparoscope. Cheap laparoscopes designed for low-resource settings replace the fiber-optic cables with small LEDs on the tip, but as a result, the tip becomes very hot [34].

The lifting device has an important advantage over laparoscopes here. The circular hook that grips the abdominal wall from the inside can also be used to place light sources. This creates a ring of light inside the abdomen, similar to a photographer's ring light device [7]. Ring lights are used in photography to achieve even lighting, and putting the camera in the centre eliminates glare or shadows [87]. Furthermore, spreading the light source over a large area instead of the tip frees up space for the camera sensor and helps with temperature management.

For these reasons, LED lighting in the loop is the logical choice for this lifting device. It eliminates the expensive fiber-optic light system while having more space to manage the issues typically associated with LED lighting for laparoscopes.

The four lighting parameters

The four lighting parameters mentioned in Section 7.1 under requirement P2 are the fundamental characteristics of light for photography and videography. Understanding these four parameters will help to determine what type of LED lighting is most suitable for the lifting device. [88]

Intensity

Intensity is commonly known as brightness. The intensity of a light source is expressed in lumens [lm], whereas the amount of light hitting a specified area is measured in lux [lx]. One lux is equal to $1 \; [lm/m^2]$.

Light intensity has a large effect on image quality. If the intensity is too low it results in underexposed footage, leading to dark and noisy videos with reduced clarity. Additionally, low light can cause motion blur. In contrast, excessive light intensity can lead to overexposure, causing lower contrast in the brightest areas of the image, lens flares, and a washed-out or white appearance. Based on interviews, Indian rural surgeons mainly struggle with laparoscopes providing too little light.

Surgeons should have at least some control over the intensity of the light because it has such an effect on image quality. However, based on scientific literature, a baseline for light intensity can be deduced. A 2017 publication on the design of an in vivo laparoscope used a "conservative estimate" for the illuminance of 10.000 [lx] at 100 [mm] [89]. Another publication measured a State of Care (SOC) laparoscope at 10.000 [lx] at 60 [mm] [32]. For this lifting device, 10.000 [lx] at 100 [mm] will be used since that standard suffices for both publications.

The camera module selected in Chapter 7 has an advertised FOV of $120°$, with which it can capture an area of 0.036 [m^2] at a 100 [mm] distance from the target. To completely illuminate this area with 10.000 [lx], a light source with a strength of 360 [lm] is required.

---

[7] https://thriveproductstudio.com/ring-lights-product-photography/

Angle

Angle specifies the direction of the light on the target. Expert GILLS surgeon J. Gnanaraj indicated that it is preferable to have the light parallel to the camera. Lighting a target from the side can produce unwanted shadows. A parallel light path, in combination with the circular setup of the LED lights, ensures the least amount of shadows or flares. The angle is therefore subject to the angle of the camera sensor.

Hardness

The third parameter is the hardness of the light, commonly known as quality. The quality of light can not be measured. Instead, it is described based on visual perception; light is either soft or hard. As a rule of thumb, light sources smaller than the subject cast hard shadows and light sources bigger than the subject cast softer shadows. The bigger the light source relative to the subject, the softer the light. [88]

Soft light is preferred because it reveals more of the image, and colours appear richer and more realistic. Hard light is typically used as an artistic effect, but the added shadows are bad for objective imaging. Although hardness is not quantifiable, it does reveal a big advantage of this lifting device over traditional laparoscopes. Laparoscopes typically have a very small light source and therefore produce relatively hard images, whereas this lifting device has a large light source in the loop and can therefore produce softer images.

Colour temperature

The final parameter is the colour temperature of the light. The colour temperature of light is measured in Kelvin [K] and describes its warmth or coolness. Lower Kelvin values (e.g., 2500 [K]) represent warmer, reddish light. Higher Kelvin values (e.g., 5000 [K] and above) indicate cooler light, more akin to daylight.

Cooler light is preferred for surgeries[8], with an optimal temperature between 5000 and 6000 [K] [90]. The exact temperature is less relevant. For example, previous research found no statistically significant difference between a laparoscopic light source of 4500 and 5100 [K] [91].

Type of LED

There are three main types of LED chips[9]. The first type is the Dual In-Line Package (DIP) LED. These are the traditional straw hats. Their design consists of a diode in a clear hard plastic case, from which two parallel connecting pins protrude. The colour of the housing determines the colour of the light emitted by the LED. Although DIP LEDs are still used today, their low luminous efficiency (compared to the latest LEDs [92]) means they are only used as indicator lights.

The second type, and most common, is the Surface Mounted Diode (SMD) LED. The LEDs are soldered onto a PCB [93]. They are brighter than DIP LEDs and more compact. The two most common types of SMD chip sizes are SMD 3528 and SMD 5050, with a 5 [mm] diagonal and a 7 [mm] diagonal respectively. Multiple SMD LEDs can be combined to form multicolour LED chips or LED strips [94]. SMD LEDs typically produce $60\text{-}80$ [lm/W]. They emit light unidirectionally but can achieve higher beam angles when evenly distributed. They have accurate colour rendering with a typical Colour Rendering Index (CRI) of 80%, and the most stable performance in adverse environmental conditions [95]. However, the drawbacks are the heat generated at the chip-to-board transition and SMD LEDs typically have less compact packaging than COB LEDs.

The third type is the Chip On Board (COB) LED. The design is based on the integration of several LEDs in one structure, thereby forming a small LED panel [96]. They have the highest lighting efficiency of the three types of LED. Their light output can exceed 150 [lm/W] and they can provide a wide beam angle of up to $160°$. A COB LED can only emit a single colour and has a CRI of 90% [97]. Despite the high diode concentration and resulting light output, the COB design allows for efficient heat dissipation, making it suitable for fixtures that need to remain on for extended periods. Another durability advantage is their resistance to voltage fluctuations in the electrical grid. These advantages make COB LEDs the most suitable type of LED for this lifting device.

---

[8]https://austinpublishinggroup.com/obstetrics-gynecology/fulltext/ajog-v1-id1014.php
[9]https://ledhut.co.uk/blogs/news/the-definitive-guide-to-led-light-bulbs-and-spotlights

LED circuit design

The final consideration for the LED lighting system is the circuit design, which is based on LEDs' individual electrical properties. LEDs are diodes. When forward biased, the current flows from the anode to the cathode of the LED and it outputs light. The voltage at which this occurs is called the forward voltage. No current flows through the LED until the forward voltage is reached, after which current flow increases exponentially. This non-linear I-V curve is shown in Figure 7.5 for several colours. The forward voltage drop is often measured for a specified amount of forward current, typically 20 [mA].

The colour of an LED is determined by the semiconductor compound used in forming the PN junction, and not by the colour of the LED's plastic body (although these can be slightly coloured to enhance light output). Different semiconductor compounds require different forward voltages, as shown in Figure 7.5. Most common LEDs require a forward operating voltage between 1.2 to 4.0 [V] with a forward current rating of about 5 to 30 [mA]. LEDs that provide white light typically require a forward voltage between 3.3 and 4.0 [V].
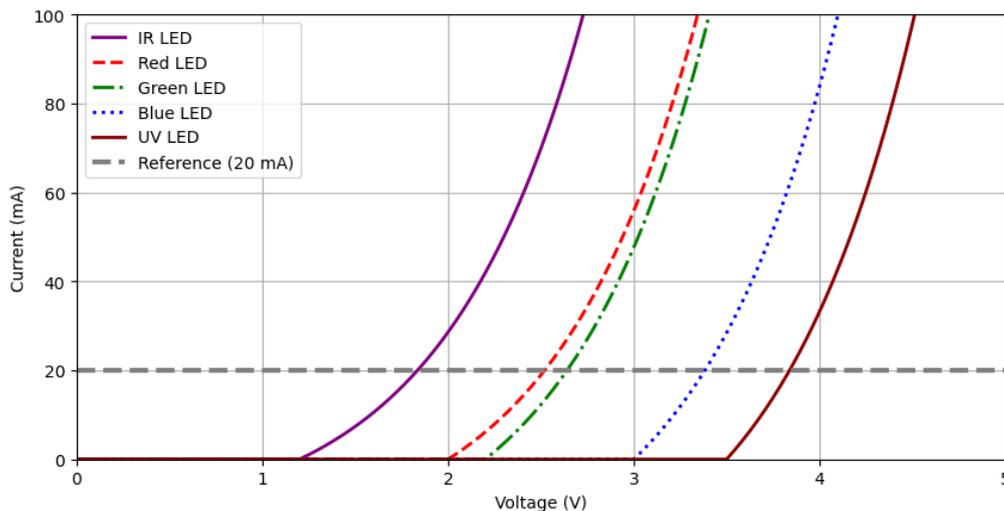
Figure 7.5: LED I-V characteristics curve

The brightness of the LED varies with the amount of current. More current means a brighter LED, approximately linearly, but too much can overheat the LED or even instantly destroy it. Furthermore, above the forward voltage, small changes in voltage result in relatively large changes in forward current. Therefore, in LED circuits, the current is controlled instead of the voltage, and the forward voltage is taken as a fixed value. Three basic current limiting techniques exist.

The first technique is LED drivers. LED drivers are power supplies dedicated to LED circuits that exist in two variants: constant voltage LED drivers and constant current LED drivers. The voltage or the current of the power supply is limited within a safe range for the LEDs.

The second option is parallel circuiting. For parallel-connected LEDs, the voltage across each LED is the same and the total current is the sum of currents through each LED, whereas in a series connection, the same current flows through each LED and the total voltage equals the sum of the voltages across each LED. This can be used to lower the effects of voltage fluctuations.

The third option is the use of current-limiting resistors. The required resistance R for an LED circuit is calculated using Equation 7.1, where V_S is the supply voltage, V_F the total forward voltage (must be lower than the supply voltage), and I_F is the required forward current.

$$R = \frac{V_S - V_F}{I_F} \tag{7.1}$$

The complete LED system has to be powered by single USB-A connection, which can provide a maximum of 1.5 [A] at 5 [V] (only 300 [mW] is required for the camera module). This leaves two options for the LED circuit.

The first option is a custom LED circuit based on multiple LED chips, rated at 65 [lm] per chip, which would result in the highest total light intensity. These LEDs require a forward voltage of 3.7 [V] and have a maximum forward current of 120 [mA]. Such LED chips are cheap (approximately €0.50 per 100 pieces as of September 2023[10]) and have dimensions of 5.7 x 3.0 [mm].

The 5 [V] USB 3.0 charging port with 1.5 [A] can be stepped down to 3.3 [V] using resistors. Connecting all LED chips in parallel, tens of LED chips can be connected to this light source, which provides plenty of light intensity. A single communal resistor can be placed up front, because all LED chips have the same colour, or individual resistors can be placed near every LED, shown in Figure 7.6b and Figure 7.6a respectively.


(a) Circuit with 5 parallel LEDs and 5 resistors   (b) Circuit with 5 parallel LEDs and a single resistor
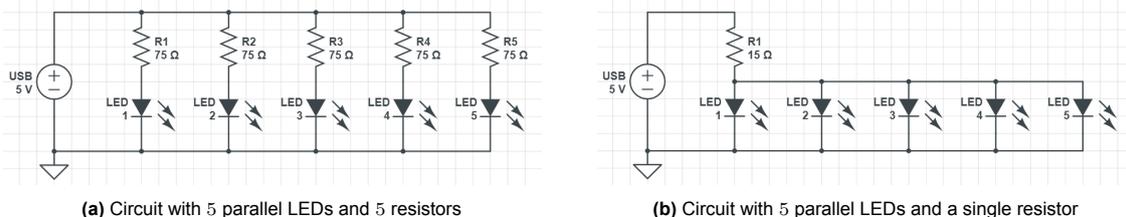
Figure 7.6: Two example LED circuits.

Individual resistors are a safer option because the circuit is not susceptible to manufacturing differences between different LED chips, which can lead to inconsistent brightness and a cascade failure mode. However, resistors generate more heat than LEDs and hence the single communal resistor option allows for better temperature management. The resistor can be placed outside the body, which reduces the local surface temperature. Such a custom circuit is preferred for the final design but more complicated than the alternative, pre-assembled LED strips, and therefore not used during prototyping.

The alternative is a pre-assembled LED strip. The advantage is that these strips are plug&play and do not require any soldering. These strips are flexible, have a sticky side, and can be cut to length because they have the circuit design as shown in Figure 7.6a. However, such LED strips provide less light than a custom circuit. They come at 5 [V] and 12 [V].

12 [V] strips are not brighter than 5 [V] strips because of the higher voltage, as voltage depends on colour and brightness is determined by the forward current. However, available 12 [V] strips have more LEDs per meter and therefore a greater [lm/m] rating. 12 [V] strips can be connected to a 5 [V] USB-A port using a step-up boost converter. However, when using a step-up converter, little current will be available (approximately 0.625 [A] assuming 85% efficiency) which limits the maximum length of the strip. Most 12 [V] strips are rated at around 10 [W/m] and hence the maximum length of the 12 [V] LED strip that can be powered with a USB 3.0 charging port and a 5V to 12V step-up converter is approximately 0.6 [m]. Both 5 [V] and 12 [V] LED strips will be trialled for the design of this lifting device.

Selected LED lighting
COB LED lights are commercially available in a wide variety of configurations in terms of dimensions, LED placement and power rating. Similar to the camera modules, the cheapest option is to directly import LEDs from the country of origin, Mainland China. The requirements for the chosen LED lights are that the type is COB, with a total strength of 360 [lm], and colour temperature between 5000 and 6000 [K]. The part of the loop that has to provide light has a length between 300 - 350 [mm], see Chapter 8. Consequently, a light intensity of approximately 1100 [lm/m] is required.

Several strips were ordered to test during prototyping, and the three most prominent are listed here.

The first is a 5 [V] COB LED strip used for the first 3D-printed prototype, shown in Figure 7.7a. It has a colour temperature of 6000 - 6500 [K]. The power consumption is 5.5 [W/m]. The strip is 8 [mm] wide and the beam angle is $120°$. It has a dim function which gives the surgeon control over the brightness of the light. However, the maximum light intensity is 800 [lm/m], which is not enough to fulfil the light intensity standard. This LED strip is therefore only used for demonstration purposes and not for the

---

[10]aliexpress.com/item/4000401630571.html

final design. This LED strip can be imported from Mainland China for approximately €5 per meter as of September 2023[11].

The second is a 12 [V] COB LED strip with 480 [LEDs/m], shown in Figure 7.7b. It has a colour temperature of 6000 [K]. The power consumption is 11 [W/m]. The strip is 8 [mm] wide and the beam angle is $180°$. The light intensity is listed at 1250 [lm/m], which suffices for the final design. It can be imported from Mainland China for approximately €10 per 5 meter as of September 2023[12].

The third strip is a 12 [V] COB LED strip with 528 [LEDs/m], shown in Figure 7.7c. It has a colour temperature of 6000 [K]. The power consumption is 14 [W/m]. The strip is 10 [mm] wide and the beam angle is $180°$. The light intensity is listed at 1550 [lm/m] and is dimmerable. It can be imported from Mainland China for approximately €4 per meter as of September 2023[13].

(a) 5 [V] 320 [LEDs/m] COB   **(b)** 12 [V] 480 [LEDs/m] COB   **(c)** 12 [V] 528 [LEDs/m] COB

Figure 7.7: The three LED strips used for prototyping.

7.4. Connections & Software

The final parts of the electronic system are the USB connection and the software. The camera signal, camera power supply, and LED power supply should rely on a single USB-A connection. Furthermore, the software used to interface with the lift device has a large influence on its usability.

USB connection

The heat-generating electronic components, such as the camera's PCB (and possibly the LED circuit's resistors), are stored in a dedicated part of the lift device, away from the surgical area, called the electronics housing. This helps to keep the lift device cool where it is in contact with patients.

The drawing in Figure 7.1 shows a female USB-A receptacle. However, interviews with Indian rural surgeons revealed that they much prefer a single cable with a male USB-A plug. Such a cable makes chemical sterilisation of the lifting device much easier and can be connected to almost any type of laptop, the monitor of choice in low-resource settings.

The electronics housing of the two prototypes contains two elements: The camera's PCB and the power plug for the LED strip. These two should be combined into a single USB-A connection. This requires many chunky off-the-shelf components or a custom circuit, which fell outside the scope of this project. The prototypes thus use two USB-A cables, one for the camera and one for the LED strip.

Software

Due to the choice of electronic components, the lifting device is plug&play when connected to any laptop running a Microsoft Windows or Linux operating system. These operating systems recognize the USB camera module which can directly be accessed using the built-in camera app. The default is Full HD imaging at 30 FPS, which can be increased to a 1440p display resolution. Furthermore, the LED system draws current from any type of USB connection. Hence no special software is required to operate the lifting device.

However, dedicated imaging processing software offers several advantages. Such software has a deeper understanding of USB camera modules and therefore provides better image quality and allows

---

[11]aliexpress.com/item/1005003337251096.html
[12]aliexpress.com/item/1005005191166730.html
[13]aliexpress.com/item/4000145232270.html

for custom functions. The image quality of different camera modules will be tested for three different software in Chapter 12: AMCap, Resolume Avenue, and TouchDesigner.

Three examples of custom functions will be given below. These functions enhance the usability of the lifting device and are not possible using a default camera app. They can be assigned to specific buttons on the laptop or even to external devices.

All three imaging software allow for the image to be rotated by $360°$, in increments of a single degree. That means the image on the display can be flipped by $180°$ if the lifting device is rotated around its connector, see Section 8.3 on camera position. Furthermore, the image can be corrected per degree if the lifting device is slightly misaligned due to a small rotation around its vertical axis.

The second custom function is recording and streaming, only possible with Resolume Avenue. The images of the procedure can be streamed without delay or recorded, which is a great asset in educational settings. Students or other surgeons can watch another surgeon perform a live procedure, or rewatch the recording of a procedure.

Finally, the most important custom function according to Indian rural surgeons is digital zoom. All three imaging software allow a digital zoom of at least 250%. The digital zoom function can be assigned to laptop keys, but expert GILLS surgeon J. Gnanaraj remarked that he would prefer a Bluetooth foot pedal because digital zoom would be frequently used during the procedure. This functionality is possible with Resolume Avenue and TouchDesigner. It allows the surgeons to control the zoom level, without taking their hands off the instruments.

The drawback of dedicated imaging software is that the cost can be up to €100 per user, i.e. per lifting device. That means 40% of the budget for the lifting device, according to requirement C1, would be spent on software. It also requires that every surgeon who uses the lifting device downloads and installs the software and loads the optimal settings and custom functions into it, which conflicts with requirement E1.

The value of dedicated imaging software will be determined based on the image quality tests in Chapter 12 and the user tests in Chapter 14. The final prototype will be trialled with both the default camera app and the three aforementioned software, to determine if increased image quality and custom functions outweigh the significant added cost and difficulty of installation.

8
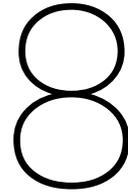
Dimensional analysis

8.1. Applicable requirements

This chapter describes how the geometry of the lifting device was calculated. First, the required operational volume is calculated which serves as input for the outer dimensions of the lifting device. The second step is to position the electrical components from Chapter 7 and adjust the frame accordingly. The resulting design is presented in Section 8.4.

The dimensions of the frame of this lifting device are based on four requirements from Section 3.2, which are listed below with a brief rationale.

- **P2**   Visibility: The first part of requirement P2 states that the operational volume created using the lifting device should be at least equal to the volume created during traditional laparoscopy.
- **D2**   Insertion diameter: The required diameter of insertion may be no more than 12 [mm].
- **M1**   Compatibility with extractors: The lifting device should be compatible with the RAIS system, including its option to rotate the device around the lateral axis of the connector.
- **M3**   Adaptability to patients: The device should be designed for the Indian female population.

8.2. Outer dimensions

This section describes the factors that influence the outer dimensions of the lifting device, which set the boundaries for the size and form of the lifting device. The primary function of any lifting device is to lift the abdominal wall and free up space inside the abdominopelvic cavity where the surgeon can perform the procedure. This free space is called the operational volume and drives the sizing of the lifting device. The shape is further influenced by the need to minimize insertion friction and requirement D2 on insertion diameter.

It is important to note that this section uses two assumptions about the design based on the structure, materials, and production of the lifting device. The first assumption is that the frame of the lifting device will be created from a circular metal tube. The second assumption is that the minimum corner radius of the loop must be greater than twice the tube diameter. These assumptions are explained in Chapter 9 and Chapter 10 respectively.

Operational volume

Operational volume is created by pneumoperitoneum in traditional laparoscopy. Requirement P2 on visibility requires the lifting device to create an operational volume that is at least equal to pneumoperitoneum during traditional laparoscopy. The required operational volume is determined using methods from previous research. [39, 55]

The operational volumes created by pneumoperitoneum, the traditional method, and by a lifting device are presented in Figure 8.1. The shapes of these volumes are assumptions. Previous research has no consensus about the shape of the operational volume. The assumptions from recent research are followed in this thesis as they are based on observations on an abdominal laparotomy model [39].
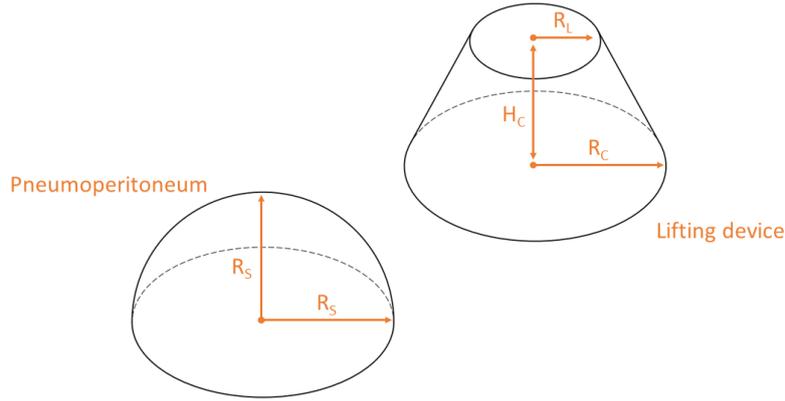
Figure 8.1: The operational volume created using pneumoperitoneum (left) and using a circular lifting device (right). The volume created by pneumoperitoneum is assumed to be a perfect half sphere, with equal base radius and height R_S. The volume created by the lifting device is assumed to be a truncated cone, with base radius R_C, height H_C, and top radius R_L.

The operational volume created by pneumoperitoneum, V_P, is calculated with Equation 8.1. R_S, the base radius of the half-sphere, is the transverse abdominal radius which is defined as the linear distance between the midpoint of the abdomen to the peritoneal edge of the lateral abdominal wall [39].

$$V_H = \frac{4\pi}{6} R_S{}^3 \tag{8.1}$$

The operational volume created by the lifting device, V_L, is calculated with Equation 8.2. The base radius of the truncated cone R_C is the transverse abdominal radius, and R_L represents the radius of the loop of the lifting device. H_C is the height by which the lifting device is raised.

$$V_L = \frac{\pi}{3} H_C \left(R_C{}^2 + R_C R_L + R_L{}^2 \right) \tag{8.2}$$

A second assumption is that the base radii of the two operational volumes for any given patient are equal, i.e. $R_S = R_C$. In previous research, the two theoretical operational volumes were then set to equal each other. This allows for the elimination of the height variable H_C such that the radius of the lift device can be optimised as a function of the base radius as shown in Equation 8.3.The resulting radius coefficient C_R is between 0.814 [39] and 0.85 [55].

$$R_L = C_R * R_C \quad \text{assuming} \quad R_C = R_S \tag{8.3}$$

However, for the dimensioning of this lifting device, the two operational volumes will not be set equal to each other. Instead, a minimum H_C will be adhered to such that the two operational volumes are at least equal. The surgeon can then use the height of the lifting device to tweak the camera position to their liking. The minimum lifting height $H_{C_{min}}$ is calculated in Equation 8.4 and is a function of the base radius R_C and lifting device outer radius R_L. Expert GILLS surgeon J. Gnanaraj indicated that the height H_C of the STAAN lifting device during use is typically 100 - 150 [mm].

$$H_{C_{min}} = 2R_C{}^3 \left(R_C{}^2 + R_C R_L + R_L{}^2 \right)^{-1} \tag{8.4}$$

Previous research has used CT scans to determine the average transverse abdominal radius. The radius of the human body differs with age. Young children have a mean transverse abdominal radius of 60 [mm] and adults average 105 [mm] [39]. Another study puts the mean transverse abdominal radius of the adult body at 103 [mm] [55]. Based on these studies, the mean transverse abdominal radius used for further calculations is 104 [mm], as BTL procedures are predominantly performed on adult patients.

Based on the mean base radius and known range of heights, a graph for the minimum lifting device radius can be created as shown in Figure 8.2. The lifting device's radius is a function of the lifting height, given that the base radius is 104 [mm]. The radius of the lifting device design should be above

the orange line. The limiting case is at the minimum lifting height of 100 [mm], which means that the minimum radius of the lifting device should be approximately 70 [mm].

Professor P.R. Culmer, responsible for the design of RAIS [38], indicated that rural surgeons prefer a small (< 60 [mm]) loop radius. Therefore, the radius of this lifting device is set to the minimum of 70 [mm].
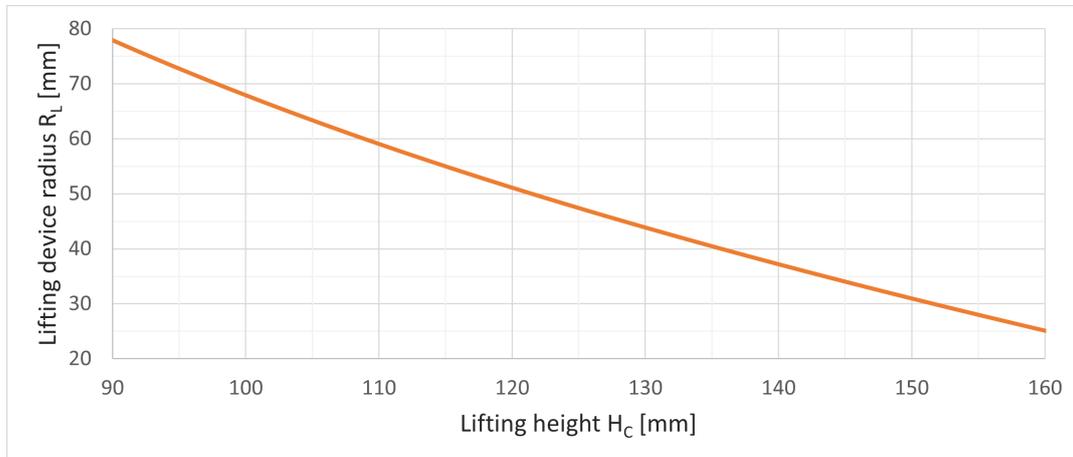
Figure 8.2: The minimum required radius of the lifting device R_L as function of the lifting height H_C.

Loop shape

The first factor that influences the shape of the lifting device is the circle circumference C_L of the loop, which represents the length of the loop. Three possible configurations are shown in Figure 8.3. Previous research found that of three other configurations, $1/2$, $3/4$, and $5/6$, the shorter loops decrease resistance during insertion [55]. Furthermore, a shorter loop significantly decreases the chance of peritoneal injury: The $5/6$ had an injury rate of 45%, the $3/4$ had an injury rate of 13%, and the $1/2$ had an injury rate of 0%. Furthermore, a shorter loop requires less material and is thus cheaper and lighter.

However, a longer circle circumference loop has two distinct advantages as well. A longer loop better supports the abdominal wall to create the truncated cone shape, which results in a larger operational volume. Secondly, a longer circle circumference also means more space for LED lighting to illuminate the operational volume from multiple angles, which eliminates shadows.

Based on these conflicting design requirements, the circle circumference on the lifting device is set to be $3/4$ to ensure optimum visibility while keeping the risk of peritoneal injury low.

$1/2$ $2/3$ $3/4$
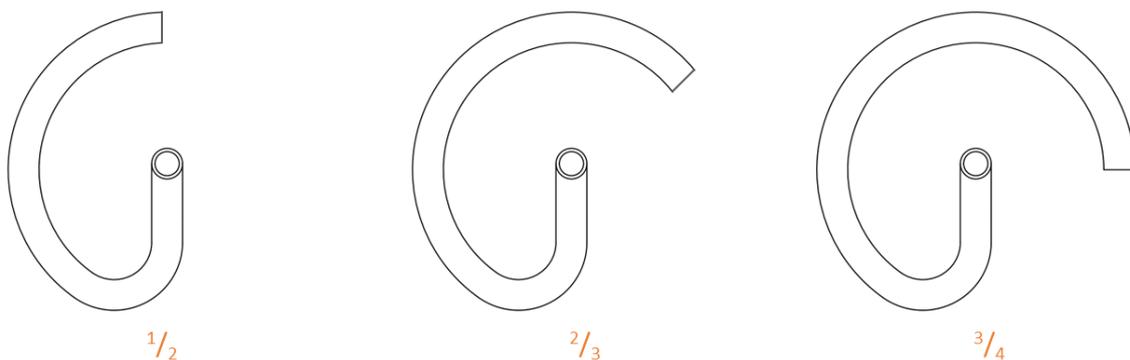
Figure 8.3: Three possible circle circumference configurations. The minimum corner radius is twice the tube radius. The fraction indicates how much of the $360°$ is spanned by the loop.

The friction during insertion can be lowered by ensuring that the upright of the device is not on the same level as the loop. This is shown in Figure 8.4. The angle between the loop and the upright of the

frame should be such that the height H_F is greater than 30 [mm], the average skin thickness [55]. For a 70 [mm] loop radius, the corresponding angle $\angle_F$ is approximately $20°$.
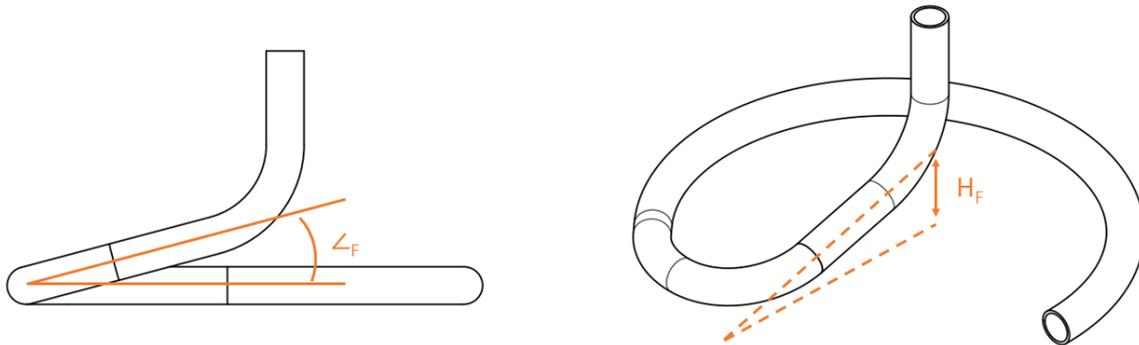
Figure 8.4: The angle and the distance between the horizontal of the loop and the upright of the frame.

Another possible design tweak to reduce insertion friction is to twist the loop. The recently published RAIS lifting device, which was designed in collaboration with Indian rural surgeons, uses this as shown in Figure 1.11c [38]. The currently used STAAN device has a downward twisted loop as well. These loops have a $5/6$ circumference, which would normally result in high insertion friction. However, twisting the loop negates the friction to a level acceptable for surgeons.

The publication did not list any injury rate numbers, which makes comparison difficult. Although a twisted loop remains a design option, it is not used for this lifting device because it is more difficult to produce than a flat loop. Furthermore, one of the main reasons for a twisted loop is that it gives easier access for a laparoscope to pass through underneath at the same incision, but this lifting device is designed to work without a laparoscope.

Finally, the tip of the loop is in the shape of a spade, which also helps insertion and prevents injury. The spade tip will be used for this lifting device.

Tube diameter

The final important parameter is the size of the tube. It can be characterised by its outer and inner diameter. For the chosen camera module, shown in Figure 7.4a, the inner diameter of the tube should be at least 10 [mm]. The camera sensor can then pass through the tube which is critical for assembly, as will be further explained in Chapter 10. The outer diameter of the tube should be as small as possible, with a maximum of 12 [mm] according to requirement D2.

The logical conclusion is to use a 12 [mm] metal tube with a wall thickness of 1 [mm]. It meets the two requirements of inner and outer diameter and it is standard-size tubing. This makes it easier and cheaper to acquire than if a custom dimension tube would be required. The tube is shown in Figure 8.5, together with the camera sensor. The dimension L_C indicates the length of the camera module's FFC, which is 163 [mm]. The camera sensor therefore needs to be placed within approximately 160 [mm] of the beginning of the tube.
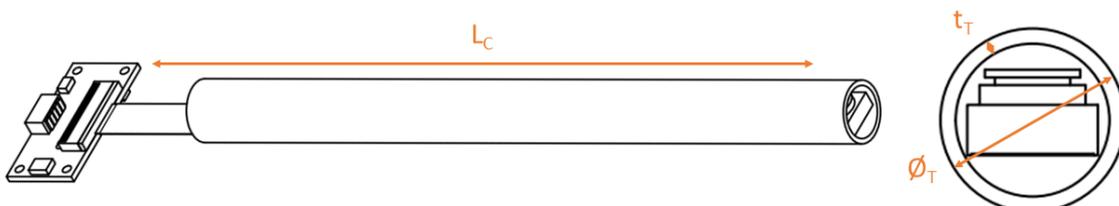
Figure 8.5: Dimensions of the tube that forms the basis of the lifting device, together with the camera module.

8.3. Other frame parameters

This section describes three additional dimension parameters of the lifting device: The position of the camera, the interaction of the lifting device with the mechanical retractor arm, and the position where the electronics will be stored.

Camera position

The camera will not be able to move with respect to the lifting device, because a fixed position is easier to manufacture, reduces complexity, and increases robustness. A fixed camera puts even more emphasis on having the correct position. The desired position of the camera relative to the frame of the lifting device can be described by three parameters, shown in Figure 8.6.

The first parameter is the height of the lifting device to the uterus, H_L. It is the sum of lifting height H_C, which was introduced earlier and ranges between 100 and 150 [mm], and the distance between the uterus and the abdominal skin near the umbilicus when the stomach is not lifted. This distance is minimal, and estimated to range between 30 [mm] and 80 [mm], the skin thickness plus 50 [mm] margin for larger waist circumferences. This estimate is based on average female waist circumferences [98]. Height H_L therefore ranges from 130 - 230 [mm], and the average 180 [mm] will be used for further calculations.

The second parameter D_U is the approximate horizontal distance between the umbilicus, the usual insertion point of the lifting device, and the location of the top of the uterus. It can be approximated based on research on fundal height development. The top of the uterus of a pregnant woman reaches the umbilicus around week 20, and the corresponding distance between the pubic bone and the umbilicus is 200 [mm] on average [99, 100]. In contrast, the top of the uterus of a non-pregnant woman extends 80 [mm] above the pubic bone on average. Hence, the average distance between the top of the uterus and the umbilicus D_U, for non-pregnant women, is approximately 120 [mm].

The third parameter $\angle_S$ is the preferred viewing angle of the surgeons. Expert GILLS surgeon J. Gnanaraj indicated that the preferred viewing angle is between $45°$ and $60°$.
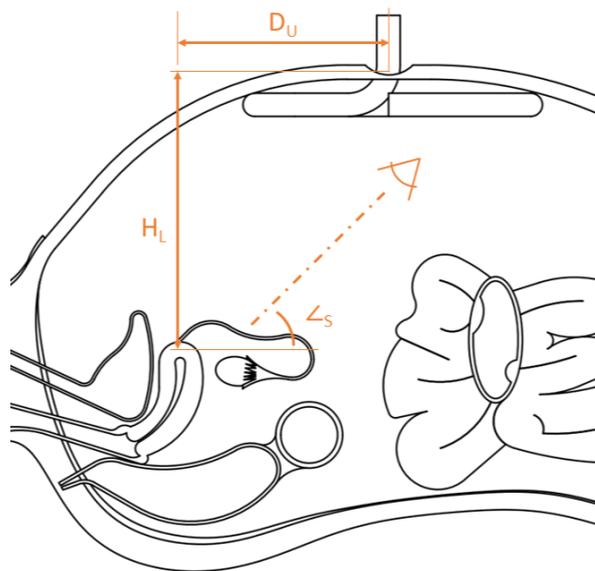
Figure 8.6: Section side view of the abdominopelvic cavity with working distances.

When the abdomen is lifted, a straight line from the umbilical insertion point towards the top of the uterus has an angle with the horizontal axis of approximately $55°$, because the vertical distance H_C is 180 [mm] and the horizontal distance D_U is 120 [mm]. A $55°$ angle is in the range of preferred viewing angles. The camera should therefore be positioned such that the viewing angle $\angle_S$ is $55°$ because it will look straight at the uterus.

However, the viewing angle is further complicated by the fact that surgeons tend to tilt the lift device in the direction of the surgery. This tilt angle is approximately $0°$ - $36°$ according to expert GILLS surgeon J. Gnanaraj. An average $15°$ tilt angle will be used. Hence, the camera needs to be tilted downward by $20°$, to get a combined angle of $35°$ with respect to the vertical axis, which is equal to a $55°$ angle with respect to the horizontal axis. This nicely matches the $20°$ angle $\angle_F$ and as a result, the camera sensor can be placed at this part of the lifting device. The lens can then be oriented perpendicular to the longitudinal axis, similar to Figure 8.5.

This camera position affects the positioning of the LED lights. The LED lights in the loop form an approximate ring, whereby the camera should be in the centre of that ring at the target. This means that the ring of LED light should be angled by $20°$ as well, such that it is parallel to the camera.

A final consideration about the camera position is the distance from the entry point. Figure 8.6 shows the lifting device inside of the abdomen with the entry point at the base of the upright. However, in reality, the abdominal skin is under tension and wraps tight around the lifting device, thereby receding along the frame. If the camera is too close to the entry point, it is obstructed by the abdominal skin.

Connector
The upright of the lifting device is shown in Figure 8.7 and is characterised by its length above the entry point H_U. This length provides clearance for insertion into the abdomen and for other instruments during the procedure. The RAIS lifting device uses a 65 [mm] upright, which will also be the required clearance of this lifting device. Consequently, any electronics that do not fit inside the tube, the camera's PCB for example, will be placed at least 65 [mm] above the entry point.

Furthermore, requirement M1 states that the lifting device should be compatible with the RAIS retractor arm. RAIS uses a custom hexagonal joint to connect the lifting device to the retractor arm, and that system will be used for this lifting device as well. The connection is shown in Figure 8.8. Due to its slanted edges, it can be set at specific forward or backwards angles around the lateral axis. The connector is a ten-sided hexagonal inscribed in an 18 [mm] cylinder that is 20 [mm] wide, connected to a 8 [mm] pole of approximately 20 [mm]. The pole should be located close to the centre point of the loop to aid its positioning by surgeons.
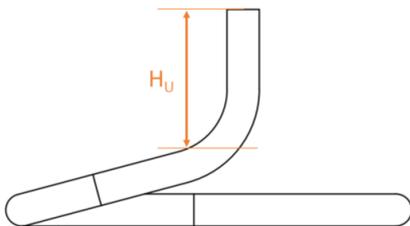
Figure 8.7: Height of the upright from the insertion point.

Figure 8.8: Render of the RAIS lifting device connection.

8.4. Final dimensions
This section summarizes the dimensional analysis. The calculated geometry of the lifting device is shown in Figure 8.9. It is based on nine calculated parameters and two assumptions. The nine parameters are listed in Table 8.1, together with their respective values and a short rationale. This geometry will be used as input for the following chapters 9 and 10.
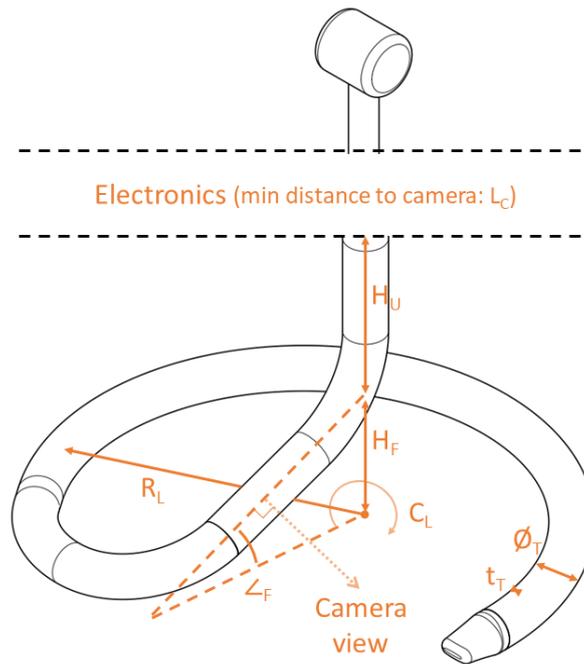
Figure 8.9: Drawing of the geometry of the lifting device.

The lifting device has a 70 [mm] radius loop with a $3/4$ circumference and a spade-like tip. It is made from a 12 [mm] tube with a 1 [mm] wall thickness. The section that connects the loop to the upright has an angle of $20°$ that creates a 30 [mm] gap at the centre, with the camera placed perpendicularly at this part of the tube. The upright of the lifting device is then at least 65 [mm] high before the larger, heat-generating electronic components can be placed. However, these need to be placed within 160 [mm] of the camera sensor due to the length of the FFC. Finally, the connection system from RAIS is placed centrally above the loop.

Table 8.1: The nine lifting device dimensions calculated in this chapter.

Parameter	Value	Rationale	Visual
R_L	70 [mm]	Minimum radius that ensures a sufficient operational volume.	Figure 8.1
C_L	$3/4$	Optimum between providing support and low injury rate.	Figure 8.3
$\angle_F$	$20°$	Minimum angle to create the required H_F.	Figure 8.4
H_F	30 [mm]	Equal to the average abdominal wall thickness.	Figure 8.4
L_C	160 [mm]	Maximum length of the camera's FFC.	Figure 8.5
$\varnothing_T$	12 [mm]	Maximum allowed insertion diameter.	Figure 8.5
t_T	1 [mm]	Maximum wall thickness that can still fit the camera inside.	Figure 8.5
$\angle_S$	$55°$	Viewing angle based on average female anatomical dimensions.	Figure 8.6
H_U	65 [mm]	Minimum required clearance height.	Figure 8.7

<div style="text-align: right; font-size: 4em;">9</div>

Structure & Materials

9.1. Applicable requirements

This chapter describes the structural design of the lifting device and the required materials. The structure of the lifting device has several functions. It provides support and stability, preventing deformation during use, and is responsible for distributing loads. It also ensures precise positioning of internal components and protects them from environmental factors and potential damage.

The functions for the structure are based on six requirements from Section 3.2, which are listed below with a brief rationale. Furthermore, an important prerequisite from multiple stakeholders in this project (not listed in the requirements) was to design the lifting device for local production. As a result, design choices about the structure, its materials, and production processes, were made in collaboration with biomedical engineers from India.

- **P1**   Abdominal wall lifting: The lifting device must sustain a load of 140 [N], distributed around the loop. Finite element analysis will be used to design the structure for strength. A safety factor of 2 is used based on an estimated medium reliability of material, medium environmental load, and considerable consequence of failure[1]. The structural strength will be verified in Chapter 13.
- **C1**   Low upfront purchase price: The complete device should be low-cost, and that applies to the structure as well. The cost of materials for the structure may not exceed 25% of the total cost, approximately €60.
- **C2**   Use of supplies: No supplies are permitted except water and electricity, hence the complete structure and all its materials should be reusable.
- **R1**   Dustproof and waterproof: The structure of the device should be dustproof and waterproof with respect to the electronics.
- **R2**   Cleaning and sterilisation: The lifting device is designed to be sterilised using Cidex or a Glutaraldehyde solution. Consequently, the materials on the outside of the device should be able to resist these cleaning agents.
- **D1**   Weight: The lifting device may weigh no more than 1 [kg].

9.2. Load-bearing frame

Throughout the history of loop-shaped AWL devices, solid metal rods have been used as the load-bearing frame, as shown in Figure 1.10 and Figure 1.11. These metal rods are bent or cast in the desired loop shape. The currently used STAAN ring is partly produced from a bent metal rod, joined to a square rod that serves as the connection to the retractor arm. The device comes in four variants, and the smallest variant is shown in Figure 9.1.

Indian biomedical engineers involved in the production of STAAN expressed the desire for this lifting device to also be manufactured using conventional production processes for metal, and plastics to be 3D-printed. This has several advantages, as will be discussed in Chapter 10. This design for manufacturing also drove the choice of frame.

---

[1]safetyculture.com/topics/factor-of-safety/

(a) Side view of the STAAN ring   **(b)** Front view of the STAAN ring   **(c)** STAAN device during a procedure
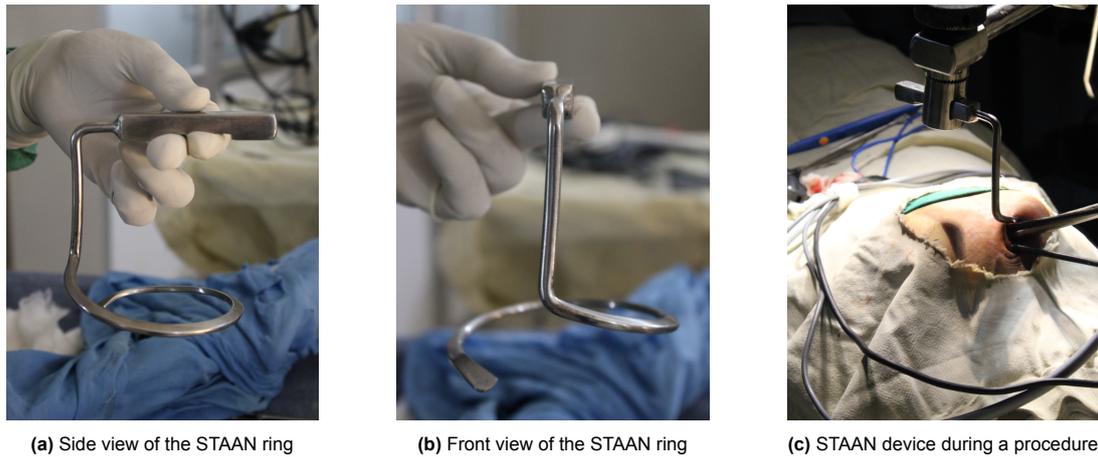
Figure 9.1: The currently used lifting device STAAN.

Interviews with Indian GILLS surgeons revealed a strong preference for the lifting device's loop to have a circular or slotted cross-section, as it minimizes the risk of injury and is easiest to insert through abdominal incisions. Combined with the need for easy production, this left two options for the load-bearing frame; A tubular metal frame or a metal-reinforced 3D printed frame.

The tubular metal frame was the clear favourite. The main advantages are that it consists of fewer parts, there is less risk of frame fracture, and it has a longer life expectancy. The required materials are easier to acquire, and it is easier to repair (as the metal-reinforced structure is an integrated part).

Tube structure

The metal tube will be the load-bearing frame that simultaneously shields the internal electronics. It requires holes for the camera and the LED lighting. Based on Chapter 8, a circular tube with an outer diameter of 12 [mm] and an inner diameter of 10 [mm] will be used (also referred to as 12x1 [mm] tubing). This tube structure has to carry a distributed load of 140 [N].

The starting point of the structure is a 12x1 [mm] metal tube with a length of approximately 500 [mm]. This is standard-size tubing for many types of metal. The metal tube will be bent, a process explained in Section 10.2, in the shape of a loop as calculated in Section 8.4. The finite element analysis (FEA) tool from Fusion 360 *(Autodesk Inc., California)* was used to calculate the strength of the frame.

Verification of FEA tool

First, a simple verification of the FEA tool was performed. For a 12x1 [mm] tube with a length of 400 [mm] and distributed loads 100, 150, and 200 [N], the analytical solution was compared to the FEA result. Beam theory states that for a beam that is rigidly clamped on one side and free on the other, under a distributed load q, the maximum deflection $\delta_{y_{max}}$ is given by Equation 9.1 and the maximum absolute stress $|\sigma|$ by Equation 9.2 [101].

$$\delta_{y_{max}} = -\frac{qL^4}{8EI_x} \quad \text{at} \quad x = L \qquad (9.1) \qquad\qquad |\sigma| = \frac{|q|L^2u}{2I_x} \quad \text{at} \quad z = 0 \qquad (9.2)$$

The FEA was performed on a straight, 400 [mm] long tube and a circularly bent tube, with a bend radius of 85 [mm] and length of 400 [mm]. Surgical stainless steel 440C was used as the study material. The mesh size was the default from Fusion 360. The results are shown in Figure 9.2.

The FEA tool from Fusion 360 underestimates the strength of the tube by approximately 25% when compared to the analytical solution, which can be seen by comparing the Analytical (Straight) and the FEM (Straight) lines. The difference could be caused by mesh and solver imperfections but is on the safe side, i.e. the FEA tool overestimates the stresses.

An interesting effect occurs when the 400 [mm] tube is bent, see the FEM (Circular) lines. It becomes stronger by a factor of 2. Due to the circular shape, part of the bending load is converted to torsion. Tubes are excellent at handling torsion, and thus the overall strength of the structure increases.

To conclude, the FEA tool gives realistic values and can therefore be used for a first estimation of structural strength. However, it has to be validated by an actual load test.
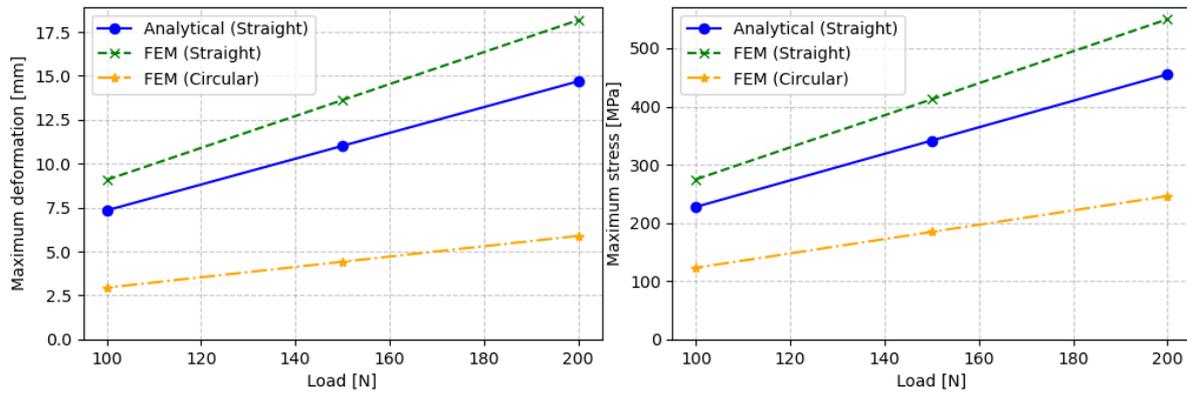
Figure 9.2: Comparison of analytical and FEA results for straight and bent cylindrical tubes.

Frame strength simulations

The strength of the tubular load-bearing frame was simulated for dozens of different configurations using FEA. The final configuration was determined by the dimensions from Chapter 8 and production requirements from Chapter 10 and is shown in Figure 10.2. The Von Mises yield criterion was used as the mode of failure. The plain structure, a bent tube without any modifications, is sufficiently strong for a distributed load of 140 [N], with a safety factor of approximately 4.4. However, the addition of holes, needed for both the camera and the LED lighting, required careful consideration.

The holes are shown in the three renders in Figure 9.3. The first opening is required for the insertion of electronics into the frame, near the site where the housing will be placed. It is a slot with a width of 9 [mm] and height of 16 [mm], required for safe insertion of the camera module.

The second set of openings, shown in Figure 9.3b, are two circular holes that are necessary for the camera module. The largest of the two has a diameter of 7.5 [mm] and is used for the camera sensor. The second hole has a diameter of 6 [mm] and is necessary for the assembly of the current version of the prototype. It also doubles as an extra opening for LED light.

The structure with the three holes as shown in Figure 9.3a and Figure 9.3b is still sufficiently strong. However, a third set of holes is required for the LED lighting system as shown in Figure 9.3c. The size and spacing of these holes determine the strength of the frame.

(a) Hole required for the electronics   **(b)** Two holes required for the camera   **(c)** Additional holes for the LED lighting

Figure 9.3: The three sites where holes in the structure are required.

Expert GILLS surgeon J. Gnanaraj noted two important considerations for the distribution of the holes for the LED lighting. Firstly, they need to be evenly spread around the large-radius portion of the loop, approximately 250 [mm] in length, to get an even distribution of light. Secondly, the holes in line

with the camera module need to have a $20°$ forward orientation, like the camera, such that the light runs parallel to the camera. Holes to the side of the camera face directly downward.

To determine the optimal distribution and size of the circular holes, two series of FEA tests were performed, plotted in Figure 9.4. Optimal in this case is the largest total surface area of the holes, for which the safety factor of the frame is still 2. The total surface area of the holes equals the number of holes times the surface area per hole, half the diameter squared times π.

In the first series of tests, shown in red, the number of holes was varied for a set diameter of 5 [mm]. In the second series of tests, shown in blue, the diameter of the holes was varied for a set number of 25 holes. A polynomial surface was fitted to this data. The two dashed black lines are isolines from this surface at a safety factor equal to 2.

The optimal distribution for the LED lighting system was found to be 24 holes with a diameter of 5.5 [mm], spaced at approximately 10 [mm]. It yields the largest total surface area at 570 [mm^2].
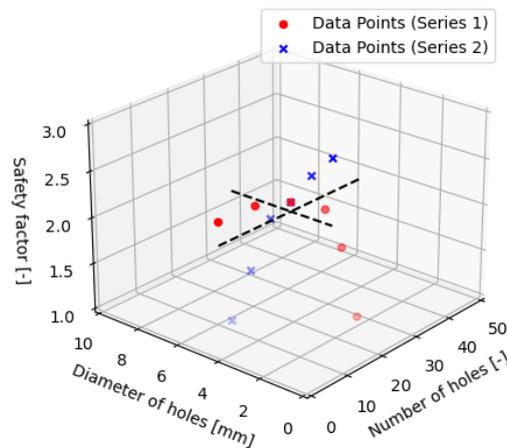
Figure 9.4: 3D plot of the FEA results for LED hole distribution. The dashed black lines are isolines for a safety factor of 2.

The final FEA result for the tube structure is shown in Figure 9.5. The structure is under a distributed load of 140 [N]. The study material is surgical stainless steel 440C. The mesh size is the default from Fusion 360. The calculated maximum stress is 340 [MPa], resulting in a safety factor of 2 and a maximum deformation of 2.5 [mm]. The approximate weight of the structure is 200 [g].

(a) Safety factor results, viewed from below

(b) Displacement results, viewed from above
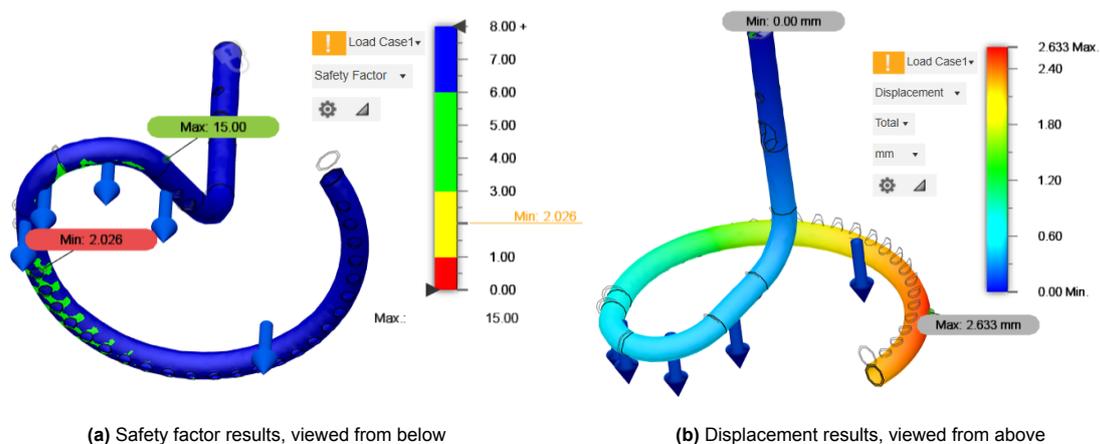
Figure 9.5: Finite element analysis results for the tube structure.

Connector

The lifting device should be compatible with the RAIS retractor arm and thus requires its custom hexagonal connector. This connector consists of two parts, a $20x8$ [mm] pole joined to an 18 [mm], ten-sided hexagonal, as described in Section 8.3. It will be placed in line with the frame. This construction is easy to produce and ensures the load is in line with the frame, which benefits the structural rigidity.

The resulting structure is shown in Figure 9.6. The two parts of the connector are produced from metal rods, the same type of material as the tube. The pole will be produced from a 10 [mm] rod. It will be inserted into the frame for 20 [mm], taper to 8 [mm], and extend another 35 [mm]. The connector will be produced from an 18 [mm] rod. The hexagonal will be carved out such that two opposite sides are 17 [mm] apart. The connector is 20 [mm] wide and has an 8 [mm] hole at the bottom.

(a) Connector pole, $20x10$ [mm] to $35x8$ [mm]   **(b)** Connector joint, 18 [mm] ten-sided hexagonal

Figure 9.6: Connector pole and joint used for this lifting device.

9.3. Additional parts

The load-carrying frame acts as a support for all additional parts. The complete structure is shown in Figure 9.7, viewed from below. The camera module is placed using a small 3D-printed holder, and the LED strip is stuck to the frame at its edges using adhesive tape. The other parts that can be seen are the housing for the electronics, the tube endcap, and the camera window.

(a) Complete structure viewed from below   **(b)** Same view, without the tube structure and half the housing
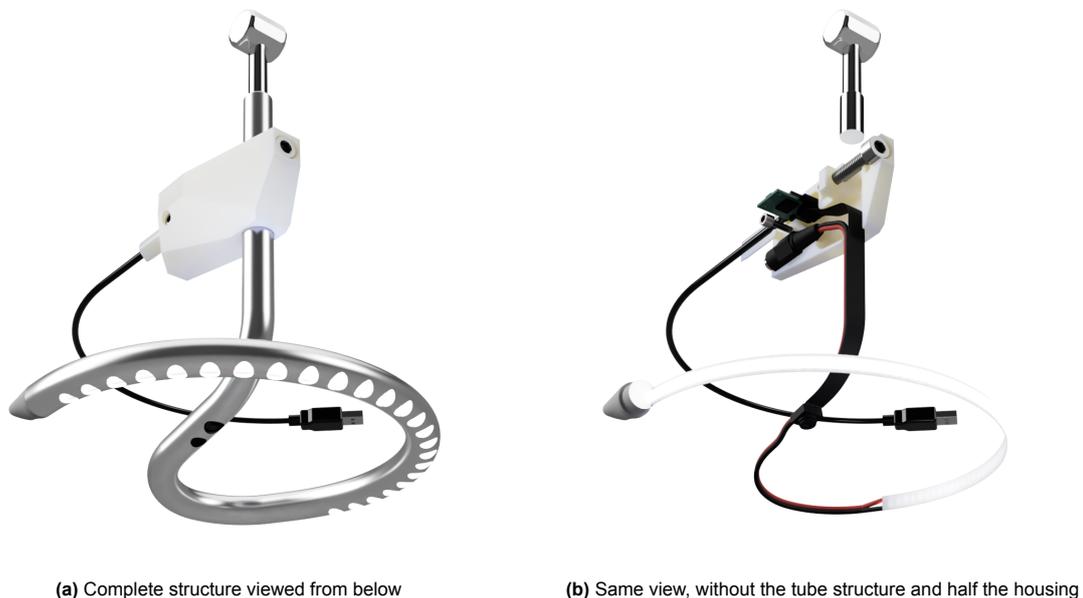
Figure 9.7: Renders of the complete structure of the lifting device.

Housing

The housing holds the camera module's PCB and the LED strip's 12V power plug, as described in Section 7.4. It is a minimalistic design based on the required internal volumes for the PCB and the power plug, as well as any excess cable. The CAD drawing of the housing is shown in Figure 9.8.
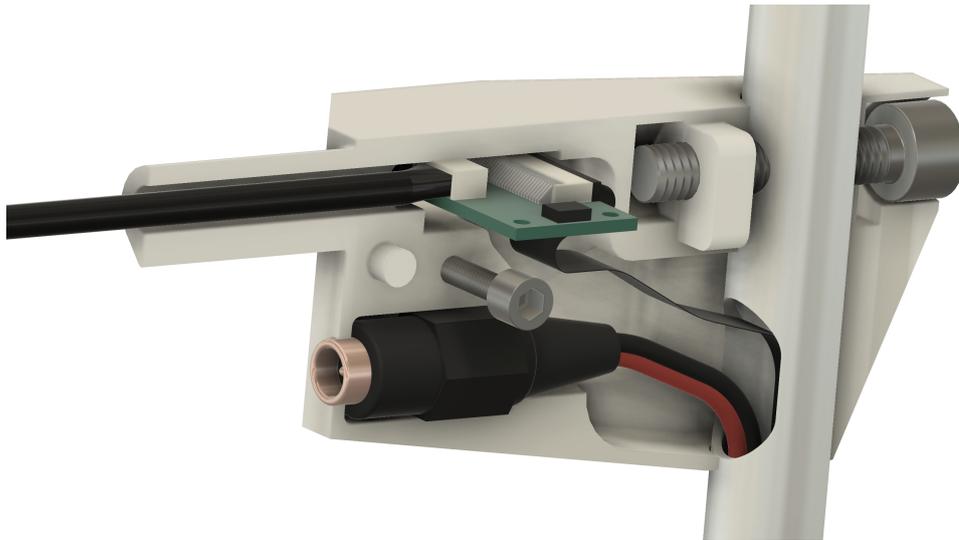
Figure 9.8: Detailed CAD drawing of the housing's right side with all the electronic components.

The housing will be 3D-printed from plastic to keep costs and weight low. The topside in Figure 9.8 serves as the bottom side during printing. Expert GILLS surgeon J. Gnanaraj indicated that many surgeons use the housing to position the lifting device, and in the process put a lot of force on the housing. The reinforcement is a 35 [mm] M6 bolt that acts as the spine of the housing and connects to the tubular load-bearing frame.

The housing consists of two near-identical sides, which are also held together by an additional 25 [mm] M3 bolt at its front. The housing measures 97 [mm] in length, 33 [mm] in width, and 38 [mm] in height. The outside borders are protected using sealant, such that the housing is waterproof. The inside shape of the housing fits exactly to the electronics, such that no additional anchoring is required. The housing is elongated around the camera module's USB cable which has no protection around the first 25 [mm], contrary to the render in Figure 9.8. The total weight of the housing is estimated at 50 [g].

Tube endcap

This lifting device requires a spade-like tip, or endcap, as described in Section 8.4. The endcap of the prototype is a 3D-printed part in the required shape, which is screwed onto the open end of the tube using a small M2 screw. However, for the lifting device, a metal tip is preferred. It can be produced as a part, like the 3D-printed part, or by compressing the ends of the tube together. For this version of the lifting device, a separate part is necessary, despite its obvious disadvantages, because an open tube end is needed for assembly.

Hole covers

The holes in the frame need to be covered such that the device is waterproof and the electronics are protected. The housing itself protects the holes near the housing, but the holes for the camera sensor and LED lighting require other solutions. An outside protection was favoured over an internal filling of clear resin because it is easier to disassemble.

Flexible, transparent heat shrink was used for this lifting device. The heat shrink is available in 1 [m] tubes with a diameter of 12.7 [mm], a wall thickness of 0.5 [mm], and a shrink ratio of 2:1. This option is easy to assemble and low cost, compared to individual covers for all 25 holes. Furthermore, it is not susceptible to small manufacturing defects in the holes. The effect of the heat shrink on light intensity will be measured in Chapter 12.

However, the camera module can not be covered by the heat shrink, because it is not transparent enough and distorts the image. Clear thermoform plastic was tried in two variants. In the shape of the tubular frame as shown in Figure 9.9a, and in the same shape but with a flat section for the camera sensor as shown in Figure 9.9b, created using the small 3D-printed press shown in the same picture. This gives clearer but still distorted images.

(a) Thermoformed cover & heat shrink   (b) Thermoformed cover with flat section   (c) Modular lens that can be cut to size
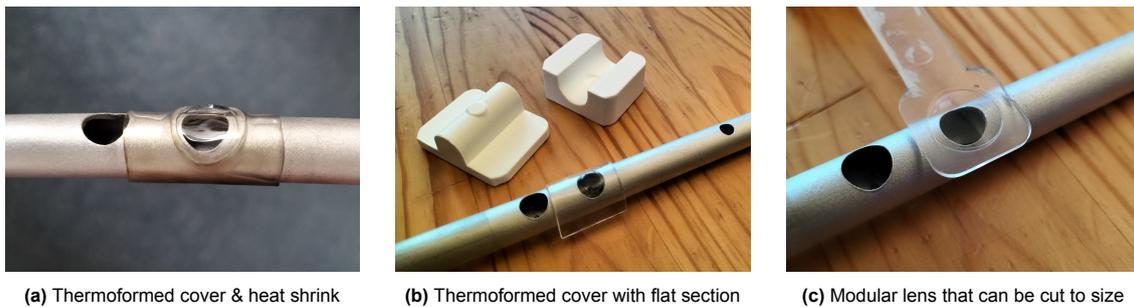
Figure 9.9: Three examples of camera sensor covers. Option 3 gives the least distortion.

Therefore, the camera sensor has to be protected by a flat lens, which will be placed onto the sensor. Such a lens is shown in Figure 9.9. Note that it causes no distortions of the underlying tube. The flat lens will partly sink into the tubular structure and be glued into place. The heat shrink will be assembled after the lens, with a small hole around the camera sensor's lens. The heat shrink will be applied to the whole tubular frame from the endcap to the housing (which is waterproof itself) such that the whole structure is waterproof.

9.4. Materials

The lifting device's structure as described in the previous Section 9.2 and Section 9.3 still uses generic terms for the materials used, such as "metal" and "plastic". This section specifies all materials.

Metal

The first choice of material is the type of metal for the tubular load-bearing frame and the connector. No materials other than metals were considered to adhere to local production standards.

The metal used for the load-bearing frame has to adhere to several requirements. Its yield strength should be equal to or greater than that of surgical stainless steel 440C (690 MPa) because that was used as study material for the FEA calculations and ensures a safety factor of 2. Secondly, although the frame is completely protected by heat shrink ideally, the metal should be corrosion and chemical-resistant because it has to endure many procedures and chemical cleaning cycles. Finally, the metal should be bendable such that it can be produced in the right shape.

Six types of metal were considered for the tubular load-bearing frame, based on market research. Most types of metal are commercially available as 12x1 [mm] standard-size tubing. Their properties are summarised in Table 9.1, where SS is short for stainless steel. The values for cost per kilogram are rough estimates only to indicate the order of magnitude of material costs.

316L stainless steel is a corrosion-resistant austenitic steel with good formability. It is widely used in medical applications due to its biocompatibility and resistance to various environments [102]. Its yield strength in the solution-annealed condition is too low to be used for this lifting device, but it can be increased by cold-working the metal.

440C stainless steel is a high-carbon martensitic stainless steel known for its exceptional hardness and wear resistance [103]. Though less common in medical applications, its robust properties make it suitable for this lifting device.

17-4 PH is precipitation-hardened stainless steel offering a unique combination of high strength and corrosion resistance [104]. In the annealed condition, 17-4 PH has good machinability (similar to 304 stainless steel) but after hardening heat treatment, bending and machining are difficult.

Aluminum Alloy 7068 is known for its exceptional strength-to-weight ratio and toughness [105]. Classified as an ultra-high-strength aluminium alloy, it is developed based on aluminium 7075. It has excellent corrosion resistance. The alloy has to undergo a heat treatment process for strength.

Ti-6Al-4V is a versatile titanium alloy renowned for its high strength-to-weight ratio, biocompatibility, and corrosion resistance [106]. Widely used in aerospace and medical implants, it's suitable for applications demanding lightweight and durable materials.

Cobalt-chromium-molybdenum alloys, like CoCrMo, are renowned for their strength, corrosion resistance, and biocompatibility [107]. They are commonly used in orthopaedic implants.

Table 9.1: The six types of metal considered for the tubular load-bearing frame. 17-4 PH SS is the best option.

Material	Yield [Mpa]	Density [kg/m^3]	Cost [kg^{-1}]	Corrosion Resistance	Bendability
316L SS	200 - 800	7990	€2 - €5	Good in various environments	Good, suitable for bending
440C SS	690	7700	€5 - €15	Good corrosion resistance	Challenging due to high hardness
17-4 PH SS	**600 - 1200**	**7800**	**€5 - €10**	**Good corrosion resistance**	**Dependent on heat treatment**
7068 Al alloy	500 - 680	2780	€10 - €20	Good corrosion resistance	Excellent, highly bendable
Ti-6Al-4V alloy	830	4430	€20 - €40	Excellent, biocompatible	Moderate, some bend processes not possible
CoCrMo alloy	600	8400	€30 - €50	Excellent, used in medical implants	Challenging, may require specialized equipment

Stainless steel is the metal of choice for the tubular load-bearing frame, with 17-4PH and 316L being the best options. They meet the minimum yield strength requirement (depending on the type of heat treatment). Furthermore, they are cheap, have good corrosion resistance, and can be bent using traditional bending processes in their solution-annealed condition [108]. They can then be precipitation-hardened at different temperatures to develop a wide range of mechanical properties.

Stainless steel 316L is commercially widely available, whereas $12x1$ [mm] tubes of 17-4PH stainless steel are more difficult to acquire. However, stainless steel 316L has to be cold-worked to at least $1/2$-hard to develop sufficient strength. Stainless steel 17-4PH is used for this design but further research into metal selection is recommended.

Good second options are stainless steel 440C and aluminium 7068. Stainless steel 440C can achieve high levels of hardness through heat treatment and is commonly used for the production of knives and precision bearings. However, this hardness also makes it more difficult to bend. Furthermore, stainless steel 440C is the most magnetic metal in the list, which could cause potential interference issues with the electronics. In contrast, aluminium alloy 7068 is non-magnetic and with a heat treatment, its yield strength can be increased up to almost 700 [MPa]. Aluminium is also very easy to work with.

The third option, titanium alloy Ti-6Al-4V, is an order of magnitude more expensive than stainless steel. It is difficult to bend using traditional bending processes because it is more brittle than stainless steel and experiences work-hardening, making it prone to cracking.

At the production facilities of the Delft University of Technology, stainless steel is not available. Hence, for the production of the prototype, aluminium 6060-T66 is used. This type of aluminium was readily available in the correct sizes. It is known for its ease of manufacturing and it can be annealed, making it more ductile and therefore easier to bend [109]. With a yield strength of around 170 [MPa] and a density of 2700 [kg/m^3], the tubular frame from aluminium is approximately a factor of 4 less strong and lighter than a frame from 17-4 PH Stainless Steel.

Further research is needed into the interaction between the two bolts in the design and the material of the frame. For example, when normal carbon steel bolts are screwed into a stainless steel frame, galvanic corrosion can occur. This happens because stainless steel and carbon steel have different electrochemical properties, leading to the flow of electrical current between them when they come into contact with an electrolyte, such as moisture or humidity, thereby accelerating the corrosion of the bolts.

Plastics

The structure has several plastic parts, the largest of which is the housing for the electronics. This is quite an intricate part that will be only produced in low volumes, and as such 3D printing is the logical choice of production. Indian biomedical engineers indicated that they have a filament 3D printer at their disposal, and access to common filaments such as polylactic acid (PLA), acrylonitrile butadiene styrene (ABS), polyethene terephthalate glycol (PETG), nylon, and thermoplastic polyurethane (TPU). The best filament will be selected based on its mechanical strength, chemical resistance, heat resistance, abrasion resistance, and costs.

PLA lacks mechanical strength and is very stiff. ABS offers good strength and impact resistance. PETG strikes a balance between mechanical strength and flexibility, making it versatile. Nylon, with its high tensile strength, is ideal for durable parts. TPU provides a high degree of elasticity. [110]

PLA has limited resistance to cleaning chemicals, while ABS and PETG exhibit moderate chemical resistance. Nylon and TPU generally withstand chemicals well. [111]

PLA and TPU have the lowest heat resistance around $60°$-$70°$ [C]. PETG has a slightly higher softening temperature of $75°$-$80°$ [C], and ABS has a range of $90°$-$95°$ [C] [112]. Nylon boasts a relatively high heat resistance at approximately $150°$ [C].

PLA and ABS offer limited abrasion resistance. PETG exhibits significantly better resistance. However, nylon and TPU are the best, both renowned for excellent abrasion resistance relative to other filament materials [113].

The cost of every filament is the same order of magnitude, with the cheapest being €20 [kg^{-1}] and the most expensive around €60 [kg^{-1}]. PLA and ABS are generally the cheapest, making them suitable for the prototyping phase. PETG falls into a mid-range in terms of cost. Nylon, with its superior mechanical characteristics, tends to be pricier. TPU is more expensive than all other (rigid) filaments because of its flexibility.

Based on these five properties, nylon filament is most suited to be used to print the housing. Its flexibility is overcome by the shape of the housing. It has the best resistance to cleaning chemicals and heat from electronic components. However, it is also more difficult to print because it requires a higher temperature and is abrasive, meaning the nozzle wears out quickly. It needs to be stored in a dry and cool place.

If available, a good alternative to nylon filament could be acrylonitrile-styrene-acrylate (ASA). This filament has been specially developed to be more UV-resistant. ASA is strong, stiff and relatively easy to print. The material is also extremely resistant to chemical influences and heat.

For the production of the prototype, PLA was used as it is the only filament material available at the production facilities of the Delft University of Technology.

The endcap of the prototype and the small camera sensor holder were both 3D-printed on a stereolithography (SLA) printer. SLA printers can print in a much higher resolution than filament printers and can use biocompatible materials. SLA printers are also orders of magnitude more expensive than filament printers and are not available at the production facilities in India. However, for the lifting device, these two parts should both be produced from the same type of metal as the load-bearing frame. Therefore, SLA printers are not required for the production of the lifting device.

Sealing

The holes in the structure, except the one for the camera, are covered by applying flexible, transparent heat shrink to the load-bearing frame. The camera sensor is covered with a plastic lens to ensure the image is not blurred or distorted.

For heat shrink, the industry-standard thermoplastic material polyolefin is used[2]. It is commercially available in a wide range of dimensions, and for this lifting device tubes with a diameter of 12.7 [mm] and a wall thickness of 0.5 [mm] are used.

One of the primary characteristics of polyolefin heat shrink is its transparency, which allows for easy visibility of underlying components and light to pass through. The material is flexible and designed to shrink when exposed to moderate heat ($70°$-$100°$ [C]) with a maximum ratio of 2:1. It is thus suitable

---

[2]https://www.polyfluor.nl/en/products/heat-shrink-tubing/polyolefin-heat-shrink-tubing/

for wrapping around the intricate shape of the lifting device, and creates a tight and waterproof seal. It also provides a layer of protection against abrasion and physical damage.

Polyolefin heat shrink tubing typically exhibits good thermal stability because it has a recovery temperature (the temperature at which the tubing begins to shrink again) higher than the initial shrink temperature. It can also withstand temperatures well below its shrinking temperature. Its safe range is approximately $-40°$ to $100°$ [C]. Furthermore, polyolefin has good resistance to a variety of chemicals, oils, and solvents [114]. It also serves as an excellent electrical insulator.

Further research is needed into the protection of the camera sensor using a lens. The lens should not distort the image and be resistant to heat, cleaning chemicals, impacts, and scratches. Common materials for such small lenses are acrylic (also known as polymethyl methacrylate) and polycarbonate. Polycarbonate is more expensive but also has better thermal and impact resistance.

The prototype has a flat lens made from Vivak®Copolyester. This material can be thermoformed, but that will introduce distortions. Hence the lens is simply a laser-cut, flat circle of Vivak®Copolyester that is put on top of the camera sensor.

Bill of materials

This section gives a brief overview of the structure and materials used for this lifting device. An exploded view of the main components of the lifting device is shown in Figure 9.10. The structure fulfils all requirements as it can sustain a load of 140 [N] with a safety factor of 2, uses no supplies, is dustproof and waterproof, withstands cleaning chemicals, weighs approximately 380 [g], and costs approximately €60 in raw materials.
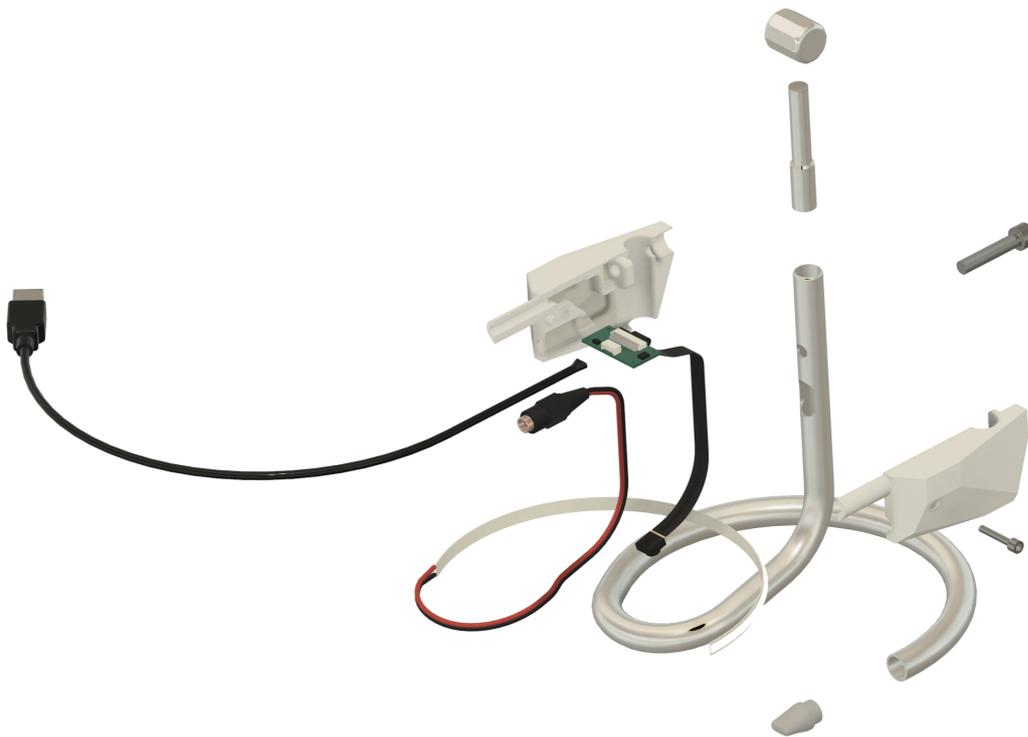
Figure 9.10: Exploded view render of the structure.

The load-bearing frame is a 12x1 [mm] tube made from 17-4 PH stainless steel or aluminium 6060-T66 for the prototype. The RAIS-inspired connector is made from two 18 [mm] and 10 [mm] rods of the same metal. The endcap should also be made of the same metal, but the prototype's endcap is SLA printed using draft resin from Formlabs. The structure is protected using transparent polyolefin heat shrink, with a small window for the camera sensor's protective lens.

The two-part housing is 3D printed from nylon filament. Due to material restrictions, the housing of the prototype is 3D printed from PLA filament. The housing is constructed using two steel bolts. The 35 [mm] M6 bolt acts as reinforcement for the housing and the 25 [mm] M3 bolt ensures a tight fitting of the two sides. The housing is made waterproof using sealant.

The electronics are all off-the-shelf components. The PCB of the camera module connects to a USB cable, and the 12V plug of the LED strip can also be connected to a 12V-to-5V USB adapter. They are secured to the load-bearing frame using small 3D-printed holders and shape-fit.

10

Production & Assembly

10.1. Applicable requirements

The production and assembly of the lifting device was one of the main focus points of the project. The experience of Indian rural surgeons is that newly designed medical devices often prove impossible to produce and implement in local low-resource settings. As mentioned in Chapter 9, an important prerequisite from multiple stakeholders in this project was to design the lifting device for local production. As a result, design choices about the production process were made in collaboration with biomedical engineers from India.

The philosophy of the production and assembly of the lifting device was to keep it simple and cost-effective, using tried and tested techniques. That will be faster, easier, and cheaper, compared to novel production techniques, as tooling and expertise is already present. The applicable requirements from Section 3.2 are listed below with a short rationale.

- **C1** Low upfront purchase price: The complete device should be low-cost. Production can be a significant cost factor if expensive tooling is required. The cost of custom tooling is added to the budget and may not exceed 25% of the total cost, approximately €60 per device.
- **R1** Dustproof and waterproof: The structure of the device should be dustproof and waterproof with respect to the electronics. These electronics should also be protected during assembly.
- **M1** Intuitiveness: This requirement also applies to production and assembly. The process used for the lifting device should fit the local production capabilities and have a clear step-by-step workflow such that it can be repeated.

10.2. Production techniques

The production of the lifting device uses 4 traditional machining techniques. Bending, drilling, turning, and milling. Bending is the main machining technique. It is used to create the shape of the load-bearing frame from a single piece of tube. Furthermore, 3D printing is used for the plastic parts.

Bending

Tube bending is a versatile and efficient machining technique where metal tubes can be formed into various configurations without compromising their structural integrity. The use of this machining technique is different from the currently used STAAN lifting device, which is produced using a combination of casting and welding. These processes and others, such as milling, hydroforming, and metal 3D printing, were all considered but bending was found to be best suited for this type of structure.

One of the key advantages of tube bending lies in its ability to preserve the structural integrity of the material [115]. Welding for example introduces potential weak points at joints. Furthermore, tube bending provides unparalleled design flexibility, allowing for the creation of the loop shape. Tube bending also contributes to products with a better surface finish. [116]

In comparison to the other machining techniques, tube bending is the cheapest option. It requires fewer materials and fewer labour hours than the machining techniques used for the STAAN lifting device. Tube bending also offers a significant advantage in terms of tooling costs with respect to milling, hydroforming, or metal 3D printing.

There are three main tube bending techniques. Compression bending, rotary draw bending (which can be expanded to mandrel tube bending), and roll bending. They are shown in Figure 10.1. Roll bending is not used for the production of the frame because thin-walled tubing easily collapses for smaller bend radii, and the accuracy and repeatability are poor. For compression bending, the die (shown in blue) is stationary, while in rotary draw bending the die rotates [117]. When a mandrel is added to the tube during rotary draw bending, it is called mandrel tube bending.

(a) Compression bending   **(b)** Rotary draw bending   **(c)** Roll bending
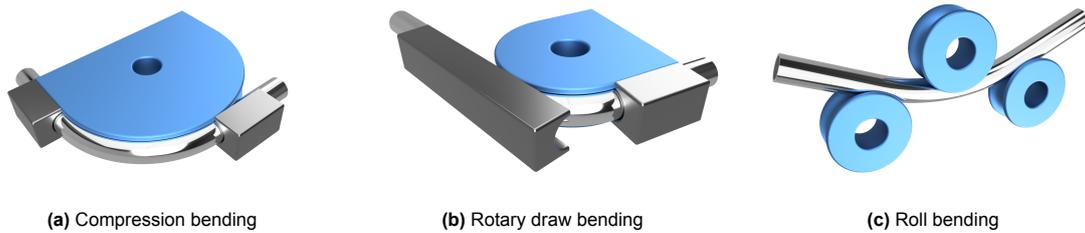
Figure 10.1: Illustration of the three main bending techniques. The dies are blue and the clamps are grey.

For both compression bending and rotary draw bending, process design is difficult and experience-based [118]. The industry-standard minimum bend radius is 2.5 times the tube diameter. Smaller radii bends are prone to imperfections such as flattening, kinking or even collapse. Additional measures can be taken to produce even tighter bends, but those will not be considered for this project to keep production simple. In addition to the minimum bend radius, every bend should have a straight section of at least 30 [mm] at one end. This straight section is necessary to clamp the tube during bending and prevent slip, which results in kinking at the inner radius of the bend. These two production requirements, combined with the dimensions from Chapter 8, set the final configuration of the load-bearing frame as shown in Figure 10.2.
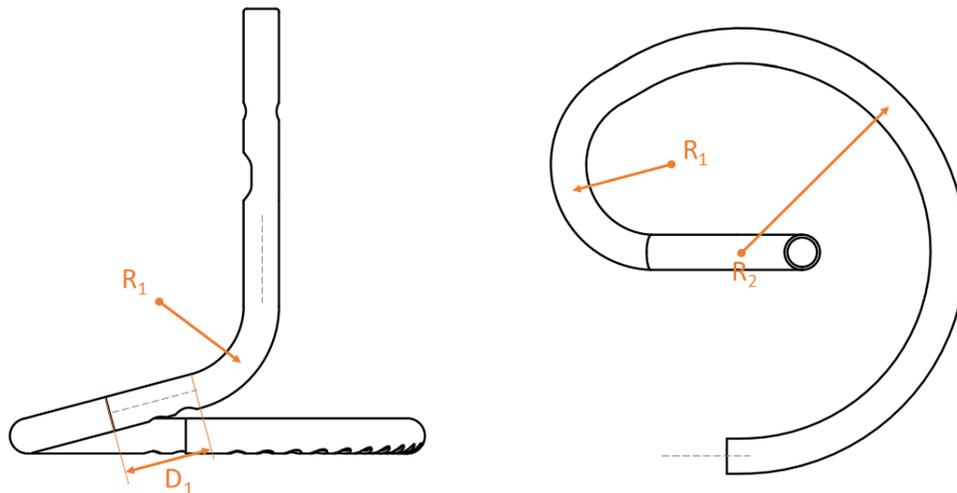
Figure 10.2: Side view and top view of the load-bearing tubular frame. It consists of two small radius bends, denoted by R_1, and one large radius bend, denoted by R_2. Every bend has at least one straight side of length D_1 to clamp the tube during bending.

The minimum bend radius for a 12x1 [mm] tube is 30 [mm]. The tubular frame has two bends with this minimum bend radius, denoted by R_1 in Figure 10.2. The bend shown in the side view has a bend angle of $75°$ and the other small radius bend has an angle of $150°$. The tubular frame has one larger

bend with a radius R_2 of 70 [mm] and a bend angle of $210°$. Every bend has a straight section on one side of length D_1, 30 [mm], indicated by the grey dashed lines.

### Compression bending

Compression bending is a cost-effective and fast bending technique. It was used for the production of the aluminium prototype. The tube is bent around a stationary bend die using pressure from a wiper die. The tube is placed at the start of the bend die and a wiper die is forced against the outer radius of the tube. This pressure causes the tube to deform and take the shape of the bend die. The degree of bend is determined by the angle through which the wiper die is rotated. Most manual tube bending tools use compression bending as their working principle. However, the small radii bends of the structure are more difficult to produce with this technique and it is less precise than rotary draw bending.

The two 2.5 diameter radii bends in the load-bearing frame require high bending forces. To achieve such levels of force by hand, a force multiplier is required. Another option is to anneal the tube such that is temporarily more malleable and therefore easier to bend. An additional problem is that a small radius bend is prone to imperfections such as flattening or wrinkling of the tube. Filling the tube with a filler helps to distribute the pressure during bending and ensures the tube retains its shape throughout the bend. The filler can be a mandrel, sand, or frozen water. The effect of filler material is clearly shown in Figure 10.3, where an annealed aluminium 6060 12x1 [mm] tube was bent with and without filler material. The used filler material was fine quartz sand.

(a) Test frame created without filler, shows severe flattening.

(b) Test frame created with filler, shows almost no flattening.
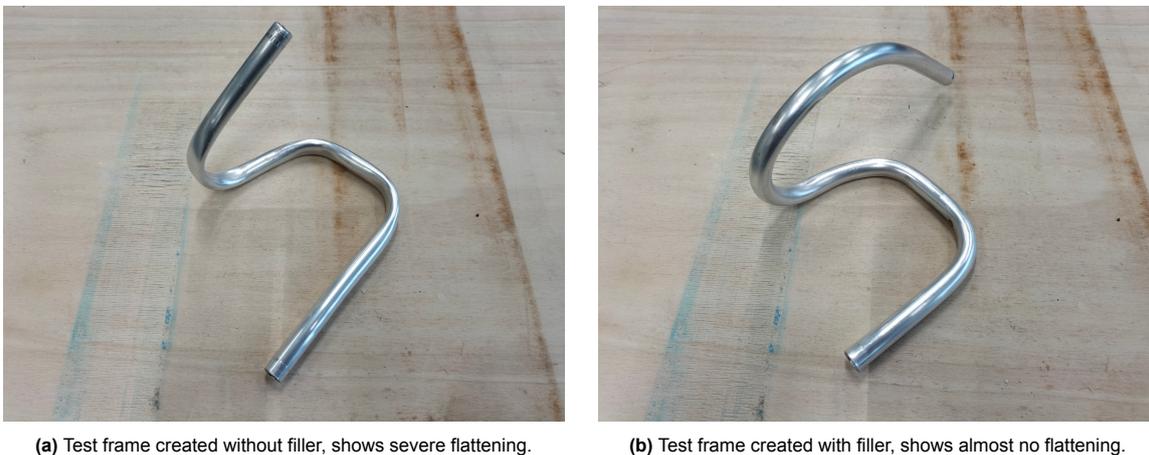
Figure 10.3: The effect of filler material (quartz sand) on the quality of compression bends.

Secondly, springback is most pronounced in compression bending. Springback means that the tube exhibits elastic recovery upon release of the applied force, leading to dimensional deviations from the intended final form. This phenomenon is difficult to model numerically. As a rule of thumb, the bend radius of the die should be 3% smaller than the intended radius of the tube and the wiper die should rotate an extra $1°$-$2°$ for aluminium and $2°$-$3°$ for stainless steel.

No expensive tooling is required for compression bending. For softer materials, such as the annealed aluminium used for the prototype, a bend die from wood or plastic suffices. For the prototype, bending dies from 4 layers of laser-cut 3 [mm] wood were created. Such bend dies are cheap and can be produced to the exact bend radii that are required. The tubes can be filled with fine sand as a filler and small 3D-prints as plugs.

The third and final iteration of the wooden bend dies is shown in Figure 10.4. It is a workstation that combines two bend dies on a single board. The left of the workstation can be used to create the two bends with a radius of 30 [mm] and the right can be used for the large radius bend of 70 [mm]. It is created from a single 5 [mm] bottom plate and four top plates with a thickness of 3 [mm], connected by screws. The top plates have a vertical profile that fits with 12 [mm] tubing. Several holes in the top plates ensure precise positioning with respect to the bottom plate. This workstation can be used to produce dozens of aluminium frames and costs approximately €10.
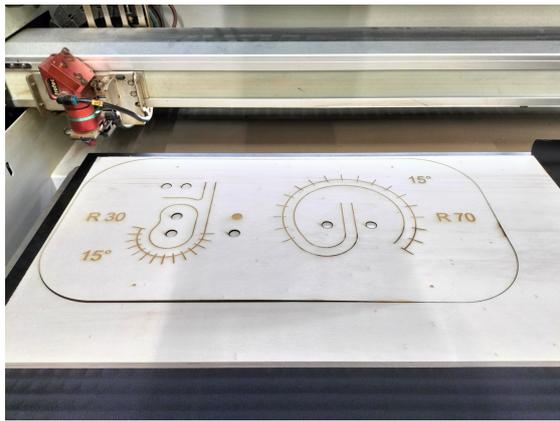
(a) The bottom plate is laser-cut from 5 [mm] wood
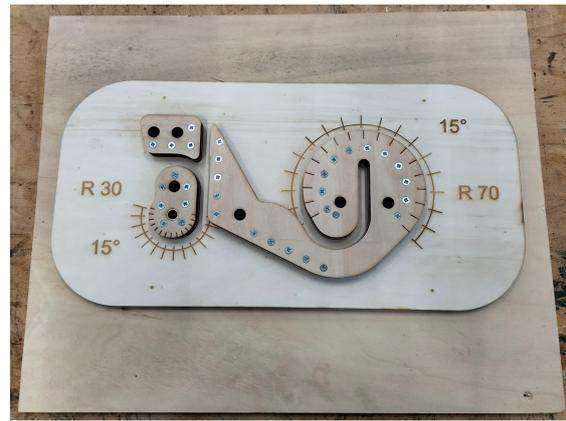
(b) The assembled workstation with two bend dies

Figure 10.4: The production of the compression bending workstation from wood using a laser cutter.

Rotary draw bending

The second bending technique is rotary draw bending, where the tube is bent around a rotating die. It is the working principle of most tube-bending machines. The tube is clamped to the bend die using a clamp die. The bend die rotates and simultaneously draws the tube. The pressure die ensures the tube stays in place. The radius of the bend is determined by the radius of the bend die, and the bend angle is determined by the angle through which the bend die is rotated. Rotary draw bending machines can achieve higher forces than manual compression bending. Therefore, the use of a rotary draw bending machine is the advised bending technique for the production of the tubular load-bearing frame from 17-4 PH (or 316L) stainless steel.

It is important to note that the required bending force can be reduced by heating the stainless steel tube to a temperature above its recrystallization temperature before bending. This is so-called hot bending. However, hot-bending stainless steel introduces the risk of sensitization, reducing corrosion resistance. For this reason, cold bending should be used to produce the stainless steel frame. It also allows for more precise control over the bending process than hot bending. Stainless steel 316L would necessitate cold bending to harden.

Rotary draw bending requires that a tube bending machine is available, and custom dies for the production of the frame. Two tube bending machines of the same type, CBC UNI 42, are available at the Delft University of Technology. These machines are numerically controlled and can be set to rotate a specified angle, with increments of $0.5°$. The machine, which was used to perform initial production tests, is shown in Figure 10.5a. The bronze-coloured block is the pressure die, the small metal ring serves as the clamp die, and the bend die is black.

(a) CBC UNI 42 tube bending machine
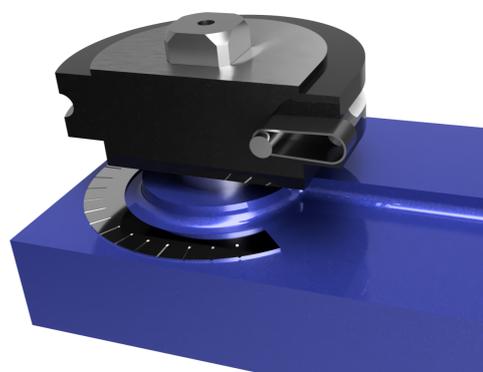
(b) CAD drawing of a custom 70 [mm] bend die

Figure 10.5: The tube bending machine and custom tooling required for the stainless steel frame.

To bend a tube with such a tube bending machine requires 3 custom dies. The clamp die and the pressure die should both match the diameter of the tube, i.e. 12 [mm], and the bend die should match the tube diameter and the bend radius. A 12 [mm] clamp die and a 12 [mm] pressure die are included with the machine because 12 [mm] is standard-size tubing. However, the 12 [mm] bend die from the machine has a radius of 36 [mm] which does not fit the bends required for the load-bearing frame.

As a result, two custom bend dies are required with bend radii 30 [mm] and 70 [mm] respectively. These dies should not be made from regular steel to prevent galvanic corrosion. Machining experts from the Delft University of Technology estimated that milling these dies from aluminium would cost approximately €400 per die. An impression of the custom 70 [mm] die is shown in Figure 10.5b.

Drilling

The second machining technique is drilling. All 30 holes in the tubular frame are created using drilling. The location and orientation of these holes are important for the performance of the lifting device, and hence the drilling involves a systematic process.

The first step is to select the appropriate drill bit, often high-speed steel or cobalt, with a diameter based on the desired hole size. The 24 holes for the LED lighting are 5.5 [mm], the two holes for the camera module are 6 and 7.5 [mm] respectively, the two holes for the M6 bolt are 6 [mm], and the opening for the electronics consists of two adjacent 9 [mm] holes.

The second step is securing the frame to provide stability during drilling and the right orientation for all the holes. This is especially important for the LED lighting holes, which should be evenly distributed and have a different orientation based on their relative position to the camera. As described in Section 9.2, holes in line with the camera module require a $20°$ forward orientation and holes to the side of the camera face directly downward, as shown in Figure 10.6a. A custom 3D-printed jig, shown in Figure 10.6b, marks the location of every hole and provides stability for the drill bit, together with centre punch markings. The holes for the camera are also drilled using a custom 3D-printed jig.

(a) LED hole location relative to centre line

(b) 3D-printed drilling jig
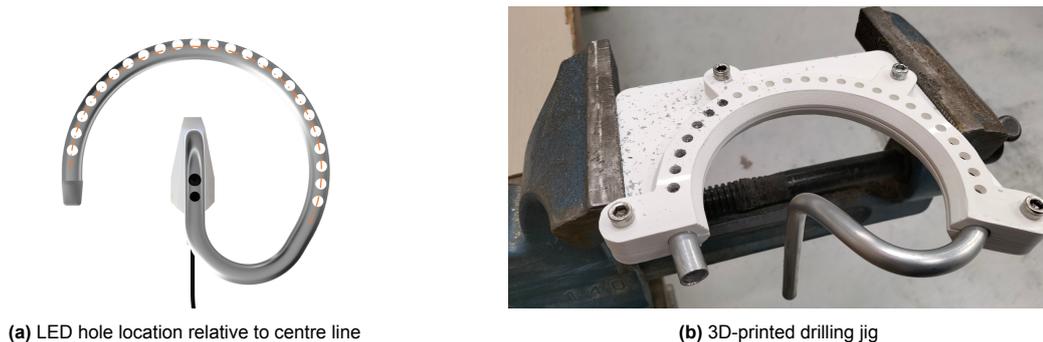
Figure 10.6: Custom 3D-printed drilling jig to ensure the holes are drilled at the intended location.

The process so far is the same for aluminium and stainless steel frames. However, the two different materials require different drill speeds. Soft metals like aluminium 6060 are drilled with high drilling speeds, about 2500 [rpm], whereas hard stainless steel is drilled at approximately 1000 [rpm] for 5.5 [mm] holes. Applying cutting fluid, though optional for softer metals, aids in dissipating heat during drilling. A depth stop is used to prevent over-penetration.

The final step is to deburr the holes. Specialized hand tools are used to remove any burrs or sharp edges around the completed hole. A small cutting plier is used to create a slot from the two adjacent 9 [mm] holes. After bending and drilling, the tubular load-bearing frame is finished.

Turning & Milling

The next step in machining the lifting device is the RAIS connector and the endcap. This step requires the use of a turning machine (also known as a lathe) and a milling machine. Although these machines are expensive, they are common in most machining facilities and the Indian biomedical engineers also have access to such machines.

The connector consists of two parts, shown in Figure 10.7. The components are glued together in the prototype, but welding is preferred for the lifting device.

A-A (1:1)

A-A (1:1)

(a) Dimensions of the pole

(b) Dimensions of the joint
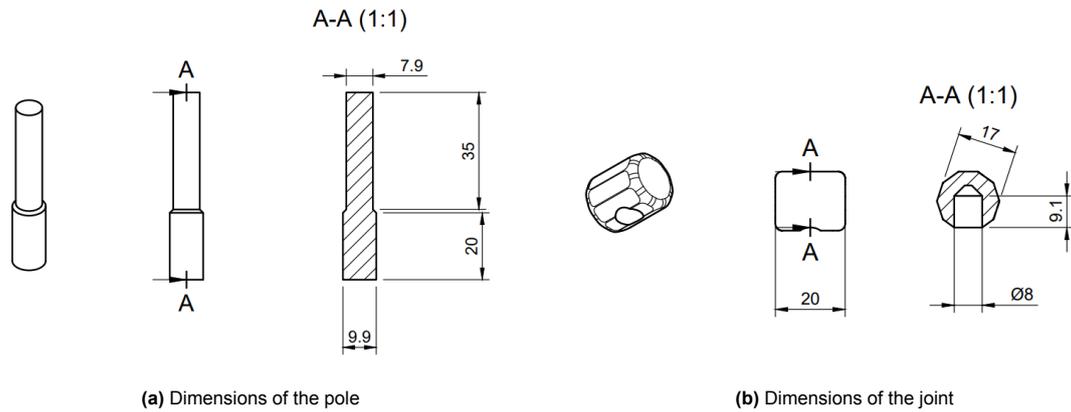
Figure 10.7: Technical drawings with dimensions of the two parts of the RAIS connector.

The pole is created from a 10 [mm] diameter rod with a length of 55 [mm]. Using a conventional lathe, the diameter of the first 35 [mm] is reduced to 7.9 [mm]. The diameter of the remaining 20 [mm] is reduced to 9.9 [mm]. These dimensions allow for a snug fit of the pole at both ends, the tubular frame and the connector joint.

The connector joined is created from 18 [mm] diameter rod with a length of 40 [mm]. Using a conventional milling machine, a ten-sided hexagonal is formed. The rod is rotated every $36°$ and the milling machine chips away 0.5 [mm] such that two opposite sides of the connector joint are 17 [mm] apart. This workpiece is transferred to the lathe, where the edges are rounded and the connector is cut to a width of 20 [mm].

The endcap is created from a 12 [mm] diameter rod with a length of at least 20 [mm]. Using a lathe, the diameter of the first 5 [mm] is reduced to 8 [mm]. The spade-like tip is shaped using a milling machine and finished by hand sanding. The technical drawing of the endcap is shown in Figure 10.8.

B-B (1:1)

A-A (1:1)
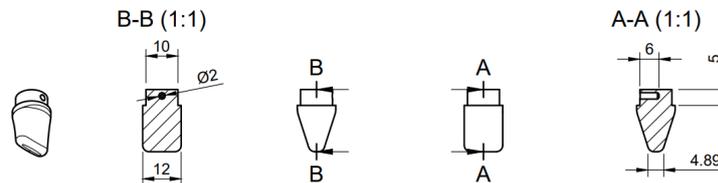
Figure 10.8: Technical drawing with dimensions of the endcap.

3D printing

The final part to be produced is the housing, shown in Figure 9.8. The two sides are separately printed using a filament 3D printer. The top side of the housing serves as the bottom side during printing. The supports can have the minimal z-distance of a single layer height if the zig-zag pattern is used. The single-layer z-distance gives an accurate result at the inside of the housing. Apart from removing the supports, no post-processing is required. The prototype's housing was coated with chrome but this is not required for the lifting device.

With these machining processes, all custom parts required for the lifting device can be produced. The next step is assembly of the custom parts and all the off-the-shelf components.

10.3. Assembly

This section provides a sequenced workflow of the assembly of the lifting device. It includes the required materials and every machining process to give a comprehensive overview. The approximate time for every step is listed. This process was also used for the production of the aluminium prototype.

The total time to produce the custom tooling is 24 hours. This step has to be performed only once for the production of multiple lifting devices. A single lifting device takes approximately 3 days. However,

this includes multiple rest periods in which no work is being performed. Hence multiple lifting devices could be produced in parallel, whereby the production time per unit can be reduced to 8 hours.

The workflow for the production and assembly of the living device consists of 15 steps, listed below.

1. The start of the production and assembly process is the machining of custom tooling. For the lifting device, two two-piece custom jigs need to be 3D-printed that assist with drilling the holes for the LED lighting and camera sensor. For bending the frame, two custom aluminium bend dies need to be milled. For the prototype, these aluminium dies are replaced by a wooden workstation with two compression bend dies as shown in Figure 10.4. The tooling can be reused.

   Required materials: PLA filament for the jigs. 50 [mm] aluminium plate for the custom dies, or multiple 3 [mm] wooden plates for the workstation.

   Estimated time: The total print time for the two jigs is 18 hours. The custom aluminium dies take 5 hours per die. Laser cutting and assembling the workstation takes 2 hours.

2. The first step is preparation for the production of the load-bearing frame, using a 12x1 [mm] tube of 17-4 PH stainless steel cut to a length of approximately 600 [mm]. The aim is to cold bend this tube. However, this has not been tested and if cracking occurs hot bending may be necessary. The aluminium 6060 tube for the prototype is also annealed before bending using a flame gun.

   Required materials: 12x1 tube, cut to 600 [mm] in length, made from 17-4 PH stainless steel or aluminium 6060-T66 for the prototype.

   Estimated time: 15 minutes for heating the tube, and 2 hours for cooldown afterwards.

3. The (annealed) tube is further prepared by filling it with fine quartz sand. Two plugs are 3D-printed from PLA. One end of the tube is plugged, the tube is filled, and the second plug is hammered in. When the two plugs are secured in place, one end of the tube is bent on the small radius die to further pressurise the inside.

   Required materials: Approximately 300 cc quartz sand and two 3D-printed plugs.

   Estimated time: 15 minutes.

4. The tube is now ready to be bent, which has to happen in a specific order. The first bend is the 75°, 30 [mm] radius bend that is connected to the upright. For the lifting device, the second bend is the 210°, 70 [mm] radius bend that forms the loop, followed by the final 150°, 30 [mm] radius bend. For the prototype, the last two bends are reversed. The 20° elevation is bent by hand.

   Required materials: 12x1 tube with length 600 [mm].

   Estimated time: 30 minutes.

5. The bent frame is left to harden again for 24 hours. Meanwhile, the connector can be produced. The first part is the pole, produced on a lathe from a 10 [mm] diameter rod. The diameter of the first 35 [mm] is reduced to 7.9 [mm], the diameter of the remaining 20 [mm] is reduced to 9.9 [mm].

   Required materials: Metal rod, of the same material as the frame, with a 10 [mm] diameter and a length of 55 [mm].

   Estimated time: 30 minutes.

6. The second part of the connector is its joint, created mainly on a milling machine from an 18 [mm] diameter rod. To form the hexagonal, the rod is rotated every 36° and the milling machine chips away 0.5 [mm] from the edge. The joint is finished on the lathe. The two parts of the connector can be joined together using welding or glueing.

   Required materials: Metal rod, of the same material as the frame, with a 18 [mm] diameter and a length of 40 [mm]. Also required are weld materials or glue.

   Estimated time: 2 hours, for joint production and to connect it to the pole.

7. Assuming that the tubular frame has hardened, all 30 holes can be drilled, using the custom jigs from step 1. The 24 holes for the LED lighting are 5.5 [mm], the two holes for the camera module are 6 and 7.5 [mm] respectively, the two holes for the M6 bolt are 6 [mm], the opening for the electronics consists of two adjacent 9 [mm] holes, and the hole to secure the endcap is 2 [mm] in diameter. After drilling, every hole should be deburred by hand. The frame is sanded with fine-grit sandpaper to remove imperfections caused by the production process.

Required materials: The bent tubular frame from step 4, and the 3D printed drilling jigs.

Estimated time: 2 hours to drill and deburr all holes. Sanding takes 30 minutes.

8. The long ends of the frame can be cut to length, and the connector can be joined to the tubular frame. For the lifting device welding is preferred, but for the prototype two-part epoxy adhesive is used. The joined structure needs to rest for several hours.

   Required materials: Welding materials or two-part epoxy adhesive.

   Estimated time: 3 hours, mainly to rest the device.

9. The final part to be machined from metal is the endcap. Machining starts on the lathe, after which the spade-like tip is shaped on the milling machine. The insert is cut to length and a 2 [mm] diameter hole is drilled at 2 [mm] from the tube's open-end edge. The endcap is finished by hand sanding it. For the prototype, the endcap was SLA 3D-printed which took less than 1 hour.

   Required materials: Metal rod, of the same material as the frame, with a 12 [mm] diameter and a length of 30 [mm].

   Estimated time: 1 hour.

10. The housing is 3D-printed using a filament printer. Each side of the housing takes 2 hours to print and requires 15 [g] of Nylon filament. The printing process can be left unattended. Post-processing involves removing the supports and sanding away any zits and blobs on the inside.

    Required materials: Approximately 15 [g] of Nylon filament, or PLA for the prototype.

    Estimated time: 4 hours for the printing in total. The post-processing steps take 30 minutes.

11. All components are machined in the first ten steps and the electronics can now be positioned. First, the camera's sensor head is inserted into the load-bearing frame and advanced to the dedicated opening in the structure by feeding the FFC. The sensor head is secured in place using a holder. Secondly, a thin metal wire is guided through the entire tube until it comes out at the open tube end. The wire is then connected to the LED strip and can be used to pull the LED strip into position. The strip can be secured using adhesive.

    Required materials: All electronics (camera module, LED lighting system, USB cable) and a 1 [mm] diameter metal wire.

    Estimated time: 15 minutes.

12. The first half of the housing is screwed onto the load-bearing frame using the M6 bolt. The electronic components that go inside the housing (PCBs and power connections) are anchored by shape-fit. Sealant is applied around the borders.

    Required materials: Left side of the housing, 35 [mm] M6 bolt, and waterproof sealant.

    Estimated time: 5 minutes.

13. The housing is completed with the right side fitted and screwed in place by the M6 bolt and an additional M3 bolt. The insertion sites for the bolts should be protected by sealant as well.

    Required materials: Left side of the housing and a 25 [mm] M3 bolt.

    Estimated time: 5 minutes.

14. The LED strip can be disconnected from the metal guidewire and is folded inwards into the frame. The endcap can now be placed and secured using an M2 bolt.

    Required materials: Endcap and a 5 [mm] M2 bolt.

    Estimated time: 5 minutes.

15. The final assembly step is to make the rest of the lifting device waterproof. A small plastic lens will be stuck to the sensor head. The tubular frame can then be sealed using transparent heat shrink at approximately $90°$ [C].

    Required materials: 6 [mm] clear plastic lens, and 500 [mm] of 12.7 [mm] heat shrink tubing.

    Estimated time: 30 minutes.

When these 15 steps are completed, the lifting device is completely assembled. The production and assembly process of the prototype is illustrated in Section 11.2. However, the lifting device based on this process can not directly be used in clinical practice because every individual device needs to be tested. Important functions such as image quality, light intensity, and waterproofness need to be verified before use. These tests will be described in Chapter 12 and Chapter 13.

<div align="right">

11

</div>

Prototypes

11.1. Prototype 1: PLA

The concept of integrating an imaging system with the lifting device for GILLS surgery had not been explored prior to this thesis. Hence, a study into the feasibility of this technology was required. This first prototype served that purpose. It is a tangible proof of concept, created from 3D-printed PLA parts such that improvements could easily be produced and added to the prototype.

Overview

The 3D-printed prototype presented in this section is the fourth generation of development, guided by five inputs: two electronic components and three outer dimensions. The electronics are the OmniVision camera module, shown in Figure 7.4a, and a 5V LED strip with dimmer, shown in Figure 7.7a. The input dimensions are a loop with a radius of 65 [mm], a diameter of 15 [mm], and a viewing angle of $0°$ (straight down). The aim was to create a lookalike lifting device with an integrated imaging system. The first, second, and fourth development iterations are shown in Figure 11.1.

(a) Bottom side view of the first iteration   **(b)** Top side view of the second iteration   **(c)** Top side view of the fourth iteration
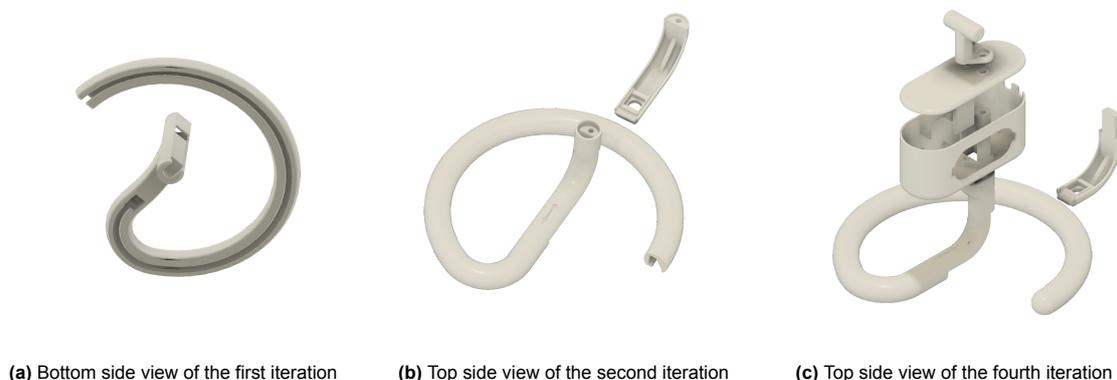
Figure 11.1: CAD renders of three iterations of prototype development.

Production

The final iteration of this prototype consists of six separate 3D-printed parts, which house both electronic components. The total print time of all parts is approximately 12 hours. It is assembled using four M3 screws. The electronics are placed during assembly and locked into place by shape-fit. The assembled prototype is shown in Figure 11.2b.

    Five parts of the prototype are shown in Figure 11.2a. The sixth part, a transparent strip to close the loop, is not shown in either picture. The loop itself is created from two parts, a large frame and a small latch. The large frame has a slot in which the LED strip can be fitted. The small latch has a square section that fits the camera sensor.

(a) 3D-printed components of the prototype   **(b)** Bottom side view of the assembled prototype

Figure 11.2: Overview of the fourth-generation 3D-printed prototype.

On top of the loop sits the electronics housing, with space for the camera module's PCB and the LED strip's dimmer. The housing is closed by a lid, and on top of that is a connector. At the underside of the loop, a transparent print closes the open slot. The screws in the bottom of the electronics housing connect to the two parts of the loop. The top lid and connector are secured by two screws into a bridge in the electronics housing.

Findings

This prototype is fully functional, as shown in Figure 11.3, and could therefore be used for an intermediate evaluation of the concept. The evaluation of this prototype was done in collaboration with Professor P.R. Culmer, responsible for the design of RAIS [38]. The prototype proved that the concept had enough promise to continue development. The camera module paired with the ring of LED light provided excellent imaging. However, several important issues arose that needed to be addressed in the next stage of prototyping.
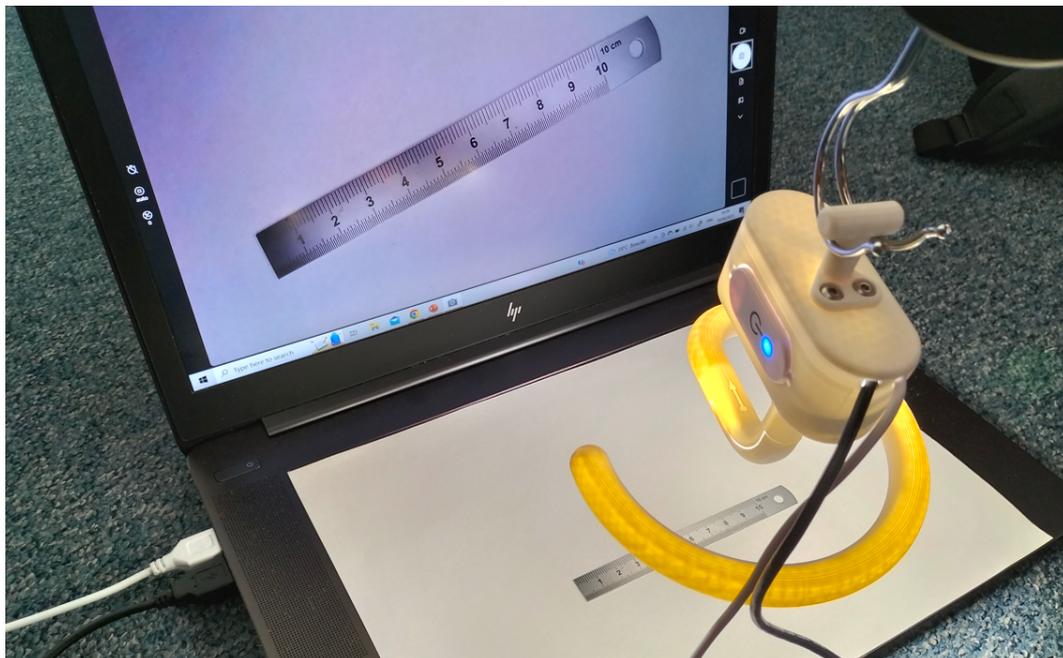
Figure 11.3: The 3D-printed prototype imaging a 100 [mm] ruler from a distance of 100 [mm].

The main issue was the low structural strength of the prototype. Though not a surprise, the big question mark at this stage of the project was if this concept could be developed such that it also had the required structural strength. The PLA material was too weak and the latch system, used to enclose the camera sensor, further weakened the structure. The focus of further prototypes should therefore be on structural strength, using metals. The loop cross-section diameter, which for this prototype is 15 [mm], should be reduced to 12 [mm].

Important lessons were also learnt about the packaging of the electronics. The camera sensor head, which measures 8.5 x 8.5 x 5.8 [mm], is too large to put longitudinal inside a tube with an inner diameter of 12 [mm]. Consequently, the sensor head should be placed perpendicular to the longitudinal axis with a maximum deviation of $\pm15°$. The camera should be clamped in place to avoid vibrations.

The LED strip can only bend laterally. That makes it impossible to put the strip in the loop with the LEDs facing downward, but instead facing to the side. An LED strip with a beam angle of $180°$ is thus required. Furthermore, a feedthrough system is required to position the LED strip.

The dimmer on the LED strip did not function properly. The intended function is to switch on/off on a single touch and to dim for prolonged touch. However, the sensitivity of the dimmer was poor, responding to touch only 50% of the time approximately. Its performance was even worse when touched with a wet medical glove. It was therefore decided to not use this dimmer for further prototypes.

11.2. Prototype 2: Aluminium

This section describes the second phase of prototyping, resulting in an aluminium prototype. When reference is made to "the prototype" in other chapters, this aluminium prototype is meant. Three aluminium prototypes were produced to the same specification for several tests.

Overview

This aluminium prototype is the fifth generation of development. Its design and production are based on the previous chapters, and it closely resembles the final design of the lifting device. However, the load-bearing frame is made from aluminium 6060-T66 (instead of stainless steel) due to availability, and the endcap is 3D-printed instead of machined. Not every prototype is finished to be completely waterproof as these final steps are harder to reverse. All the main components are shown in Figure 11.4a, and the assembled prototype is shown in Figure 11.4b.

(a) Components of a single prototype   **(b)** Two fully-assembled prototypes

Figure 11.4: Overview of the fifth-generation aluminium prototype.

Production

The aluminium prototype is produced and assembled using the workflow described in Section 10.3. The first steps of this workflow concern the tubular frame. Starting with a straight 600 [mm] 12x1 [mm] tube, it is annealed, filled with sand, bent to the right shape, left to harden, and drilled to produce all the required holes. These steps 2,3,4, and 7 respectively are shown in Figure 11.5.
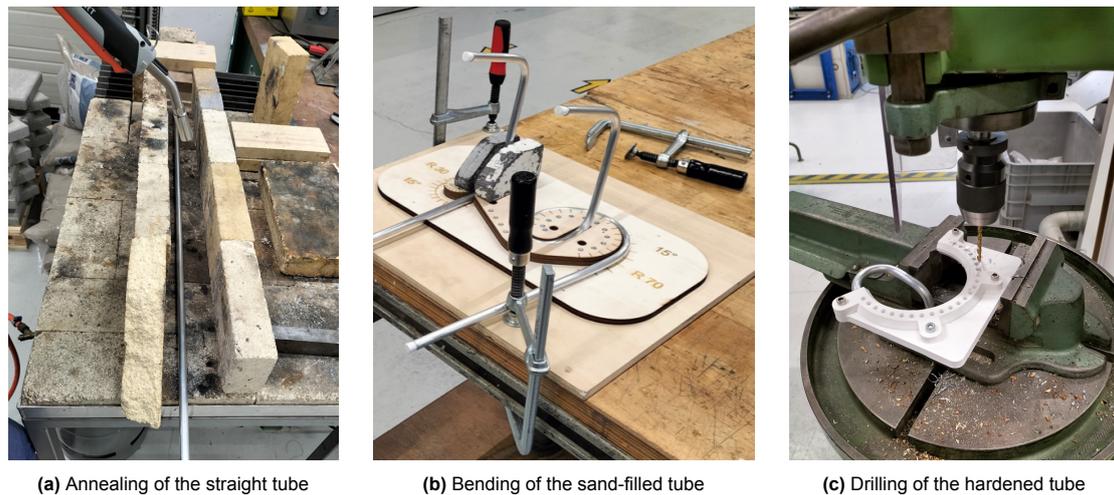
(a) Annealing of the straight tube   **(b)** Bending of the sand-filled tube   **(c)** Drilling of the hardened tube

Figure 11.5: Machining of the tubular load-bearing frame.

The connector is produced in parallel with the frame, corresponding to steps 5 and 6 of the workflow. The pole is produced on a lathe and the joint on a milling machine, shown in Figure 11.6a. The frame, shown in Figure 11.6b, is deburred, sanded with fine-grit sandpaper, and polished. The two parts of the connector are joined together by a two-part epoxy adhesive from Griffon®, shown in Figure 11.6b. The connector itself is then joined to the tubular frame, using the same two-part epoxy. The endcap is 3D-printed on an SLA printer.

(a) Milling of the connector joint   **(b)** Sanded & polished frame   **(c)** Joining the connector with adhesive

Figure 11.6: Machining of the connector and polishing of the frame.

The electronics housing of this prototype is 3D-printed from PLA and spray-coated with chrome, as shown in Figure 11.7a. The LED strip used for the prototype required some modifications. The sides of the strip were trimmed such that it would fit inside the tube more easily, and a 12 [V] female power plug was soldered on. The connection is protected by a 30 [mm] piece of black heat shrink. The LED strip, shown in Figure 11.7b, is unit-tested directly afterwards.
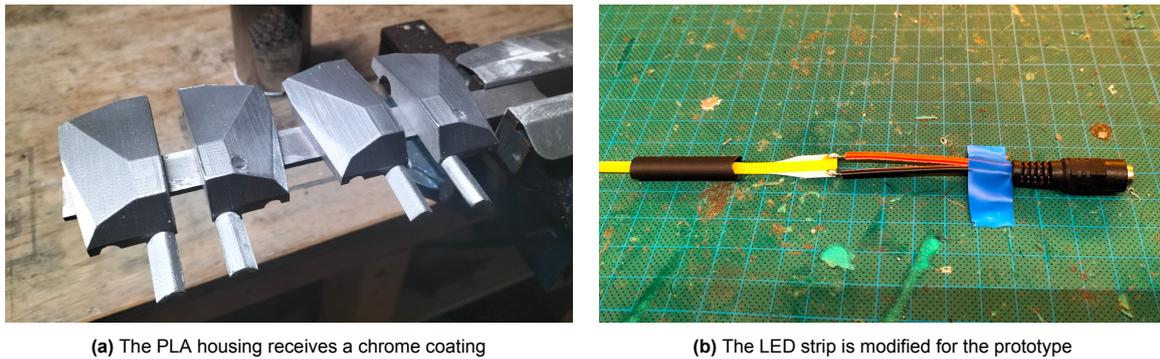
(a) The PLA housing receives a chrome coating

(b) The LED strip is modified for the prototype

Figure 11.7: Additional custom components for this prototype.

With the frame, housing, and electronics complete, the assembly can start. The camera sensor is positioned first. The metal guidewire is then fed through the tube and connected to the LED strip, as shown in Figure 11.8a. The guidewire is used to pull the LED strip into position. The LED strip is folded inwards at the end of the loop. The left side of the housing is screwed onto the tubular frame, shown in Figure 11.8b, and the electronics can be secured in place. The right side of the housing can then be screwed on, as well as the endcap, to finish the assembly of the main components. The assembled device is shown in Figure 11.8c.

(a) Positioning of the electronics

(b) Construction of the housing's left side

(c) Unit testing of the electronics

Figure 11.8: Assembly of the additional components.

The final step is to make the prototype waterproof. The prototype is first checked to see whether all electronics are functioning properly because the final step is harder to reverse. When this is the case, the electronics housing is screwed together again with sealant around the borders. A small plastic lens is stuck onto the camera sensor, and the frame is sealed using transparent heat shrink with an electric heat gun. These steps complete the prototype, ready for testing and evaluation.

Findings

This prototype is fully functional, as shown in Figure 11.9. This prototype is used for the verification and validation of the final design, hence most findings about this prototype are listed in other sections.

The verification of the electronic system is described in Chapter 12. The quality of the camera module, intensity of the light source, and temperature development are all tested in that chapter.

The verification of the structure is described in Chapter 13. The strength of the prototype will be compared to FEA results. The prototype will also be tested on waterproofness. Furthermore, tests on the cost, weight, and dimensions of the prototype will be performed.

The validation of the prototype is described in Chapter 14, with feedback from epert GILLS surgeon J. Gnanraj and comments from a showcase at the ECTMIH 2023.

Figure 11.9: The aluminium prototype imaging a 3D-printed intestinal model.

The complete production process of the prototype was developed in 25 days to drive design choices. The total cost of materials for the four produced units (two test frames and two fully functional prototypes) amounted to approximately €120. The lessons learnt from this production process and recommended improvements are listed below.

The annealed aluminium tubes were very malleable and could even be bent by hand. This made the $20°$ elevation of the upright easy to produce. However, it has yet to be tested if the $20°$ elevation can also be produced on a stainless steel frame using just hand tools. The repeatability of the elevation was also poor, hence custom tooling might be required.

Filling the tube with quartz sand was a necessity. Without filler material, the tube would flatten severely when bent. The filler was pressurised by a first bend (top bend in Figure 11.5b), after which the tube showed almost no flattening anymore for even the small radius bends.

Springback was not taken into account for the design of the custom tooling. As a result, the radius of the loop is 145 [mm] instead of the intended 140 [mm]. The future bending dies therefore need to be designed smaller than the intended radii, using the rule of thumb from Section 10.2.

Drilling the LED holes required extra preparation. The holes at the front of the loop are not on the centre line, and with the current drill jig, the drill bit is not perpendicular to the tube's surface. Consequently, the drill bit tends to "walk" along the surface, producing inaccurate results. Therefore, every hole needed individual marking using a centre punch, a time-consuming step. The future drill jig therefore needs to have angled support holes such that the drill bit is always perpendicular to the loop.

The two parts of the connector were joined by sinking the pole into the frame and the connector joint and glueing it with two-part epoxy adhesive. However, this joining mechanism may not work as well for welding because there is little space to create a weld. A combination of glueing and spot welding may provide the strongest joint.

The LED strip required modifications to help with assembly. The sides of the LED strip are trimmed such that it has less torsional stiffness and can bend around the corners of the loop. The guidewire is a necessity. For the custom LED circuit of the final design, it is recommended to insert it at the open

end of the tube without a power plug, feed it through the frame using a guidewire, and solder on the power plug when the wires come out near the housing.

The extra hole near the camera opening in the tubular frame is required to place the holder for the camera sensor. It also doubles as an extra opening for LED light. Although it is not the weakest point of the structure, it is recommended to remove it and insert the camera sensor holder via the opening itself before assembly.

The 12 [V] female power plug on the prototype has limited resistance to cleaning chemicals. The final design should therefore combine the connection into a single, outgoing USB cable of at least 3 [m]. Such a connection makes the lifting device much easier to clean using chemicals.

The current production techniques to make the prototype waterproof have poor repeatability, are irreversible, and have low reliability. The lens on the camera module can only be secured in place using glue and produces two small bumps at the surface of the lifting device. The housing is sealed using Den Braven Hybridseal, which also acts as a glue and thus makes disassembly and repairs more difficult.

The heat shrink should be applied using a heat gun and not using a lighter, as that leaves soot on the heat shrink. However, a single tear (i.e. an accidental cut with a surgical tool) and the whole tube has to be stripped and replaced. The heat shrink also wrinkles on the inner radius of bends. Furthermore, the temperature required to shrink the tube ($70°$ - $100°$ [C]) means the camera is heated beyond its maximum operating temperature ($70°$ [C]). Hence alternative waterproofing solutions, such as clear infill resin or custom covers, need to be considered for future prototyping.

12

Verification: Electronic system

12.1. Applicable requirements

This chapter marks the start of the verification and validation of the lifting device. The aluminium prototype, described in Section 11.2, will undergo a series of tests and user evaluations to investigate its performance. The first part of the verification is the electronic system.

The unique aspect of this lifting device is the integration of an imaging system, intended to replace the laparoscope during GILLS BTL procedures in low-resource settings. This requires that the imaging system provides higher-quality images than any currently used laparoscope in low-resource settings. It should also provide enough light without overheating, a common problem with currently used laparoscopes. The exact requirements are specified below.

- **P2**   Visibility: The camera should provide better visibility than a state-of-the-art laparoscope from 10 years ago. This will be verified by objectively testing the two selected camera modules from Section 7.2 on four imaging quality factors: (perceived) sharpness, noise, distortion, and colour. These results will be compared to several state-of-the-art laparoscopes from the BovenIJ hospital in the Netherlands, and a development laparoscope camera sensor for low-resource settings from the University of Leeds. This test is described in Section 12.2.

  The camera is supported by an LED lighting system. The main goal of the lighting system is to provide a minimum illuminance of 10.000 [lx] at 100 [mm], as determined in Section 7.3. This is measured with several tests, described in Section 12.3.

- **P3**   Product temperature: The surface temperature of the device may not exceed $41°$ at any point. The lifting device houses the camera module and the lighting system and has no active cooling system. The test in Section 12.4 verifies whether this is sufficient.

12.2. Image quality test

This test aims to determine the image quality of the used camera modules. Image quality is determined in absolute terms using standards from the International Organization for Standardization (ISO) for determining the photographic quality of digital cameras. The selected camera modules are also rated relative to two state-of-the-art laparoscopes from the BovenIJ hospital. It is the most extensive test in the verification process because the usability of this lifting device hinges on its image quality.

Three different camera modules were tested. The first two are the selected camera modules from Section 7.2. However, the camera module with the IMX 258 CMOS sensor used in this test has an autofocus, $75°$ FOV lens system instead of the preferred fixed-focus, $135°$ FOV lens. Furthermore, through collaboration with the University of Leeds, an OmniVision 9734 camera module was also tested. This is a dedicated endoscope camera module with a fixed-focus, 0.9 MP, $90°$ FOV, CMOS sensor and LED lights on its 3.9 [mm] diameter tip. It is used in their development of a laparoscope for low-resource settings. The three camera modules and their specifications are shown in Figure 12.1.

Imaging software affects the image quality of these camera modules. The image quality factor sharpness is therefore tested with the images captured by three different imaging software, for every camera

module. The three imaging software are AMCap (free), Resolume Avenue (€75), and TouchDesigner (free). The capabilities of every software are listed in Section 7.4.

(a) OV5693, fixed-focus, 5 MP, 120° FOV
Approximate cost: €20

(b) IMX258, auto-focus, 12 MP, 75° FOV
Approximate cost: €50

(c) OV9734, fixed-focus, 0.9 MP, 90° FOV
Approximate cost: €90
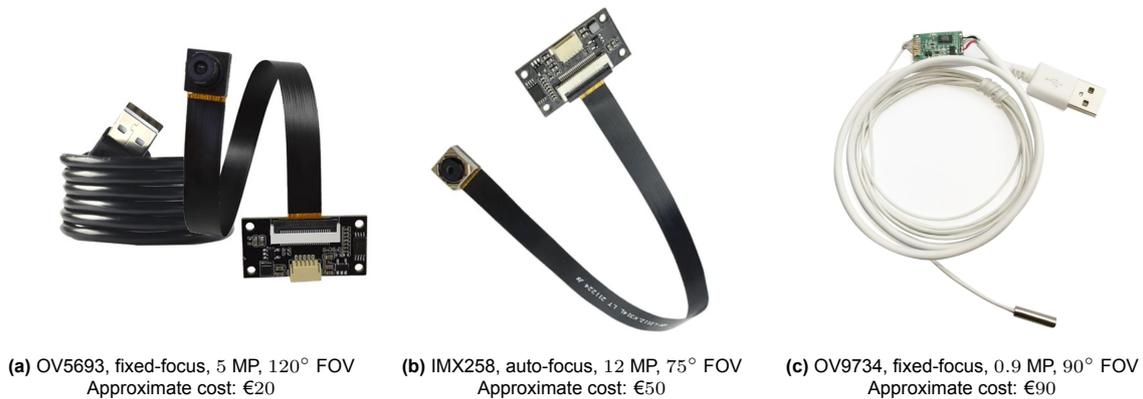
Figure 12.1: The three camera modules investigated in this test. All values are manufacturer's specifications.

Two laparoscopes from the BovenIJ hospital were also tested as a benchmark for the camera modules. These laparoscopes consisted of two different imaging systems with their respective camera heads connected to the same 26003AA 10 [mm] 0° optic from Karl Storz.

The first imaging system is Stryker's 1688 Advanced Imaging Modality (AIM) 4K Platform. It represents the current state of the art for laparoscopic imaging in HICs and has only recently been introduced at the BovenIJ hospital. Biomedical engineers at the BovenIJ estimate that this system costs €25.000.

The second imaging system is Olympus' OTV-S7. It provides Full HD (1920 x 1080 pixels) imaging and has been used in the BovenIJ hospital for the past 15 years. This system is the benchmark of image quality for the camera modules, per requirement P2.

The Pentax Endo-Vision 3000 imaging system, a system from approximately 25 years ago, was also tested. However, its imaging quality has not been analysed because captured images could only be physically printed and not saved digitally.

Method

The camera modules and laparoscopes were tested on two separate occasions on the same test setup. Repeatability was therefore the focus of the test setup design. The setup blocks light from the environment, has a precise positioning system, and comes with three test charts, to accurately determine the five image quality factors for each camera module and laparoscope. All images were analysed using image quality testing software from ImaTest®.

Image quality factors

The five image quality factors are listed below. Note that requirement P2 specifies only four, and not the FOV. However, FOV was also measured to validate the manufacturer's specifications because it is an important parameter for this lifting device.

- **Field of View (FOV):** The lifting device requires a wide-view camera because it has to capture the whole surgical field from a single viewpoint. This is quantified with the FOV, measured in degrees. The FOV is the angle between the outer sight lines of the area of vision. A camera sensor with a wider FOV can capture more area at the same distance than a camera with a smaller FOV [119]. The measurement method is based on ISO 8600-3.

  The FOV is measured horizontally, vertically, and diagonally by picturing a FOV test chart. This is a simple rectangle with known outer dimensions and the same aspect ratio as the camera sensor. For example, the two selected camera modules have an aspect ratio of 4:3, and hence their FOV is determined by measuring the minimum distance at which they can fully picture a 160x120 [mm] rectangle. For laparoscopes with an aspect ratio of 16:9, a 192x108 [mm] rectangle is used.

  The FOV can then be calculated using simple trigonometry, with Equation 12.1 for the horizontal FOV and Equation 12.2 for the vertical FOV. The distance from the camera sensor to the test

chart is d_x, and w and h are the width and height respectively of the pictured rectangle. The same equation can be modified to calculate the diagonal FOV, using the length of the diagonal of the pictured rectangle.

$$FOV_H = 2 * \arctan((\frac{w}{2})/d_x) \quad (12.1) \qquad FOV_V = 2 * \arctan((\frac{h}{2})/d_x) \quad (12.2)$$

- **Sharpness:** Sharpness determines the amount of detail the camera system can reproduce. Camera sharpness is best measured as a Modulation Transfer Function (MTF) [120]. MTF is the contrast at a given spatial frequency, measured in line pairs per millimetre or cycles per pixel, relative to the low-frequency MTF limit of 1. The measure for camera performance is MTF50, the spatial frequency at which the modulation transfer function drops to 50%. A higher MTF50 value is associated with better image sharpness. The measurement method is based on ISO 12233.

MTF50 can be explained using the bar pattern shown in Figure 12.2. The original bar pattern on the left has perfect sharpness, but when pictured with a camera the transition zones blur a little bit. Ergo, at higher frequencies of line pairs per millimetre, the sharpness decreases.

(a) Perfectly sharp bar pattern   **(b)** Slighty blurred bar pattern

Figure 12.2: Example bar pattern, original and with camera degradation.

A luminance (V) amplitude plot (with black $= 0$, white $= 1$) of Figure 12.2b has a decreasing amplitude for higher frequencies due to the increasing amount of grey on the right of the blurred pattern. This is the red line in the example plot in Figure 12.3 [1]. For every frequency, the sine pattern contrast $C(f)$ at spatial frequency f can be calculated using Equation 12.3 and normalized to an MTF value using Equation 12.4.

$$C(f) = \frac{V_{max} - V_{min}}{V_{max} + V_{min}} \quad (12.3) \qquad\qquad MTF(f) = \frac{C(f)}{C(0)} \quad (12.4)$$

The MTF value can also be plotted in the frequency domain, shown as the blue curve in Figure 12.3 [1]. Both frequency and MTF are displayed on a logarithmic scale. The MTF50 value is at 61 line pairs per millimetre in this example.
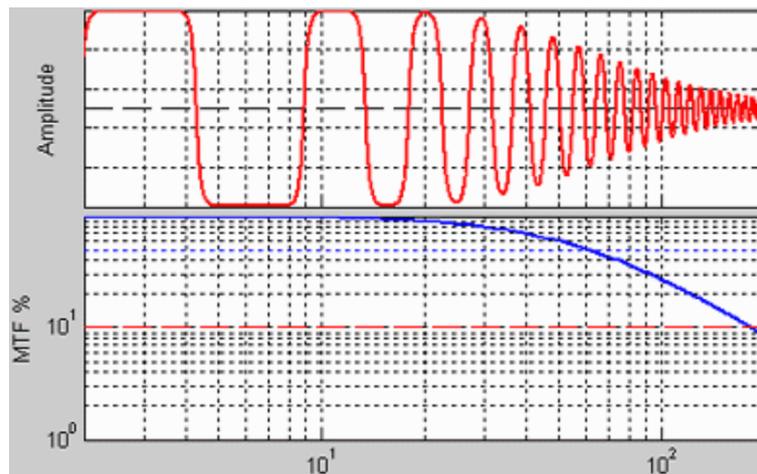

Figure 12.3: Example luminance amplitude plot (red) and MTF plot (blue) for an alternating bar pattern.[1]

---

[1] https://www.imatest.com/support/docs/23-2/sharpness/#MTF_Equation

Using MTF50 has several advantages. It is much less susceptible to observer bias than traditional methods, such as the USAF 1951 chart. MTF50 determines sharpness at an image contrast of 50% of its low frequency, whereas traditional methods correspond to an MTF of roughly 10%. Furthermore, the MTF50 of the complete camera system is the product of its components, whereas e.g. the rise-distance method has no possibility of calculating the rise distance of the complete camera system from its components.

The images from the tested camera modules and laparoscopes are not raw but are already processed. Manufacturers of imaging systems often apply sharpening algorithms, boosting the apparent sharpness by increasing contrast around any edges. However, these algorithms work best for straight lines and can therefore be detected using non-linear test figures. As a result, sharpness is determined with a linear slanted wedge figure, and the effect of sharpening is determined using a non-linear wedge figure. If the peak MTF of the resulting MTF curve is above 100%, sharpening has been applied. [121]

Finally, the results from the MTF measurements can be used to determine the acutance. Acutance is a score for the perceived sharpness, i.e. how sharp the surgeon sees the images on his laptop screen. Acutance scores are determined using the MTF50 curve from the slanted edge. Based on interviews with Indian rural surgeons, an average laptop monitor size of 0.4 [m], and a distance between the surgeon and monitor of 1.5 [m], were used as input.

- **Noise:** Noise is a random variation of image brightness or colour, visible as grain. It is more pronounced in camera sensors with smaller pixels. Noise levels are measured using a stepchart and expressed in two parameters. The measurement method is based on ISO 19264.

  The first parameter is exposure error, which is the difference between the actual exposure of an image and the used exposure level of the camera system. The error is negative for underexposed images and positive for overexposed images, expressed in the unit f-stop. The f-stop scale is logarithmic, meaning that each f-stop represents a doubling or halving of the amount of light reaching the camera sensor.

  The second parameter is the peak Signal-to-noise ratio (SNR), measured in decibels [dB]. Noise is only meaningful in relationship to the signal. A higher SNR indicates a better-quality image because the signal (actual image content) is more prominent relative to the noise.

- **Colour:** Colour accuracy indicates how faithfully the colours in an image represent the true colours of the photographed subject. A ColourChecker chart is used to measure colour accuracy, expressed in three parameters. The measurement method is based on ISO 19264.

  The overall colour accuracy is measured as the ΔE, the mean distance in the Adobe RGB colour space between the true colour and the pictured colour. Secondly, the appearance of the colours is also determined by the image's luminosity. This is measured by a similar parameter ΔL. Finally, white balancing is measured as ΔC, which indicates the whiteness of true white objects in the image. For all three parameters, smaller values indicate smaller deviations in the Adobe RGB colour space and thus better performance.

- **Distortions:** Distortion causes straight lines to curve near the edges of an image. Outward curving, known as barrel distortion, is expected due to the wide FOV of the camera modules. Distortion is measured using a checkerboard pattern, based on ISO 19264.

  Distortion is expressed by the SMIA TV Distortion standard. It covers multiple types of distortion, denoted as an average percentage deviation from the ideal standard.

Test setup

The five test metrics were evaluated using three test charts. One test chart is dedicated to the FOV test, and two more ISO test charts are used for the four image quality factors. The three test charts are shown in Figure 12.4. The first ISO test chart, shown in Figure 12.4b, has 7 wedges and 2 slanted edges to determine sharpness, a block pattern to determine distortions, and colour bars to determine colour. The second ISO test chart, shown in Figure 12.4c, has 3 gradient bars to determine noise. [122]

The two ISO test charts were printed with a high-quality and colour-calibrated printer at 1200 dots per inch (dpi). The high print resolution is necessary to minimize the noise created by the test charts. The FOV test chart was printed on a regular printer. The size of the rectangles is denoted in small font on the FOV test chart and verified using a ruler.

(a) Chart for Field of View (FOV)   **(b)** Chart for sharpness, colour, and distortion   **(c)** Chart for noise
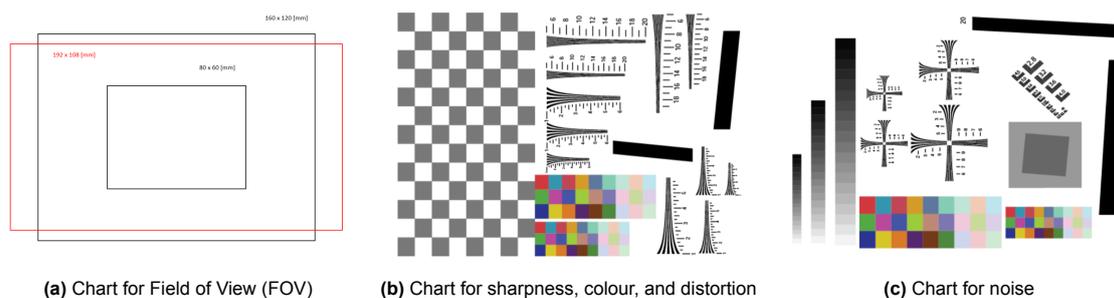
Figure 12.4: The three test charts used in this test.

The three test charts were pictured on a custom test setup, shown in Figure 12.5, with each camera module and laparoscope. The setup is designed such that every picture can be taken at a specified distance and orientation, with minimum variation in available light.

The structure of the test setup is created from a $600\text{x}600$ Thorlabs baseplate and six large 540 [mm] aluminium profiles. This outer structure is covered with a double layer of towel and canvas to shield the setup from light from the environment. Four more small aluminium profiles, equipped with 3D-printed parts, are used to set the distance and orientation of the camera sensors and laparoscopes relative to the test charts.

(a) Render of the structure with just the 3D-printed parts   **(b)** Render with all the components except the shielding
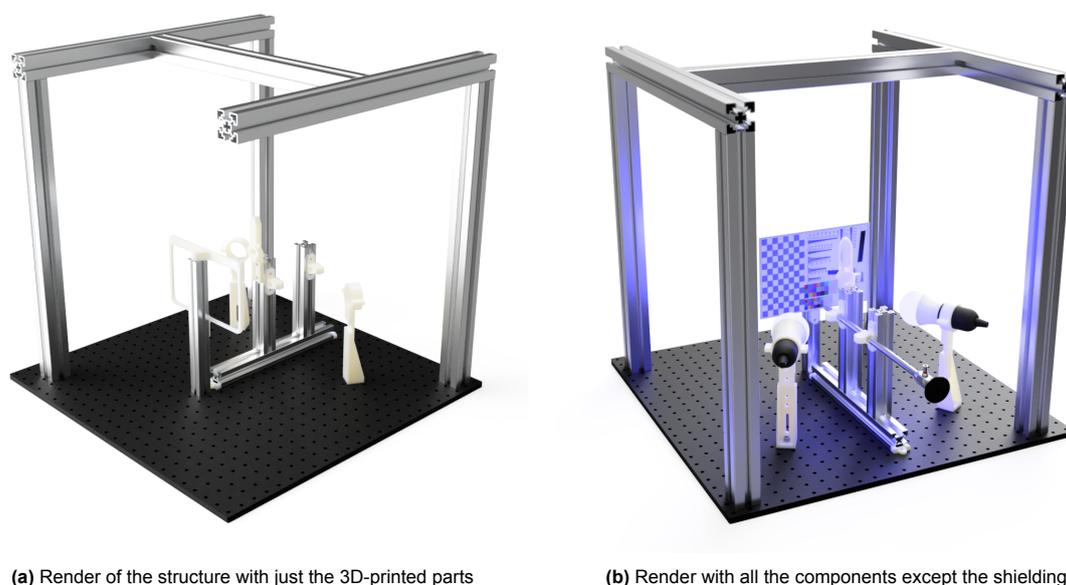
**Figure 12.5:** Two renders of the test setup used for this test.

The test charts are epoxied to a custom 3D-printed chart holder, which is screwed onto a vertical aluminium profile. It can be moved in two horizontal directions in increments of 25 [mm].

The camera sensors are placed inside the elongated, two-part 3D-printed holder. The sensor heads and PCBs of every camera module are secured by shape-fit. The camera holder is centred on the middle of the test chart and can be adjusted in the vertical direction relative to its vertical aluminium profile in increments of 1 [mm]. The vertical aluminium profile itself can move forward and backward over the underlying aluminium rails, such that every camera sensor can be set between 10 [mm] and 200 [mm] from the test charts.

The laparoscopes are connected to two vertical aluminium profiles using two 3D-printed 10 [mm] diameter clamps. The two clamps are used to achieve a perfect horizontal orientation of the laparoscope. The clamps are centred on the middle of the test chart with a horizontal offset of 25 [mm] and can be moved in the same two directions as the camera sensor holder.

Two light sources are placed diagonally behind the 3D-printed holders and clamps on two custom supports. These light sources illuminate the test chart with 2200 [lx], measured at the test chart, and a colour temperature of 6500 [K]. Their height corresponds to the middle of the test chart.

The test setup during use for both tests is shown in Figure 12.6 with all its components.

(a) The test setup with a camera module, without shielding   **(b)** The test setup with a laparoscope
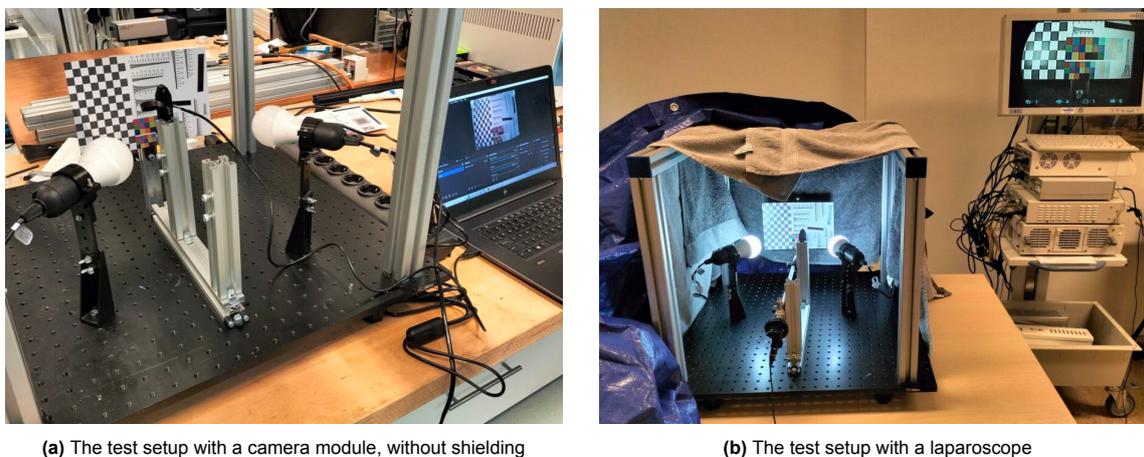
Figure 12.6: Pictures of the test setup used during the two separate tests of the camera modules and laparoscopes.

Results

The results from this image quality test are summarized in Table 12.1. All images were captured from a distance of 100 [mm]. A total of five imaging systems were tested. The OmniVision 5693 CMOS camera module, the Sony IMX 258 CMOS camera module, the Omnivision 9732 CMOS camera module, the Stryker 1688 AIM 4K laparoscope, and the Olympus OTV-S7 laparoscope. For each of the five quality factors, the relevant parameters are listed and highlighted for the best-performing imaging system. The sharpness per imaging software is shown in Figure 12.7.

The OV5693 camera sensor has the widest field of view with a diagonal FOV of $108°$. All three camera modules have a measured FOV_d that is approximately 10% smaller than the manufacturer-specified FOV_d. Both laparoscopic systems have the same FOV because they used the same 26003AA optic from Karl Storz. The measured FOV_d of $88°$ is close to the manufacturer's specification of $90°$. However, the FOV_d of the laparoscopes is likely curtailed because they display 16:9 images cropped out of the original 4:3 image from their sensor.

The absolute sharpness was measured using the MTF50 values for a slanted edge and a wedge figure. Large differences between these MTF50 values, such as for the IMX258 camera module, indicate that sharpening has been applied during the processing of the image. The OV5693 camera module and the IMX258 camera module have the highest sharpness based on the edge MTF50 value, closely followed by the Stryker AIM 4K laparoscope. However, for linear objects, sharpening algorithms boost the sharpness of the IMX258 camera module and the Stryker AIM 4K laparoscope.

The Stryker AIM 4K laparoscope has the highest perceived sharpness. The IMX258 camera module also has the highest possible A+ rating, and the OV5693 camera module has an A rating. The older-generation Olympus OTV-S7 laparoscope has an acutance rating of D, and the OV9732 endoscope camera module has an F (poor) rating.

The exposure errors for the OV5693 camera module and the Olympus OTV-S7 laparoscope are close to zero, indicating their sensors are properly saturated. The other imaging systems have to compensate for areas of underexposure. The SNR is around 30 [dB] for all three camera modules and approximately 20 for both laparoscopes.

The absolute value of colour accuracy is irrelevant, as will be discussed in the next section, but the imaging systems can be compared relative to each other. The IMX258 camera module has the best colour accuracy, followed by the OV5693 camera module and the Stryker AIM 4K laparoscope. These

imaging systems best represent the true colours, capture the highest range of luminosity, and have the most accurate white balance. The Olympus OTV-S7 laparoscope and OV9732 camera module score significantly worse.

The final quality factor is the distortion of each imaging system. The IMX258 camera module has the least distortion due to its small FOV. Both laparoscopes have small SMIA TV distortion scores of less than -5%. The OV5693 camera module has an SMIA TV distortion score of -8%, and the OV9734 camera module performs worst with a score of -16%.

Table 12.1: All results from the image quality testing. The highest scores are marked for every parameter.

Quality factor	Parameters	OV5693	IMX258	OV9732	AIM 4K	OTV-S7
FOV	FOV_h [deg]	**95**	56	72	76	76
FOV	FOV_v [deg]	**79**	44	45	52	52
FOV	FOV_d [deg]	**108**	67	80	88	88
Sharpness	MTF50 - slanted [cy/pxl]	0.17	**0.31**	0.09	0.24	0.10
Sharpness	MTF50 - wedge [cy/pxl]	0.18	**0.19**	0.12	0.17	0.16
Sharpness	Acutance [-]	89 (A)	99 (A+)	44 (F)	**121 (A+)**	63 (C)
Noise	Exposure Error [f-stop]	**-0.1**	-1.4	-1.7	-0.9	-0.3
Noise	SNR [dB]	28	**32**	28	20	21
Colour	ΔE [-]	23	**17**	37	31	38
Colour	ΔL [-]	22	**15**	28	21	26
Colour	ΔC [-]	6	**5**	18	11	20
Distortion	SMIA TV [-]	-8%	**-1%**	-16%	-4%	-5%

The effect of imaging software is shown in Figure 12.7, based on the measurements from the OV5693 camera module. MTF50 is used because it is illustrative for the differences between the imaging software. Resolume Avenue has the highest MTF50 value for the slanted edge, but its MTF50 value for the wedge figure lags approximately 10% behind the two other software.
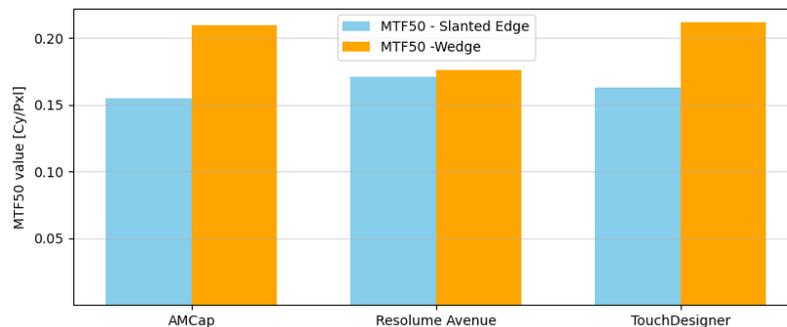
Figure 12.7: Comparison of the three imaging software for the sharpness of the OV5693 camera module at 100 [mm].

Discussion

The discussion of this image quality test is split into two parts. The first part is a critical interpretation of the results per image quality factor. The second part discusses the limitations of this test.

Analysis of results

The performance of imaging systems concerning the first image quality factor, FOV, is best characterised by the diagonal angle. The measured values for FOV_d are all within 50% of each other, which seems to suggest the FOV is pretty similar between all tested imaging systems.

However, the area captured by the imaging systems increases exponentially with the FOV_d angle. For example, at a distance of 100 [mm] the OV5693 sensor can capture 36000 [mm^2], and both laparoscopes can capture 15100 [mm^2], more than double the area for an increase of $20°$. This is graphically

shown in Figure 12.8. The OV5693 sensor can thus capture twice as much area as any other imaging system in the test, making it most suited for use as a wide-view camera on the lifting device.

FOV$_d$: 110°

Area: 391 x10^2 [mm^2]

FOV$_d$: 90°

Area: 192 x10^2 [mm^2]

FOV$_d$: 70°

Area: 94 x10^2 [mm^2]
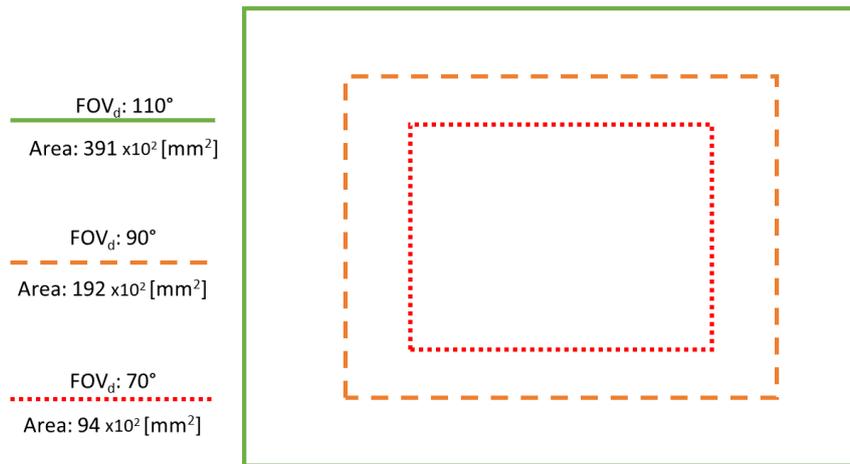
Figure 12.8: The area captured for differing FOVs, assuming a 4:3 aspect ratio, at a distance of 100 [mm].

The sharpness of the imaging systems was measured using two test figures to detect sharpening. Sharpening algorithms increase contrast around edges, and therefore work best on linear objects. Hence for imaging systems with sharpening, the linear slanted edge appears sharper than the curved wedge resulting in a higher MTF50 value for slanted edge. The Stryker AIM 4K laparoscope had a sharpening setting (it was set to its lowest setting for the test) which illustrates the concept, shown by the two pictures in Figure 12.9. Anatomical structures are seldom linear and therefore traditional sharpening algorithms are not necessary for the camera module used in the lifting device.

The resolution of the camera modules has been verified using imaging software, and all camera modules could produce images in the advertised maximum resolution. Note that a high resolution does not equal high sharpness, as a high-resolution image can still be out of focus. However, a combination of high resolution and high sharpness does lead to a higher perceived sharpness. The test chart was deemed sufficiently sharp as none of the cameras exceeded a resolution of 30 MP [123].

Perceived sharpness is an important parameter for the use of imaging systems in practice. Perceived sharpness benefits from small amounts (peak MTF $< 130\%$) of sharpening. Consequently, the Stryker AIM 4K laparoscope and IMX258 camera module have the highest possible A+ rating for acutance. The OV5693 camera module also performs well with an A rating, especially considering it has almost no sharpening. The benchmark for this test is the Olympus OTV-S7 which scores a C rating. To conclude, both the OV5693 and IMX258 camera modules provide sharp imaging that outperforms a state-of-the-art laparoscope from 10 years ago and is close to the current state-of-the-art laparoscope.

(a) Test chart capture with minimum (1/8) sharpening

**(b)** Test chart capture with maximum (8/8) sharpening
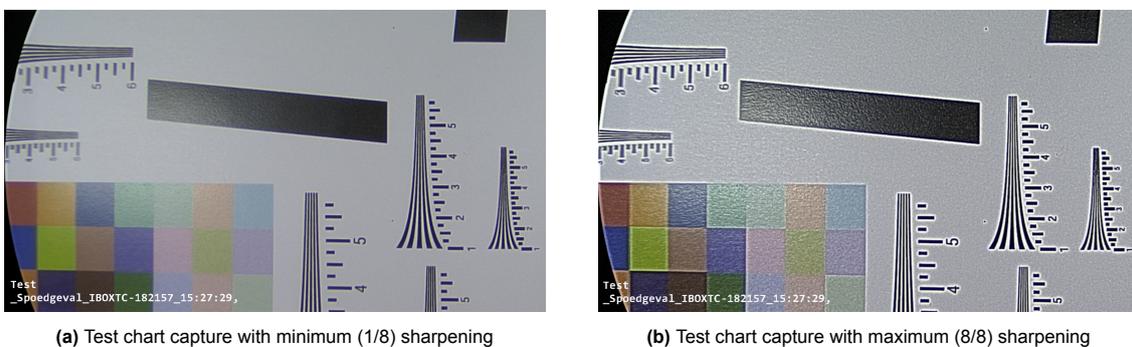
Figure 12.9: The visual effect of the sharpening setting from the Stryker AIM 4K laparoscope.

For noise performance, the OV5693 camera module is the only imaging system that is better than both laparoscopes. It has the lowest exposure error, meaning the luminance of its pixels is close to the actual luminance. All measured SNRs are rated as excellent by the sued ISO 19264 standard. However, the higher SNRs of the camera modules indicate they work even better in low-light conditions.

The absolute colour accuracy is heavily dependent on lighting conditions and therefore hard to quantify. However, comparisons from the same test setup (with the same light conditions) are valid. The OV5693 and IMX258 camera modules have a significantly better colour accuracy ΔE than the benchmark Olympus OTV-S7 laparoscope and are comparable to the current state-of-the-art Stryker AIM 4K laparoscope.

The colour accuracy is strongly related to ΔL. If a camera sensor is not properly saturated, different tones of colour are harder to distinguish. The laparoscopes may be calibrated for a higher target illuminance than the 2200 [lx] produced by both light sources, explaining their darker colour appearance. Furthermore, the Stryker AIM 4K laparoscope had a low luminance setting of 3/8 and captured images were noticeably darker than displayed on the screen during the test. In summary, the colour accuracy results of both laparoscopes are not representative of their true performance.

The visual difference in colour accuracy between the IMX258 camera module and the current state-of-the-art Stryker AIM 4K laparoscope is shown in Figure 12.10. The relation between ΔE and ΔL is also visible here. The Stryker AIM 4K laparoscope's sensor is less saturated than the IMX258 camera sensor and therefore reproduces darker colours.

(a) Colour accuracy of the IMX258 camera module   **(b)** Colour accuracy of the Stryker AIM 4K laparoscope
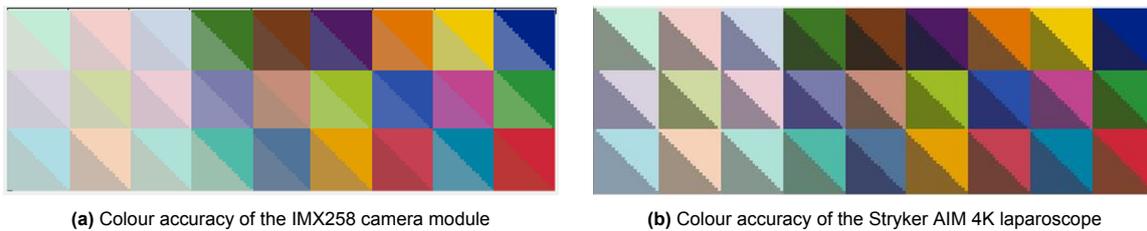
Figure 12.10: The visual effect of different colour accuracy performance.

The score for distortion has one important caveat. The checkerboard pattern was not captured at a fixed distance of 100 [mm], but at the distance at which the checkerboard was in full frame. This was done to determine the distortion value of the whole sensor.

Distortion scores have to be related to FOV. Sensors with a large FOV have distortions around the edges, in areas that sensors with a smaller FOV do not even capture. This is illustrated in Figure 12.11, by comparing the OV5693 and IMX258 camera modules. The OV5693 camera module has the second-highest SMIA TV score for distortion, compared to just -1% for the IMX 258 camera module. However, it also captures four times the area of the IMX258 camera module. This is visible if the image size from the IMX258 camera module is overlayed on the image from the OV5693 camera module, as shown in Figure 12.11b.

(a) Distortion capture for the IMX258 camera module   **(b)** Distortion capture for the OV5693 camera module
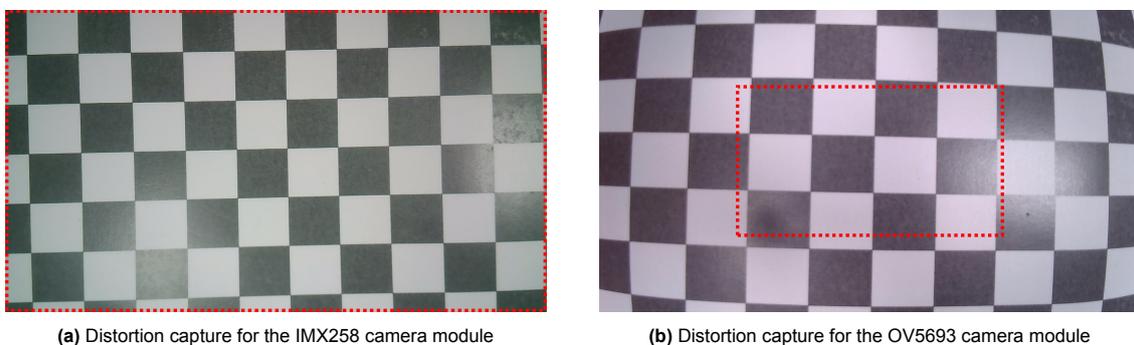
Figure 12.11: Relation between distortion and FOV. The red rectangle in the OV5693 camera's image represents the area that would be captured by the IMX258 camera. Notice how significant distortion only occurs outside of the rectangle.

Finally, the different imaging software seems to have little influence on image quality. However, the image quality using Resolume Avenue was visibly better than the other two imaging software. This is mostly due to the used methodology. Screenshots were taken from every software. These were not always at full screen, and the displayed image had to be captured and processed again, introducing artefacts and consequently reducing image quality.

Limitations of methods

There are several limitations to this image quality test. Comparison to other research is limited due to the test setup and methodology. The results for the 12 quality factor parameters for the five imaging systems are based on singular data points. Every parameter value, e.g. the exposure error for the OV9732 camera module, is based on the ImaTest®analysis of a single capture. The images were visually checked for large artefacts, but any random discrepancies between them were not accounted for. Therefore, any small differences between parameter values of different imaging systems could be noise in the measurement and only large differences are of significance.

Furthermore, the test was conducted in two parts with only limited cross-validation. The three camera modules were tested at a different time than the two laparoscopes due to logistic reasons. Variability between the tests was minimized by using the same test chart, at the same distance and orientation relative to the imaging systems. The light sources also had the same luminosity and the same orientation. The outside light was blocked using a double layer of towel and canvas. During both tests, the OV5693 camera module was used to capture the test charts for cross-validation. No significant differences were detected for any of the image quality factor parameters.

The lighting conditions have a large influence on the absolute values of most image quality factor parameters. Comparison to other research is not possible because these studies used different lighting conditions. The two light sources provided 2200 [lx] at a colour temperature of approximately 6500 [K]. The light source colour temperature was not verified. Hence only comparison between the tested imaging systems is possible.

Some of the imaging systems have a built-in light source. The OV9732 camera module has LEDs on the tip and the two laparoscopes could be equipped with a laparoscopic light source. These built-in light sources were not used during the test to get the most objective results for just the camera sensors. However, system performance (imaging system and lighting system) is important because it reveals how well the imaging from the system as a whole is. It is important to note here that the OV5693 camera module was perfectly saturated at 2200 [lx], suggesting much less than the recommended 10.000 [lx] may suffice for the lifting device.

For example, the LEDs of the OV9732 camera module are very weak, and thus its system performance would drop relative to its camera sensor in this test. In contrast, the laparoscopes are calibrated to their laparoscopic light sources so their performance would increase relative to this test. The OV5693 camera module on the lifting device will also work in conjunction with a ring of LED light. The system performance relative to this test would show how well this lighting system works.

The imaging systems are not tested in any special conditions that could occur during BTL procedures. For example, an excessive amount of red in the image (due to blood, tissue, etc.) can cause blooming. Blooming means that the image is tinted in the dominant colour, red. Laparoscopes have algorithms that prevent blooming, whereas the OV5693 camera sensor seemed sensitive to red blooming. This is an aspect that has to be tested still. Similarly, the performance of the camera modules in the presence of smoke or fog needs to be tested [124].

Conclusion

The OV5693 camera module is best suited for the application of this lifting device due to its wide FOV and excellent performance relative to both laparoscopes, especially considering its price point. The OV5693 camera module outperforms the benchmark for imaging performance, the Olympus OTV-S7 laparoscope, as shown in Figure 12.12, and comes close to the current state-of-the-art Stryker AIM 4K laparoscope. It provides sharper imaging, with more accurate colours and less noise than the benchmark. Its distortion score is higher but it also captures twice the area. The OV5693 camera module also has excellent low-light performance and produces well-saturated images with only $1/5$ of the recommended illuminance.

(a) Test chart capture using the OV5693

(b) Test chart capture using the OTV-S7
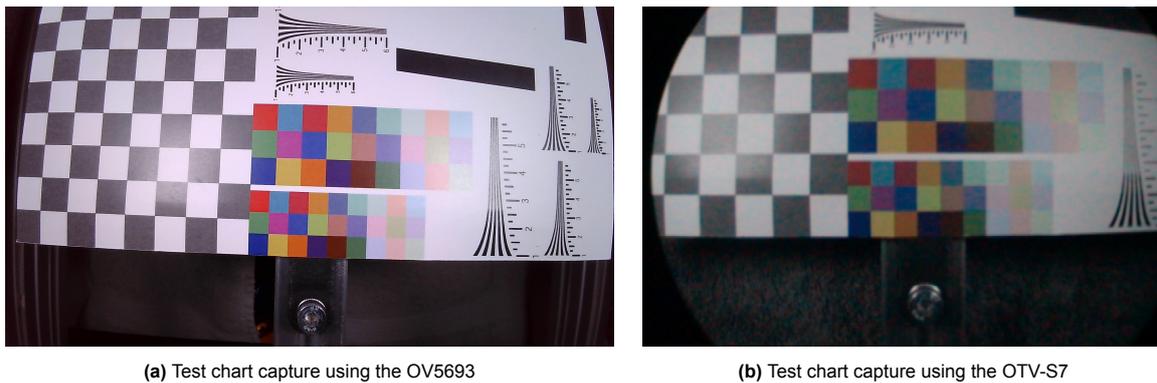
Figure 12.12: Comparison of the image quality between the OV5693 camera module and the benchmark Olympus OTV-S7 laparoscope. FOV, sharpness, noise, colour accuracy and distortions are all visibly different.

Using the IMX258 camera module with a wide-FOV, fixed-focus lens system is a good second option. This camera module is more expensive but also provides higher-resolution imaging that is even sharper and more colour-accurate. Its image quality matches that of the Stryker AIM 4K laparoscope. The use of Resolume Avenue as imaging software is recommended even though it could not be substantiated.

The use of the OV9732 endoscopic camera module is not advised because it performs worst of all imaging systems on almost all image quality factor parameters and its own LEDs are weak.

12.3. Light intensity test

This test aims to quantify the illuminance of the LED lighting system used in the prototype. The requirement from Section 7.3, based on literature, is a minimum illuminance of 10.000 [lx] at 100 [mm]. However, the previous test in Section 12.2 proved that approximately 2000 [lx] at 100 [mm] is sufficient to saturate the used OV5693 camera module.

Method

Three separate tests were performed to evaluate the lighting system. The first test is a comparison between five commercially available LED strips and aims to determine which strip has the highest light intensity. The second test investigates the effect of LED strip length on illuminance. The third test quantifies the efficiency of the LED holes in the structure and the effect of the heat shrink sealing. For all three tests, the illuminance values are measured at a distance of 100 [mm].

The first test compares five different commercially available pre-assembled LED strips, to determine their light intensity. The five tested LED strips are the three selected strips from Figure 7.7, another 5 [V] strip with an on/off switch, and a 12 [V] SMD strip with 120 [LEDs/m]. Every strip has a colour temperature of approximately 6000 ± 250 [K].

The five strips are shown in Figure 12.13, with their voltage, number of LEDs per meter, type of LED chip, strip width, beam angle, power consumption, and power control option (power plug, dimmer, or on/off button) listed in the caption. All values are the manufacturer's specifications.

The setup from the image quality test in Section 12.2 was used as a basis for this test, shown in Figure 12.14. The test chart holder was replaced by a custom 3D-printed holder for the ILM-201L illuminometer from RS PRO. It has four measuring ranges: 200, 2000, 20000, and 200000 [lx], with 3-digit reading and an accuracy of $\pm 8\%$.

Strip sections of 750 [mm] were used. These sections were placed between two vertical aluminium profiles from the structure, at the same height as the illuminometer's sensor, at a horizontal distance of 100 [mm] from the illuminometer. Consequently, 450 [mm] of the strip illuminated the illuminometer. The setup is shielded from outside light using a double layer of towel and canvas.

The illuminance of 450 [mm] of every strip, at a distance of 100 [mm], was measured five times for every strip in random order. Every single measurement consists of a base illuminance of the environment, with the LED strip off, and the total illuminance with the LED strip on. The difference between these two values is the effective illuminance of the LED strip.

Figure 12.13: 250 [mm] sections of the five LED strips that were tested for use in the prototype, from top to bottom:
1) 12 [V] 120 [LEDs/m] SMD strip, 8 [mm], $120°$ beam angle, 8 [W/m], plug
2) 12 [V] 528 [LEDs/m] COB strip, 10 [mm], $180°$ beam angle, 14 [W/m], plug
3) 12 [V] 480 [LEDs/m] COB strip, 8 [mm], $180°$ beam angle, 11 [W/m], plug
4) 5 [V] 320 [LEDs/m] COB strip, 8 [mm], $150°$ beam angle, 6 [W/m], on/off
5) 5 [V] 320 [LEDs/m] COB strip, 8 [mm], $150°$ beam angle, 9 [W/m], dimmer

The second test aims to quantify the effect of the prototype's LED strip length on illuminance. The prototype uses the 12 [V] 480 [LEDs/m] COB strip, the third strip in Figure 12.13, which has a power rating of 8 [W/m]. However, a single USB-A port can only provide 7.5 [W] at 5 [V] and requires a step-up boost converter to power a 12 [V]. If the strip is too long, it may therefore be underpowered.

The effect of length on illuminance is measured using the test setup shown in Figure 12.14a. The length of the LED strip will be varied between 50 and 950 [mm] in increments of 100 [mm], with a maximum measurement section length of 450 [mm]. The base illuminance and total illuminance are measured five times for every length of strip. For this test, measurements are taken in descending order, because the same strip is used for all measurements and shortened in length with every increment.
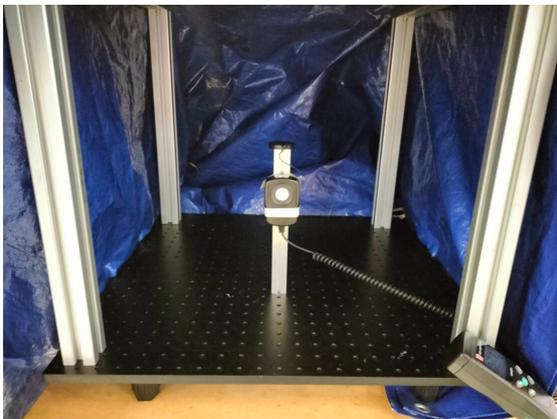
(a) Test setup for measuring light intensity

(b) Test frame used to determine total illuminance

Figure 12.14: Test setup and test frame used for the three light intensity tests.

The third test determines the illuminance of the prototype. This will be measured with and without heat shrink to quantify its effect. A custom test frame is used, shown in Figure 12.14b, with the same loop dimensions as the prototype. The heat shrink is applied using a heat gun shown, and the resulting frame is tightly sealed apart. The test frame is placed perpendicular to the illuminometer, with its ring a distance of 100 [mm] away from the sensor. The base illuminance and total illuminance are measured to calculate the total illuminance.

Results

The results for the first test are shown in Figure 12.15a. The illuminance measurements of the five LED strips from Figure 12.13 range from 1000 to 3200 [lx]. The two 5 [V] COB strips and the 12 [V] 528 [LEDs/m] COB strip (LED strip 4, LED strip 5, and LED strip 2 respectively) provide the least amount of light at around 1200 [lx]. The 12 [V] 480 [LEDs/m] COB strip (LED strip 3) almost doubles that at 2040 [lx], and the 12 [V] 120 [LEDs/m] SMD strip (LED strip 1) tops the chart at 3110 [lx].

(a) Average illuminance for different LED strips

(b) Average illuminance for varying LED strip lengths
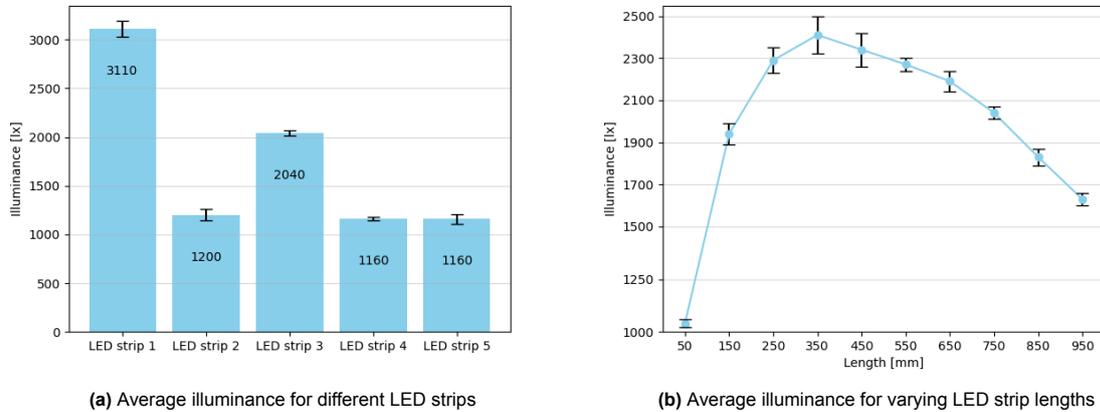
Figure 12.15: Average illuminance of every strip from Figure 12.13 and for varying lengths of LED strip 3.

The illuminance of the 12 [V] 480 [LEDs/m] strip was measured at 10 different lengths, ranging from 50 to 950 [mm], shown in Figure 12.15b. The strip has the highest illuminance between 250 [mm] and 650 [mm]. For strip lengths over 650 [mm], the USB-A connection does not provide enough power anymore. For strip lengths shorter than 250 [mm], the test section is too short compared to the standard 450 [mm] section and has physically too few LED chips. The error bars for these measurements seem larger than in Figure 12.15a, but this is largely due to the smaller y-axis range used in the figure.

The results of the third test are shown in two figures in Figure 12.16. The total illuminance of the prototype is difficult to summarize in a single value because it depends on where it is measured. Therefore, the illuminance of the prototype was evaluated on a 200 x 250 [mm] grid, with stepsize 25 [mm], resulting in 99 measurements. The measurements are graphically shown in a 3D surface plot in Figure 12.16a and a 2D surface plot in Figure 12.16b. The dashed grey circle indicates the position of the prototype relative to the measured illuminance values. The black arrow inside the circle shows the forward orientation of the prototype. The illuminance peals near the front part of the loop at 1640 [lx].

(a) Illumination 3D surface

(b) Illumination 2D surface
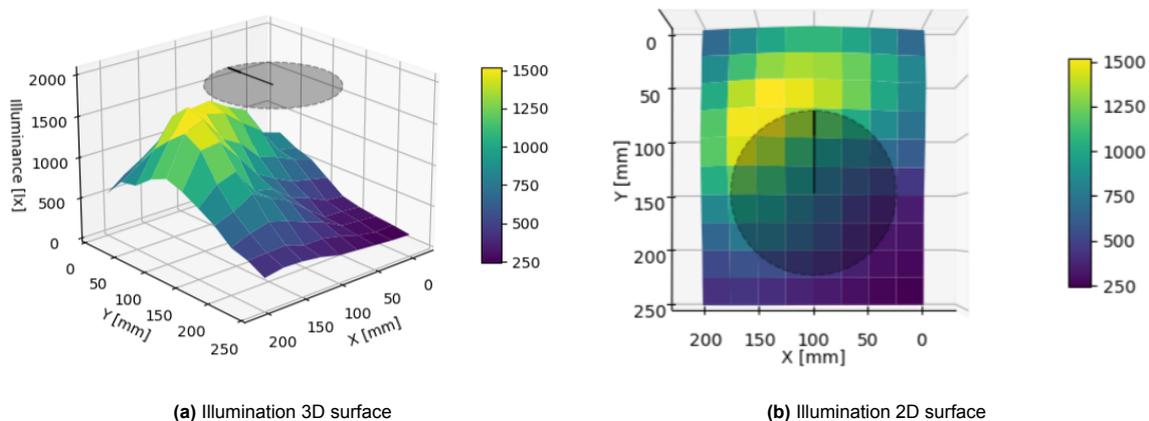
Figure 12.16: Illuminance distribution of the prototype with heat shrink. The dashed circle indicates its position.

The results in Figure 12.16 are from the prototype with heat shrink applied and a double-folded

LED strip. Double-folded means that the excess strip near the open tube end is folded inwards over the length of the loop. Heat shrink reduces the illumination of the prototype by approximately 20%. Double-folding the LED strip increases the illumination of the prototype by approximately 50%.

Discussion

The three tests provide an indication of the performance of an LED lighting system based on commercially available LED strips. However, the results require critical interpretation. For example, the first test is only used for comparison of the five selected LED strips. The test is no measure of their absolute performance or the validity of the manufacturer's specifications.

The single LED strip based on SMD technology is the clear winner of the first test. However, this SMD strip has limited applicability in the prototype because its beam angle is $120°$ and it generates noticeably more heat than the COB-based LED strips. The performance of the 12 [v] 528 [LEDs/m] COB strip was likely hindered because the 750 [mm] strip section requires more current than the USB-A connection could provide. Hence the 12 [v] 480 [LEDs/m] COB strip was chosen to continue further testing and for prototyping.

The second test showed a degradation of illuminance for strip lengths over 650 [mm]. This confirmed the calculations from Section 7.3 which estimated a maximum strip length of 600 [mm]. Therefore, as a rule of thumb for 12 [V] LED strips, 6 divided by the listed power usage in [W/m] is the maximum strip length in [m] that can be powered by a laptop USB-A connection.

The second test has also been tried with the strip inside the prototype. The loop of the prototype has a length of approximately 300 [mm]. It can therefore be powered by a 300 [mm] strip or a double-folded 600 [mm] strip. The double-folded 600 [mm] strip increased the illumination by 50% and is therefore preferred for the prototype. The influence of double-folding on temperature is measured in the next Section 12.4. The polyolefin heat shrink shielding reduces illumination by 20%.

The third test determined the total illumination of the prototype. With a peak of 1640 [lx] it does not provide enough light to meet the requirement from Section 7.3 or the conclusion from Section 12.2. User validation in Chapter 14 shows that this amount of light output is no barrier for low-resource settings, but a stronger light source is still recommended for further prototyping.

The distribution of light is concentrated on the field of view of the camera module, which spans roughly from $x = 0, y = 0$ to $x = 200, y = 150$, but it is not symmetric. The left side of the field of view receives up to 40% higher illumination. This is a significant difference, which is partly due to the prototype's design and partly because a set base illuminance was used for every measurement point. The lifting device can be improved by placing more holes near the end of the tube, i.e. focused on the right side of the field of view.

Limitations of methods

The illumination of the LED strips over time was not measured. All strips have a manufacturer-specified lifetime of over 50.000 [hrs] and hence severe degradation per hour is not expected.

The second test would be more accurate if the power consumption was measured in conjunction with the light output. The power measurement would clearly show when the maximum of the USB-A port is reached and thereby provide a better estimate for the power usage [W/m] rule of thumb.

The third test would be more insightful if the illumination of the benchmark Olympus OTV-S7 laparoscope was measured for comparison. This measurement would allow for direct evaluation of requirement **P2**, and show the differences in maximum illumination and illumination distribution between a laparoscopic light source and a ring of LED light. The first recommendation from this test is therefore to measure the illumination distribution of the benchmark and state-of-the-art laparoscopes at their respective working distances.

All three tests were susceptible to variations in distance. These variations have a large effect on the measurements because illuminance is quadratically related to distance. For this reason, the first two tests were performed 5 times. However, the results from the third test are based on single measurements. It is therefore recommended to do this test again for the next prototype, with several measurements per point and a base illuminance measurement per point.

Conclusion
The LED lighting system used for the prototype provides too little light to meet the requirements. This requires more realistic a requirement, based on the camera module's saturation, but also requires a stronger lighting system. A custom LED lighting system, as described in Section 7.3, is therefore recommended for further development. The loop of the lifting device should also have more holes near the end of the tube to provide a symmetric light distribution. For the next prototype, it is recommended to redo the third test and compare the lifting device to a state-of-the-art laparoscope.

12.4. Temperature test
This test aims to quantify the temperature of the lifting device in use. Based on initial user tests, the suspicion arose that the lifting device prototype generated too much heat. Therefore, the hypothesis is that if the prototype were to be used in a GILLS BTL procedure, then it would heat up beyond the maximum allowed $41°$ [C] from requirement **P3**.

Method
During a GILLS BTL procedure, the lifting device will be inside the abdominopelvic cavity for up to 2 hours. This environment is a closed space with high humidity and an average temperature of $36.6°$ [C] [125]. This means little heat could be dissipated to the environment without exceeding $41°$ [C].

In contrast, the temperature of the prototype is measured in a laboratory, which is an open space with a constant average temperature of $22°$ [C]. The test setup is shown in Figure 12.17b. If the prototype becomes too hot in this environment, it will surely overheat inside the abdominopelvic cavity.

The temperature of the prototype is measured three times for a period of 120 minutes. All electronics are switched on. The test frame from the previous test in Section 12.3 is used, again with heat shrink applied and a double-folded LED strip.

(a) Test setup for measuring light intensity   (b) Test frame used to determine total illuminance

Figure 12.17: Thermometer and test setup used for the temperature test.

A Reed 882 infrared thermometer was used for this test, shown in Figure 12.17a. It has a temperature range of $-50°$ [C] to $550°$ [C], with a temperature resolution of $0.1°$ [C] below $200°$ [C]. The accuracy of the measurements is $\pm2°$ [C]. The temperature is measured every 5 minutes at four points on the prototype. The environmental temperature is also measured every 5 minutes.

Results
The main result is a graph of the prototype's temperature over time, shown in Figure 12.18. The environmental temperature remained constant at $22°$ [C] during all tests. The device heats up in approximately 15 minutes, after which it settles at a constant temperature. The double-folded LED strip causes the ring to heat to $42°$ [C], which is above the maximum allowed temperature.

However, the section of the prototype that houses the camera (indicated by the yellow dot in Figure 12.18) does not heat up as much. Its temperature averages at $26°$ [C], only $4°$ [C] above the environment temperature.
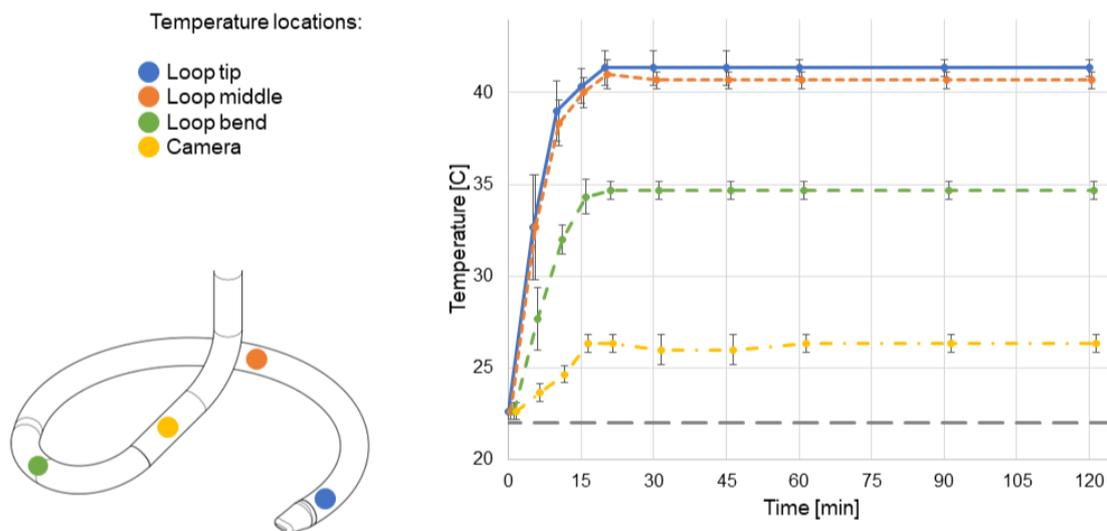
Figure 12.18: Temperature of the prototype over time, measured at four points. The maximum temperature is $42°$ [C]. The grey horizontal line indicates the environment temperature was a constant $22°$ [C].

Discussion

The results of the test confirm the hypothesis. The prototype heats up beyond the maximum allowed $41°$ [C] within 20 minutes, in an environment that is approximately $15°$ [C] cooler than what is customary during GILLS BTL procedures. Therefore, it is reasonable to assume that the prototype would heat beyond $41°$ [C] during a 2 hour GILLS procedure.

The excessive heat is caused by the individual resistors of the LED strip, evidenced by the difference in temperature between measurement points. The measurement points with double-folded LED strips (blue and orange) average $41°$ [C], the measurement point with a single-fold LED strip (green) averages $35°$ [C], and the camera (yellow) averages $26°$.

A single-fold LED strip reduces the temperature of the prototype by $5°$ [C] but also reduces illumination by approximately 33%. The camera sensor does not generate much heat and can therefore be used for further development. The increase to $26°$ [C] is partly due to the nearby LED strip.

The quick heating up of the prototype is partly caused by the high thermal conductivity of aluminium 6060-T66, which is 150 $[W/mK]$. Moreover, the LED strip is directly bonded onto the inside of the tubular frame without insulation. In comparison, stainless steel 316L or 17-4PH has a thermal conductivity of approximately 15 $[W/mK]$ and will thus heat up less quickly.

Based on this temperature test, it is recommended to discontinue the use of pre-assembled LED strips for the lighting system. The resistor placement (see Figure 7.6a) means the strips generate too much heat in the loop. A new lighting system, combined with simple insulation, can be tested on the same setup. If that shows promising results, with temperatures exceeding the environment by only a few degrees, a second test setup more akin to the abdominopelvic cavity should be designed. Furthermore, the electric power consumption of the electronic has not been measured but that is recommended for future tests because it indicates the thermal efficiency of the complete device.

13

Verification: Structure

13.1. Applicable requirements

This chapter is the second part of the verification of the lifting device. The structure of the lifting device, as designed in Chapter 10, is verified using the aluminium prototype. The structure needs to provide support and protection to the electronics, and both aspects are separately tested. Furthermore, several smaller tests are performed to verify four more requirements. The total of six requirements are listed below, with a rationale.

- **P1** Abdominal wall lifting: The lifting device must be able to sustain a load of 140 [N], distributed around the loop. The aluminium prototype will be tested in Section 13.2, and the results will be extrapolated for the stainless steel frame.
- **C1** Low upfront purchase price: The lifting device may cost no more than €250. In Section 13.3, a cost estimation for the final design is performed.
- **R1** Dust- & waterproof: The structure of the device should be dustproof and waterproof with respect to the electronics at the IP67 level. The corresponding test is described in Section 13.3.
- **D1** Weight: The lifting device may weigh no more than 1 [kg]. In Section 13.3, the prototype will be weighed, and the results will be extrapolated for the stainless steel frame.
- **D2** Insertion diameter: The diameter of insertion may not exceed 12 [mm] at any point. This requirement is verified in Section 13.3.
- **M1** Compatibility with extractors: The lifting device should be compatible with the RAIS retractor arm. This requirement is also verified in Section 13.3.

13.2. Structural strength test

This test aims to determine the structural strength of the aluminium prototype. Requirement **P1** specifies that the lifting device should be able to sustain a load of 140 [N]. The lifting device has been designed for this load in Fusion 360 based on the use of stainless steel 440C, with a safety factor of 2. The performance of the aluminium prototype relative to simulated stress tests in Fusion 360 allows for some initial predictions about the structural strength of a stainless steel lifting device.

Method

The structural strength test is a force-displacement measurement of an aluminium prototype. The prototype has a custom M3 threaded joint to connect it to a Futek LSB210 FSH03943 loadcell, shown in Figure 13.1a. The loadcell has a maximum capacity of 100 [lbs] and is calibrated from -200 to 200 [N]. It is connected to a Festo EGSL linear stage, shown in Figure 13.1c, using a custom aluminium joint. The linear stage has a stroke of 200 [mm] at a constant velocity of 5 [mm/s] and it can withstand a maximum axial load of 300 [N].

The prototype is clamped by a 300x200 [mm] section of Rayyl artificial skin, shown in Figure 13.1b. The artificial skin is secured to the Thorlabs baseplate using 35 M6 bolts with washers. This setup aims

to replicate the force distribution on the lifting device during GILLS procedures. The prototype is pulled up 40 [mm] in the vertical direction while measuring the force.

(a) Custom aluminium joint   (b) Complete setup with Rayyl artificial skin   (c) Festo linear stage
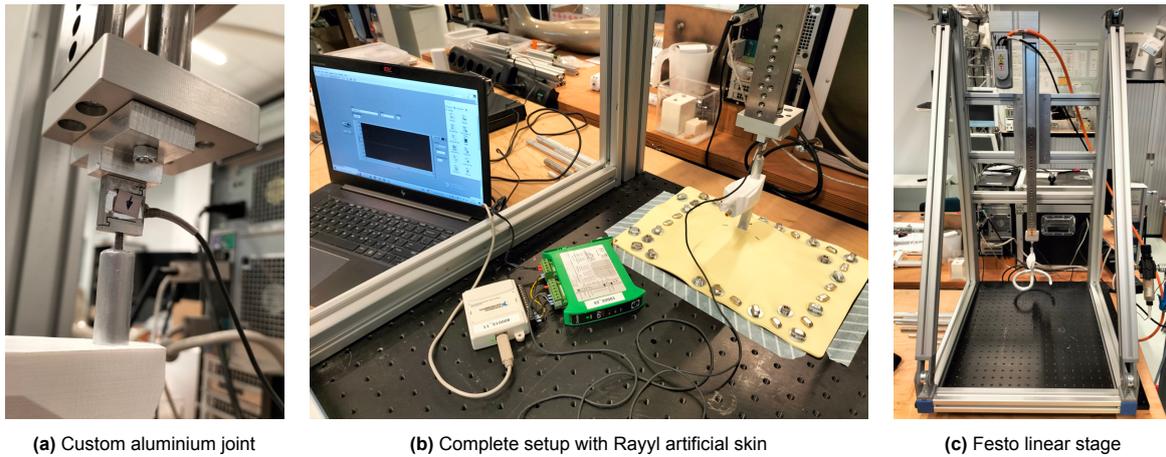
**Figure 13.1:** The test setup and prototype used for the structural strength test.

The load-carrying frame of the prototype is made from thermally treated aluminium 6060-T66. This material has a Young's modulus of 68 [GPa], a yield strength of 170 [MPa], and an ultimate tensile strength of 220 [Mpa] [126]. Additional parts are made from PLA.

The FEA tool from Fusion 360 is used to simulate the structural strength of the prototype. Using the abovementioned materials and a safety factor of 2, the prototype is predicted to sustain a maximum load of 31 [N], thereby displacing 1.8 [mm]. This is approximately 22% of the design load 140 [N], which corresponds to the yield strength ratio between aluminium 6060-T66 and stainless steel 440C. The load distribution is shown in Figure 13.2a.

The FEA tool from Fusion 360 calculates that the static stress will exceed the yield strength at 62 [N]. The simulation is shown in Figure 13.2b. The expected point of failure is the first LED hole.

(a) FEA results for a distributed load of 31 [N]   (b) FEA results for a distributed load of 62 [N]
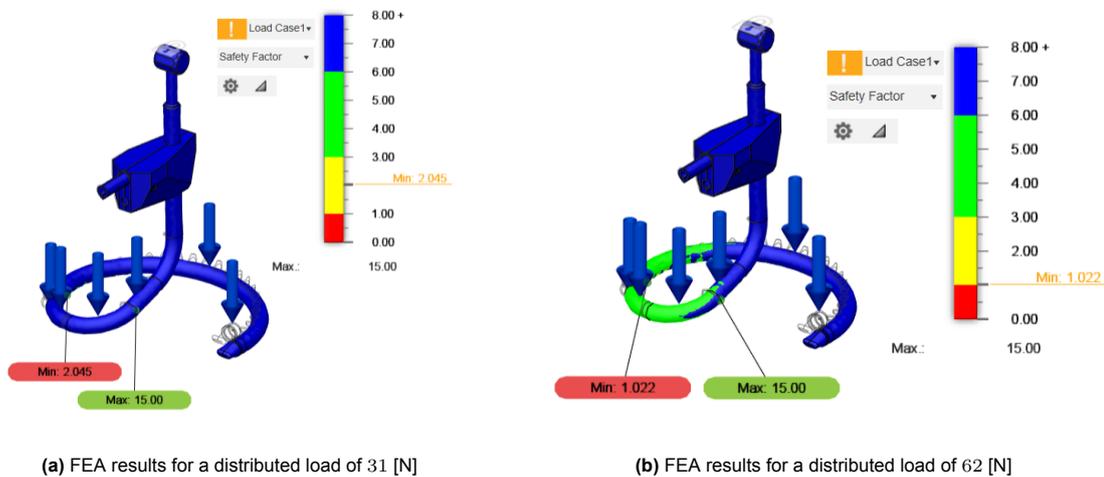
Figure 13.2: FEA results for the aluminium prototype. The loads result in a minimum safety factor of 2 and 1 respectively.

Results

The main results of the structural strength test are the two graphs shown in Figure 13.3. The left graph shows the raw data from the load cell (force [N]) and from the linear stage (displacement [mm]) over time. The right graph shows the corresponding force-displacement graph.

The force-displacement graph clearly shows when the prototype starts to fail, as the slope changes from 34 [N/mm] to 11 [N/mm]. It starts at approximately 50 [N], for a vertical displacement of 1.5 [mm]. The load cell reaches its maximum of 200 [N] before the end of the measurement.

(a) Force and displacement plotted over time

(b) Force plotted over the first 20 [mm] of displacement
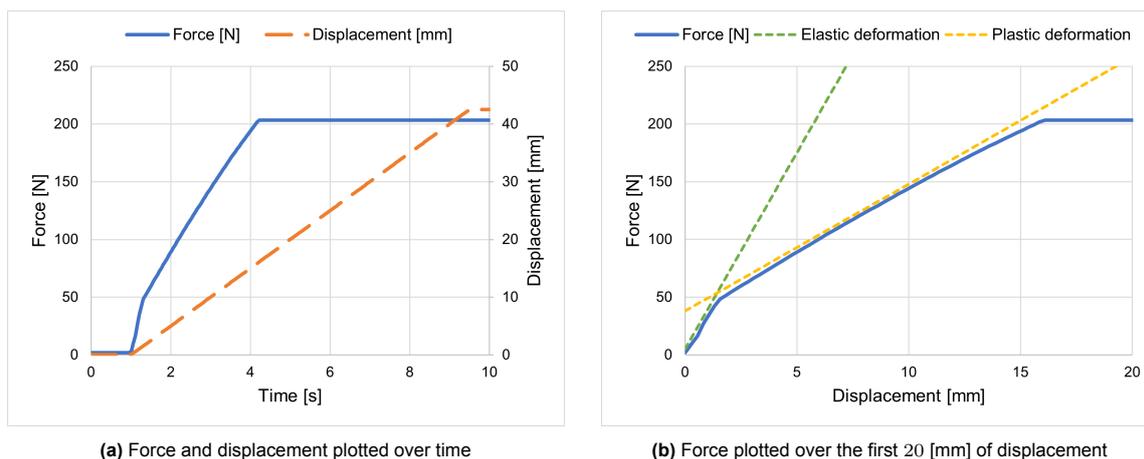
Figure 13.3: The result of the structural strength test, plotted over time and displacement. The dashed trendlines indicate the elastic and plastic deformation; the transition occurs at 50 [N].

The plastic deformation is shown in Figure 13.4a. The prototype fails at the predicted spot, the first LED hole in the loop, as shown in Figure 13.4b. The prototype is still watertight after it has deformed 40 [mm]. The upright and the section that houses the camera are still intact. This part of the aluminium prototype can sustain over 200 [N].

(a) Plastic deformation of the prototype

(b) Close-up of the location of failure
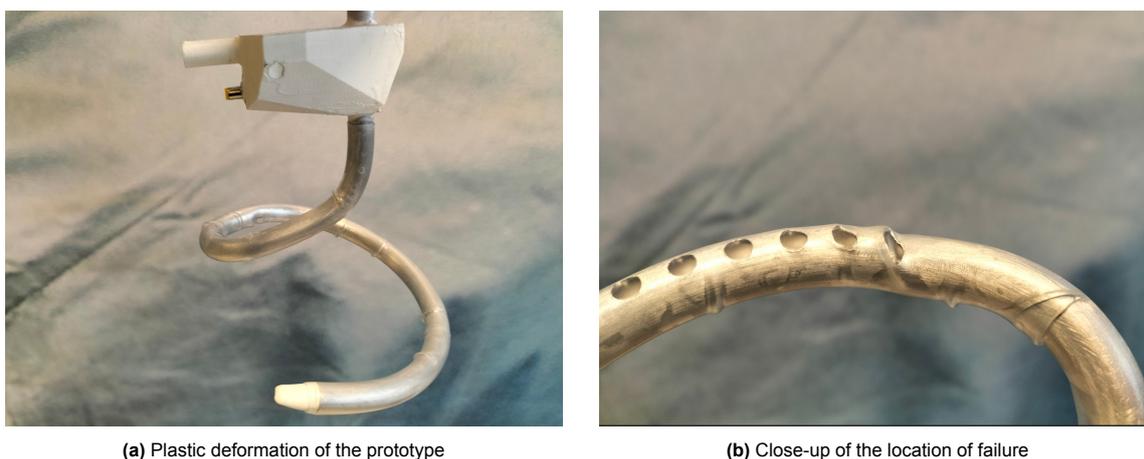
Figure 13.4: The shape of the prototype after the structural strength test.

Discussion

The force-displacement curve gives an indication of the structural strength of the lifting device. The prototype starts to fail at around 50 [N] because the slope of the force-displacement graph changes significantly here. The loop of the prototype does not fully support the artificial skin anymore and the section with the camera is the only part that still pulls on the artificial skin. This can be seen in Figure 13.5, where the skin tension around the camera section is higher than at the tip of the loop.

The change of slope, and its occurrence at a deformation of 1.5 [mm], strongly suggest that this point of the graph marks the transition from elastic to plastic deformation. However, part of the 1.5 [mm] deformation may already be plastic deformation. The ultimate strength of aluminium 6060-T66 is 220 [MPa], a 30% increase over the yield strength. This means that the prototype can sustain at least 40 [N], accounting for possible plastic deformation.

The aluminium prototype was designed to sustain 31 [N]. The structural test showed that it can withstand at least 40 [N] of load from a simulated abdominal wall, exceeding the design load by 30%. The deformation measurements are less reliable because it is a combination of prototype deformation and artificial skin stretch.
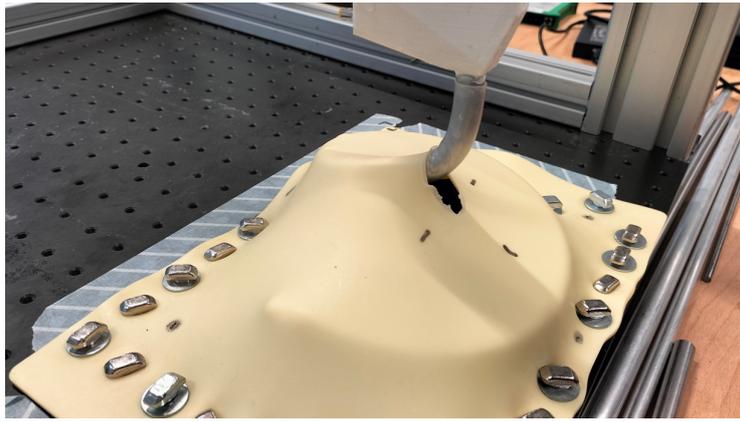
Figure 13.5: The prototype during the test, at a deformation of 25 [mm].

Based on these findings, it is recommended to continue the use of the Fusion 360 FEA tool for further development. Using a safety factor of 2, the aluminium prototype proved that the FEA predictions are accurate with a safe margin. Extrapolation of the prototype's result indicates that a stainless steel (yield strength < 690 [MPa]) lifting device should be able to sustain a load of 140 [N]. However, the structural strength of a future development lifting device should still be verified on a similar test setup.

Limitations of methods
The results from this test are based on a single run, making it susceptible to variability. The reason is that every test destroys a semi-finished prototype which costs 8 hours to produce. For future structural strength tests, it is therefore recommended to start with multiple runs of non-destructive stress tests before performing this test.

The used setup gives an estimate of the failure load of the complete prototype. However, it does not measure its deformation (due to the contribution from the skin) or local strain. For future tests, it is recommended to equip the prototype with strain gauges to determine the failure load more accurately.

During the test, the linear stage had a velocity of 5 [mm/s]. However, the prototype deforms less than 2 [mm] before failure, and as such failure happened within 0.4 [s]. For future tests, it is recommended to set the linear stage to a much lower velocity of < 1 [mm/s] to more accurately measure the forces on the lifting device during failure.

The FEA results from Figure 13.2 do not completely replicate the structural strength test. FEA assumes all parts of the prototype are loaded equally, FEA does not account for the polyolefin heat shrink, and FEA assumes all parts are perfectly bonded. The results from this test showed that these inaccuracies are still within the limits of the applied safety factor.

Conclusion
The prototype exceeds the material-adjusted design load by 30%. It is therefore recommended to continue the use of Fusion 360 FEA for future design of the lifting device. However, FEA results always need to be verified on a force-displacement setup. The setup used in this experiment can be improved by adding local strain gauges and reducing the velocity of the linear stage.

13.3. Additional tests
This section describes five small tests to verify requirements C1, D1, R1, D2, and M1. The tests quantify the performance of the aluminium prototype on these five aspects. Based on the performance, several recommendations are made for future development.

Cost
This test assesses the cost per lifting device. Cost-effectiveness is the second design driver of this design. Keeping costs low is vital for the potential impact of the device because that makes it accessible to healthcare facilities in low-resource settings and enables wider adoption and implementation.

To get an estimate of the cost per lifting device, a simple analysis of the production cost is performed. The lifting device has no running costs. Production cost can be estimated by three main expenses: raw

materials, labour, and overhead. Overhead, such as rent and utility expenses, is ignored in this analysis. The cost of materials and the labour time are listed in Table 13.1 per component.

The data for cost and labour time per component follow from the production of several aluminium prototypes. The final design of the lifting device requires some different parts, listed in italics. These numbers are estimates based on commercially available parts. A fully functional aluminium prototype costs approximately €30 and 8 hours of manual labour to produce. A lifting device in final design specification costs approximately €60 and 10 hours of manual labour to produce.

The production costs of the lifting device thus heavily depend on the hourly labour cost. The Federal Statistical Office of Germany estimates[1] that the hourly labour cost is approximately €41.00 ($44.89) in The Netherlands and €1.50 ($1.69) in India. As a result, the basic cost of production per lifting device is €460 in The Netherlands and €75 in India.

This initial estimate shows the importance of local production. The maximum purchase price per lifting device is €250. The basic cost of production is 30% of the purchase price if production is moved to India, providing a good starting point for the commercialisation of the lifting device. However, production in the Netherlands would make the lifting device too expensive.

This simple cost analysis has left out many factors. Production overhead costs and tooling costs are not considered. Tooling costs may be significant because several custom parts are required and the production run may be small (< 100). Furthermore, production costs make up only part of the cost per unit. Operational expenses, regulatory environment, product lifecycle (not assessed in this thesis), logistics, and other expenses all add to the cost of the lifting device.

To conclude, a rough estimate of the production costs indicates that the lifting device can be cost-effective. For more accurate estimates it is recommended to intensify collaboration with local biomedical engineers for future development of the lifting device.

Table 13.1: Overview of the weight and cost of the lifting device per component. The data is based on the aluminium prototype. Differences between the prototype and the final design are indicated in italics.

Part	Weight [g]	Material cost	Manual labour time [min]
Aluminium tubular frame	56	€ 2,00	240
Stainless steel tubular frame	*160*	*€ 15,00*	*240*
Aluminium RAIS joint	25	€ 0,60	120
Stainless steel RAIS joint	*75*	*€ 4,00*	*120*
SLA-printed endcap	2	€ 0,25	15
Machined endcap	*12*	*€ 0,35*	*45*
PLA housing	50	€ 1,00	30
Nylon housing	*45*	*€ 5,00*	*30*
M6 bolt & nut	5	€ 0,40	—
M3 bolt	2	€ 0,15	—
Polyolefin heat shrink	16	€ 2,60	15
Camera module	5	€ 18,80	15
LED strip (commercial)	20	€ 2,75	45
LED circuit	*50*	*€ 10,00*	*120*
USB cable	10	€ 2,30	—
Total	**191 / *380***	**€ 31 / *€ 59***	**480 / *585***

Weight

This test assesses the weight of the lifting device, which may weigh no more than 1 [kg]. Measurements show that a fully functional aluminium prototype weighs approximately 190 [g], which confirms the breakdown in Table 13.1. The table also lists an expected weight of 380 [g] for the stainless steel lifting device. It can thus be concluded that the weight of the lifting device is well below the 1 [kg] limit.

---

[1]www.destatis.de/EN/Themes/Countries-Regions/International-Statistics/Data-Topic/Tables/BasicData_LaborCosts.html

Waterproofness

This test assesses the waterproofness of the lifting device, which should have an IP67 rating. This rating stipulates that the lifting device should be submerged in water for 30 minutes with its highest point at least 150 [mm] below the surface. However, due to logistical restrictions, no pool of water with sufficient depth was available.

Instead, the prototype was submerged in water approximately 300 [mm] below the surface for three runs of 2 hours. The waterproofness was assessed visually and by weighing it after every submersion. The prototype had polyolefin heat shrink applied to the tubular frame, and the housing was sealed using Den Braven Hybridseal. These two measures proved sufficient to make the prototype waterproof. Moreover, the prototype appears waterproof even after the tubular frame has failed (see Figure 13.4a).

This test does not confirm that the prototype has an IP67 rating. However, the waterproofness rating of the prototype is not relevant since the current waterproofness measures are not recommended for future development (see Findings in Section 11.2).

Insertion diameter

This test assesses the insertion diameter of the lifting device. The cross-section of the lifting device may not exceed a 12 [mm] circle at any point that will be inserted into the abdominopelvic cavity, which was verified by measuring the diameter of the prototype with a digital calliper.

Measurements showed that the majority of the prototype has a diameter of 12.4 [mm] and 12.5 [mm] at the small radius bends. This diameter is because the polyolefin heat shrink is applied on a 12 [mm] aluminium tube. A decrease in diameter can be realized by using a different waterproofing method or by decreasing the diameter of the tube. The diameter of the tube can be decreased by at least 2 [mm] at the loop part, but the camera section is more difficult due to the space required for the camera sensor. It is therefore recommended to find alternatives for the polyolefin heat shrink.

Compatibility

This test aims to verify that the lifting device is compatible with the RAIS connector arm. Professor P.R. Culmer, responsible for the design of RAIS [38], kindly shared the CAD drawings of the RAIS connector arm. Based on these drawings, parts of the RAIS connector arm were 3D-printed to the exact dimensions of the metal variant. The 3D-printed parts were used to perform a simple fitting test.

The results are shown in Figure 13.6. The machined RAIS joint fits snugly in the retractor arm, but the sides are wedged slightly. The hexagonal sides of the joint can be used to set the orientation of the lifting device in increments of $36°$. For future production, it is recommended to decrease the width of the machined RAIS joint to 19.8 [mm] such that it fits without wedging.

The compatibility of this lifting device with the RAIS system was also confirmed by Deborah Maufi, CEO of Loresa, a health venture that works on commercializing the RAIS system.

(a) A prototype connected to a 3D-printed retractor arm   **(b)** Closeup of the connection
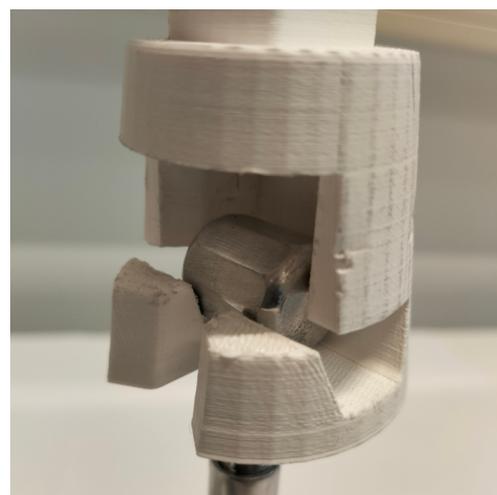
Figure 13.6: Verification of the lifting device's compatibility with the RAIS retractor arm.

14

Validation: User test

14.1. Evaluation by Dr Gnanaraj

Dr Jesudian Gnanaraj (also referred to as J. Gnanaraj or Dr Gnanaraj) is an accomplished and expert GILLS surgeon in low-resource settings. He has been working in rural India for three decades and has performed, or helped to perform, thousands of surgical procedures. Furthermore, he has helped to start more than 30 hospitals with MIS capabilities.

Dr Gnanaraj is currently president of the Association of Rural Surgeons of India (ARSI) and the joint secretary of the International Federation of Rural Surgeons (IFRS), and as such is at the forefront of advancing surgical practices in underserved regions. He is also an adjunct professor in the Electronics and Instrumentation Department of Karunya University. As the Editor of the Rural Surgery Journal of the Association of Rural Surgeons of India, Dr Gnanaraj continues to shape the discourse in his field with 45 publications in national and international journals.

Dr Gnanaraj visited the Delft University of Technology at the end of November 2023. As part of this visit, pictured in Figure 14.1, he tested the lifting device prototype on requirement E1 and several others. The following section summarizes his findings about the device.


Figure 14.1: Dr Gnanaraj evaluating the lifting device prototype on a simulated GILLS setup.

Discussion
The overall conclusion from Dr Gnanaraj was that the lifting device prototype works much better than expected. Sceptical at first, but after trying out the prototype on a test setup Dr Gnanaraj is now convinced of the potential of this technology. This discussion represents the words from Dr Gnanaraj about the lifting device and is published with his approval.

The two test setups are shown in Figure 14.2. Both are based on a laparoscopic box trainer with a transparent plastic sheet as an abdominal wall. The lift device is inserted through a 12 [mm] incision. The plastic sheet is covered by a dark towel such that the inside of the box trainer is devoid of outside light. The difference between the test setups is the model on the inside. In the first setup, the model is a printed AI-generated drawing of the intestines. This was used to evaluate the colour representation of the camera. In the second test setup, the model is a 3D-printed model of the intestines and uterus, used to evaluate depth perception. In both test setups, the lifting device prototype was compared to the low-cost laparoscope that is currently used in rural India [34].

(a) Test setup 1, based on an AI-generated drawing of the intestines   (b) Test setup 2, based on a 3D-printed organ model
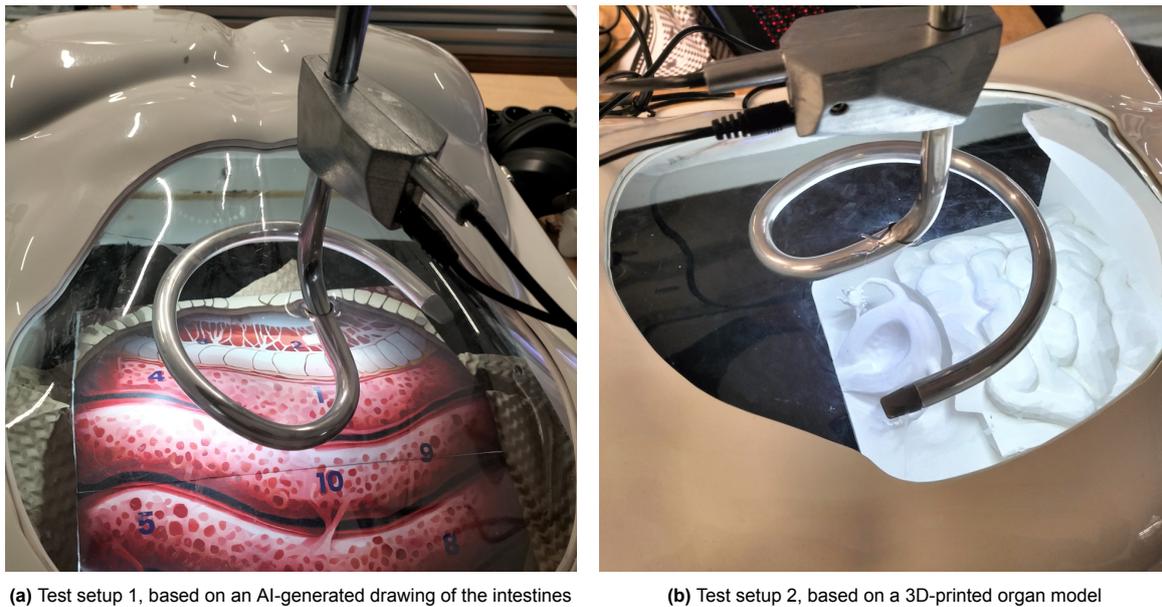
Figure 14.2: The two test setups for the visit of Dr Gnanaraj.

The biggest improvement of this lifting device over current imaging systems is its integrated camera. The wide-angle camera offers a very good overview of the complete surgical area in high resolution, and there are no problems with depth perception or distortions at the side of the image. Digital zoom is an essential function as it allows close-up inspection of tissue without physically moving the camera. The time delay is rated as excellent because it is negligible, and as a result, the imaging does not suffer from vibrations.

Due to the high quality of imaging and the possibility of digital zoom, the single viewpoint is more than sufficient for BTL and many other types of laparoscopic procedures: almost all laparoscopic procedures would be possible with just this lifting device.

The fact that the currently used laparoscopes could be replaced by this lifting device for many procedures is a big step forward for rural surgeons. Currently, an assistant holds the laparoscope while the surgeon uses both hands to control surgical instruments. However, assistants in low-resource settings are often untrained and thus incorrectly orient and position the laparoscope (for this reason, a laparoscope-holder is simultaneously being developed at the Delft University of Technology). In contrast, this lifting device can be set at a specific orientation, and the surgeon will have both hands free for the procedure. Dr Gnanaraj even reckons that this is the biggest advantage of this lifting device over the current setup.

Another advantage lies in a superior light output. The ring of LEDs provides much more light than currently used laparoscopes. Additionally, the camera sensor is larger than that of currently used

laparoscopes. It is therefore more easily saturated, meaning the complete surgical field is correctly exposed. Almost no shadows or flares are present due to the light coming from all directions. In contrast, laparoscopes emit their light from a single point and therefore it is necessary to "move around" the target location to get a view without shadows or flares.

The dimensional design of this lifting device is the primary area of improvement. Dr Gnanaraj advocates for a frame with a different shape and dimensions such that the lifting device is also compatible with single-incision laparoscopic surgery (SILS).

SILS is an MIS technique that utilizes a single abdominal incision of 15-20 [mm] near the umbilicus for all instruments. These instruments are placed underneath the entrance point of the lifting device, as shown in Figure 14.3a for the currently used lifting devices STAAN or RAIS.

SILS is not possible with the current dimensional design. The loop of the lifting device should be above the surgical field, to create space for all the instruments. However, Figure 14.3b shows that the loop of the lifting device and the tip of the instrument are on opposite sides. The camera also looks in the opposite direction compared to the instrument. Furthermore, the camera is partially or even completely blocked by the instrument.

(a) Orientation for current lifting devices   **(b)** Orientation for the prototype lifting device
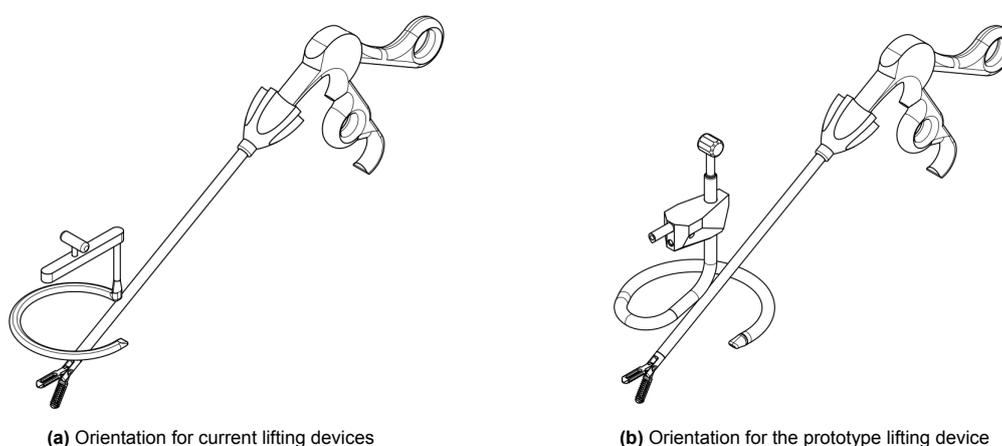
Figure 14.3: Drawing of the orientation of instruments with respect to the lifting device for SILS.

The loop of the lifting device should also have a smaller radius. Before inserting the lifting device, surgeons use their fingers to sweep the anterior abdominal wall to rule out adhesions. The 70 [mm] loop radius is too large for most Indian surgeons to check by hand; 50 [mm] is the maximum. The resulting decrease in theoretical operational volume is no issue in practice. For use in SILS, the loop of the lifting device should also be twisted. The twist eases the insertion of the lifting device and creates the operational volume with minimum interference for other instruments.

The diameter of the loop cross-section should also be reduced if possible. The current 12 [mm] is not needed in the loop part, which only houses the LED strip. A reduction to 8 [mm] will reduce the internal volume of the loop by more than 50%.

The RAIS connector is set at a good height from the loop, and its central placement helps with the positioning of the lifting device. The electronics housing may be closer to the loop, i.e. a clearance distance of less than 65 [mm] suffices. The strength of the housing seems good but has to be verified. A longer, single USB cable is preferred over the current configuration.

Recommendations

The result of this evaluation by Dr Gnanaraj is several recommendations. The concept of integrating an imaging system with the lifting device, at this price point, has the potential to improve surgical outcomes and increase access to specialized medical care in LMICs. Therefore, this lifting device must move from the prototyping phase to production such that it does not remain just a good concept.

The focus of future development should be on collaborating with local surgeons and biomedical engineers. Presentation of pre-production models of the lifting device at congresses for rural surgeons

can introduce them to the concept. Biomedical engineers from India can start working on production processes with input from the current project and additional research.

Adapting the shape of the lifting device such that it can also be used for SILS would increase its usability and applicability. Furthermore, the loop should have a smaller radius and preferably a smaller cross-section diameter.

At least three additional tests are required to verify the performance of the lifting device. The effect of smoke and fog in the operational volume on image quality, the surface temperature of the lifting device during 8 hours in a confined space, and the structural strength of the handle all need to be investigated. If the shape of the lifting device is altered, its structural strength has to be verified again.

14.2. Remarks from the ECTMIH 2023

The prototype of this lifting device was showcased at the European Congress on Tropical Medicine and International Health (ECTMIH) 2023 in Utrecht. Five different surgeons with experience in low-resource settings evaluated the lifting device on its potential for use in laparoscopic procedures. Their comments are summarized below.

The surgeons were unanimously appreciative of the all-in-one capabilities of the lifting device. One device that creates the operational volume and provides imaging with a high-quality camera and very large (for laparoscopic terms) light source is a unique concept. The price point makes it perfectly suited for low-resource settings, and one surgeon commented he would even use the device for diagnostic laparoscopy in HICs.

The camera technology was praised for being comparable to state-of-the-art laparoscopes in HICs. The images are sharp, offer a wide view, and have no noticeable time delay. However, the fact that this lifting device could not be sterilized was deemed a drawback. One surgeon also questioned the rigidity of the heat shrink sealing during intensive use.

Finally, the device removes the need for surgical assistants to hold the laparoscope. This gives the surgeons more autonomy as they can perform procedures completely solo. All surgeons were eager to test a future pre-production model of the lifting device on a simulated setup.

<div align="right">

15

</div>

<div align="right">

Discussion

</div>

The aim of this project was to design, build, and test a context-driven AWL device with an integrated imaging system for GILLS BTL procedures in low-resource settings. It should substitute for both the current lifting device and the currently used laparoscopes. The design should be cost-effective, robust, user-friendly, and compatible with the RAIS mechanical retractors.

15.1. Discussion

The main result of this project is the design of a loop-shaped lifting device with an integrated imaging system and lighting system. The design was translated into two fully functional prototypes. The final design is shown in Chapter 6 and explained in the subsequent chapters, and the prototypes are shown in Chapter 11. Its performance is evaluated using 9 verification tests and validated by 2 user tests. The results are summarized and evaluated per subsystem below.

Electronic system

The used imaging system, an OmniVision 5693 CMOS wide-view camera module, outperforms the benchmark of laparoscopic imaging, the Olympus OTV-S7 laparoscope, on all of the tested metrics: field of view, sharpness, noise, colour accuracy, and distortion. Its image quality is close to that of the current state-of-the-art Stryker AIM 4K laparoscope and costs just €20. It is therefore highly recommended to continue using this camera module during further development. The image quality factor test has insufficient reliability, but the results were confirmed by user validation.

The performance of the OV5693 camera sensor was not tested in surgical conditions such as excessive blood, smoke, or fog. The test on colour accuracy revealed that the OV5693 camera module is sensitive to red blooming, where the whole image is tinted to the dominant colour red. Furthermore, the effect of smoke and fog on image quality relative to laparoscopic systems should be tested.

The position and orientation of the camera on the lifting device were rated as excellent in the user test. The wide-view high-quality imaging of the camera offers a very good overview of the complete surgical area. Depth perception is excellent and time delay negligible. Combined with digital zoom, the traditional laparoscope becomes redundant for most GILLS procedures. This lifting device can be set at a specific orientation and the surgeon will have both hands free for the procedure, without needing an assistant for imaging. Dr Gnanaraj described this as the biggest benefit of this lifting device.

Further research is needed into the imaging software. The default Windows camera app gives good-quality imaging but does not allow for digital zoom and other functions. For most GILLS procedures, digital zoom is necessary to replace the laparoscope, and it should be controlled using buttons on the device or a foot pedal. Imaging software like Resolume Avenue enhances imaging quality and allows for such functionality. However, it is expensive and difficult to work with for novices.

The lighting system used for prototyping, a pre-assembled 12 [V] LED strip, does not provide enough light to meet the requirements, has an asymmetric illumination distribution, and generates too much

heat. It also requires an additional USB-A cable. However, its illumination was rated as superior to any current laparoscopic imaging system in low-resource settings by Dr Gnanaraj.

For future development, a custom LED circuit is recommended to increase light intensity and reduce heat generation. Insulation may be required for temperature management. Furthermore, the power- and data input of the lighting system needs to be combined with the camera module into a single USB-A cable of approximately 3 [m]. The custom LED circuit should be designed such that the individual LED chips have the same orientation as the holes (toward the ground plane), instead of a $90°$ angle like the LED strip, to get a higher efficiency. The loop may need an asymmetric distribution of LED holes to provide a symmetric illumination distribution.

Dimensions

The shape of the lifting device is based on methods from research to ensure a sufficiently large operational volume and easy insertion. The camera sensor is at an angle such that it centres on the uterus. The shape can be bent from a single piece of 12x1 [mm] tube.

However, Dr Gnanaraj indicated he would prefer a different shape to allow for SILS. The radius and cross-section diameter of the loop should be smaller for easier finger clearance. The resulting loss of operational volume is no issue in clinical practice. For example, the currently used STAAN ring has a radius of 45 [mm]. It also utilizes loop twist for easier insertion, something Dr Gnanaraj would like to see on this lifting device too. Two examples of SILS-compatible lifting device shapes, developed in collaboration with Dr Gnanaraj, are shown in Figure 15.1.
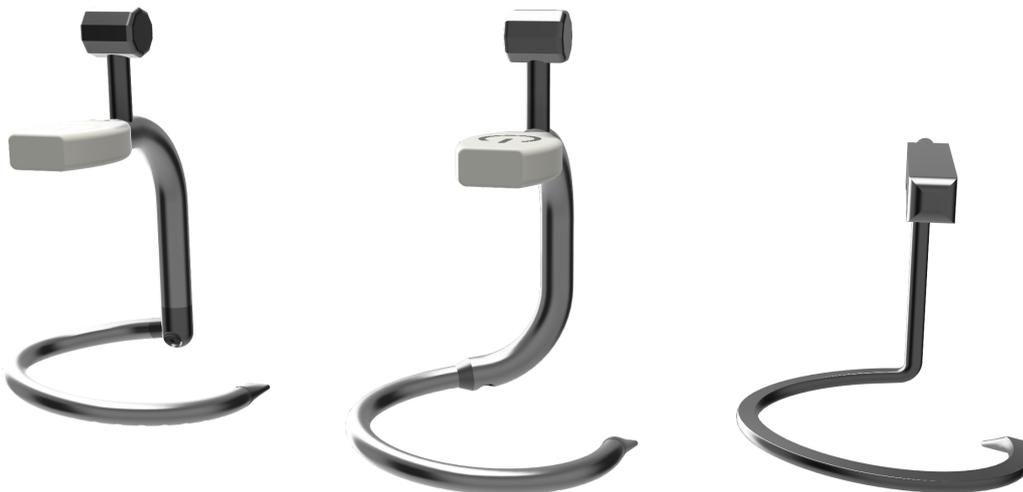
Figure 15.1: Two example configurations of the lifting device that are compatible with SILS. The lifting device on the right is the currently used STAAN. Both example configurations use the OV5693 camera module.

The input from local end users thus conflicted with recent research [39]. However, the mismatch in dimensional design was also caused by inconsistent use of input data, not always tailored to the patient population; Indian females. For example, the mean transverse radius used for dimensioning does not represent the average for Indian females. This data is difficult to find in literature and only indirect measurements are available, such as studies into the dimensions of the abdominal aorta [127] or the abdominal muscles [128].

Another example is the tilt angle, for which an average value of $15°$ was used. However, with the RAIS connector joint, the tilt angle is either $0°$ or $\pm36°$, and never the average $18°$ (although the arm can also tilt a few degrees).

It is therefore recommended to review the dimensional design of the lifting device using multiple rural GILLS surgeons. Their experience with lifting devices, like the STAAN, trumps methods and data from research. Consensus about the need for a SILS-compatible shape and the outer dimensions should be the priority.

Structure & Materials

The structural design of the lifting device is based on FEA in Fusion 360. The limiting factor to its structural strength is the diameter and amount of holes in the loop for the lighting system. The distribution of holes was optimised for the maximum area for which the FEA safety factor remained 2.

A structural strength test showed that the strength of the aluminium prototype exceeds the material-adjusted design load by 30%. The setup used a section of artificial skin to clamp the prototype to mimic the force distribution during GILLS procedures. It is therefore recommended to continue the use of Fusion 360 FEA for future design of the lifting device. FEA results always need to be verified because they do not perfectly represent all loads and failure phenomena. The effect of fall damage on the lifting device has not been tested but should be verified in future development.

The connector is machined from the same metal as the frame and fits with the RAIS retractor arm. All additional parts of the lifting device are also machined from the same metal, and the housing is 3D printed from Nylon. The total weight of the device is less than the maximum allowed 1 [kg] at an estimated 0.38 [kg]. This is an estimate because the prototype used different materials than the final design.

The type of material for the screws in the housing has not been researched. Furthermore, the resistance to cleaning chemicals was not tested at all. It is important for further development to verify chemical resistance for repeated cleaning cycles.

The prototype is sealed using polyolefin heat shrink and sealant. This keeps the device waterproof, even during structural failure, but is not sufficient for use in clinical practice. The heat shrink is susceptible to tears, difficult to apply without wrinkles, and increases the insertion diameter beyond 12 [mm]. Furthermore, it negates the use of stainless steel which in itself is a tough and chemical resistant material. Other sealing options should be considered for further development.

Production & Assembly

The production of an aluminium prototype proved that all major components of the design can be realized using traditional machining techniques and 3D printing. However, the load-bearing tubular frame was created from aluminium 6060-T66, a material known for its ease of use. The intended material, stainless steel 17-4 PH, theoretically also has good machinability in its annealed condition (similar to 316L stainless steel) but this has not been tested.

The production of other parts using turning, milling, and 3D printing is straightforward but assembly of these parts requires training. The camera sensor has to be inserted first and carefully guided into position using small (< 2 [mm] diameter) slotted screwdrivers. A camera sensor holder was designed but not used for the prototype because it did not fit, and instead the camera sensor was glued in place. Next, a metal guide wire is inserted through the frame and then used to pull the LED strip in position. The LED strip can be glued to the inner radius of the loop. The housing fitted well with all components but the process of assembly should be simplified.

A simple cost analysis showed that the base production cost of a single lifting device equals approximately €75, accounting for both material costs (Dutch rates) and labour costs (Indian rates). However, this analysis did not consider all costs, such as the cost of tooling. For example, the tubular frame of the prototype was bent using a compression bend die but rotary draw bending is likely required for stainless steel. Rotary draw bending requires expensive custom bending jigs and a different sequence of bends. Further research is therefore necessary to determine if rotary draw bending is the best option for the production of the frame.

To summarize, the production process for the final design has not been completely verified. It requires additional machining techniques which can be expensive. Collaboration with local biomedical engineers is recommended to design a feasible and cost-effective production process. The positioning and installation of the electronic components also need improvement such that it is easier and reversible, allowing for quick repairs of the lifting device.

15.2. Limitations

It is important to acknowledge the limitations of this project. Although the aim of the project specifies a lifting device for GILLS BTL procedures, the final design of this lifting device is not suited for use in clinical practice. The resulting prototype works well as a study model and for small user tests on simulator models. However, it is not suited for production and subsequent use on human patients.

The development of the prototype has been done in collaboration with two local end-users, which was not sufficient. The collaboration should be with multiple local end-users to get more diverse and balanced feedback throughout the design process. For example, Dr Gnanaraj noted only near the end of the design process that he did not like the shape and size of the device. Such crucial aspects should have been discussed earlier in the process to prevent the need for extensive redesigns.

An extra fully functional aluminium prototype has been produced specifically to gather more feedback. It has been sent to Dr Gnanaraj for further evaluation by rural surgeons in India and multiple countries in Africa. For future development, it is important to form a group of rural surgeons as a sounding board for the design process.

The performance of the prototype's electronic system was measured with several tests. However, these tests were mostly unit tests of the electronics and no integrated system tests. For example, the effect of the protective camera lens on image quality has not been tested. Neither has the effect of lighting on image quality been tested, even though these effects can be significant. The results of these tests could be used to determine how well the proposed lighting system works with the selected camera module.

The consequences of failures in the electronic system were also not investigated nor tested. The electrical components were placed inside the metal frame of the lifting device without insulation, and it is made from metals that easily conduct electricity and heat. If leakage of current, LED burnout, or other failures occur during procedures they may have a detrimental effect on patients.

Interviews with multiple rural surgeons are required to determine if it is necessary to change the shape of the lifting device such that it is suited for SILS. What is certain is that the 70 [mm] radius of the loop is too large by at least 30%. However, the minimum possible radius for this shape with a $12x1$ [mm] tube is only 60 [mm]. The 12 [mm] tube diameter in turn is necessary to fit the camera sensor. A new shape is therefore required with a varying cross-section diameter.

The new shape and possibly varying cross-section diameter require investigations into new production methods and new materials. The use of 17-4PH stainless steel and bending as the main machining process were selected early in the design process, thereby influencing many design choices. For future development, it is recommended to review this design while keeping options open for material selection and production processes.

The current production process was not tested using the intended materials. However, preliminary calculations showed that rotary draw bending could become quite expensive due to the need for customs dies. The effect of work hardening on the selected stainless steel 17-4 PH was also not considered. Similarly, no test prints have been made using Nylon filament. The nylon filament is more flexible than PLA. The effect of this flexibility on the overall stiffness of the electronics' housing was not investigated.

The waterproof sealing based on polyolefin heat shrink is a weak point of this design, as mentioned before. The polyolefin heat shrink is unsuited for clinical use. Other options need to be investigated such as custom covers per hole or a clear infill resin. A slotted loop design was tried as well but quickly discarded because its reduced torsional stiffness decreased structural strength by 90%. Any proposed solution should be verified using multiple cleaning cycles with chemicals such as Cidex.

The degradation of components has not also been investigated. The lifetime of the device determines its potential and cost-effectiveness. It should therefore be considered for future development.

Finally, the proposed design did not account for problem statements 4 and 5 from Chapter 2. The required adaptability to patients of different weights and lengths has not been verified. Neither has the tip of the lifting device been verified on its potential for causing trauma.

15.3. Recommendations

The concept of a lifting device with an integrated camera system has the potential to improve access to GILLS procedures in low-resource settings. It is therefore strongly recommended to continue development of this lifting device focussed on a pre-production prototype. This next stage of development should be done in close collaboration with multiple rural surgeons and local biomedical engineers.

The selected camera module is the key technology of this lifting device because it provides state-of-the-art imaging at an unmatched price point. Its history as a smartphone camera means that it is mass-produced and thus widely available. If new sensors appear on the market in the future, they can be swapped in easily because of the industry-standard dimensioning. Further research is needed into intuitive, affordable imaging software that allows for digital zoom.

Three focus points have been identified for the future development of this lifting device. The first is the loop part of the lifting device. The design presented in this project can be improved by finding consensus among rural surgeons about the need for SILS compatibility. The shape and size can be adjusted accordingly, also accounting for the diverse patient population. Furthermore, the selection of materials and subsequent production processes need additional research and collaboration with local engineers. The structural strength of the resulting design can be verified using the test setup presented in this project.

The second focus point is a new lighting system. It should output more light, be distributed more evenly, and generate less heat than the pre-assembled strips used for prototyping. The lifting device should not heat up beyond $41°$ [C] when operated in a closed, humid, $37°$ [C] environment for up to 8 hours. Temperature management has not been considered in this project but should be designed for in future iterations.

The third focus point is the waterproofness of the device. The current production techniques to make the prototype waterproof have poor repeatability, are irreversible, and have low reliability. New waterproofness techniques should also be tested on chemical resistance. Autoclave compatibility would enhance the applicability of the lifting device but is not critical for its implementation in low-resource rural hospitals.

16

Conclusion

This study presents the design, production, and evaluation of a novel lifting device with an integrated imaging system. The aim was to create a cost-effective, robust, and user-friendly device that could substitute for both the current lifting device and currently used laparoscopes during BTL procedures in Indian rural hospitals. The design is based on methods from literature and input from local end-users. It consists of a custom-shaped stainless steel hook housing an imaging system created from commercially available parts. It is not ready for clinical use, but several aluminium prototypes proved the potential of this novel concept. Specifically, the performance of the imaging system received excellent feedback from expert GILLs surgeon J. Gnanaraj and visiting surgeons at the ECTMIH2023, a conclusion supported by quantitative verification tests. Its applicability reaches far beyond BTL procedures, conceivably making the traditional laparoscope redundant for many GILLS procedures. Furthermore, verification of the structural design showed that the lifting device can sustain a research-based maximum load of 140 [N] and weighs less than 0.5 [kg]. The enthusiasm created by the prototypes was such that local surgeons and biomedical engineers already initiated discussions about a production version. Such collaboration is essential for the further development of this lifting device. The three main technological focus points should be the shape, size, and material of the lifting device, its lighting system, and its resistance to cleaning processes before clinical trials can be considered. However, it is also advised to start researching contextual and regulatory factors in the local healthcare systems of target markets. Acquisition, training and maintenance of the lifting device all require context-specific consideration. This study merely demonstrated the feasibility of the technology, but it has generated incentives and momentum to work towards the successful implementation of the lifting device in hospitals in low-resource settings worldwide.

References

[1] R M Oosting et al. "Roadmap for design of surgical equipment for safe surgery worldwide". In: *2018 IEEE Global Humanitarian Technology Conference (GHTC)* (2018).

[2] G S Litynski. "Profiles in laparoscopy: Mouret, Dubois, and Perissat: the laparoscopic break-through in Europe (1987-1988)." In: *JSLS: Journal of the Society of Laparoendoscopic Surgeons* 3 (2 1999), pp. 163–7.

[3] Trishul Kapoor et al. "Cost Analysis and Supply Utilization of Laparoscopic Cholecystectomy." In: *Minimally invasive surgery* 2018 (2018), p. 7838103.

[4] William C. Meyers. "A Prospective Analysis of 1518 Laparoscopic Cholecystectomies". In: *New England Journal of Medicine* 324 (16 Apr. 1991), pp. 1073–1078.

[5] Ninh T. Nguyen et al. "Laparoscopic Versus Open Gastric Bypass: A Randomized Study of Outcomes, Quality of Life, and Costs". In: *Annals of Surgery* 234 (3 Sept. 2001), pp. 279–291.

[6] J. Esteban Varela, Samuel E. Wilson, and Ninh T. Nguyen. "Laparoscopic surgery significantly reduces surgical-site infections compared with open surgery". In: *Surgical Endoscopy* 24 (2 June 2010), pp. 270–276.

[7] Stefan Sauerland, Thomas Jaschinski, and Edmund AM Neugebauer. "Laparoscopic versus open surgery for suspected appendicitis". In: *Cochrane Database of Systematic Reviews* 11 (10 Oct. 2010).

[8] C. Clay Cothren et al. "Can we afford to do laparoscopic appendectomy in an academic hospital?" In: *The American Journal of Surgery* 190 (6 Dec. 2005), pp. 973–977.

[9] E. Patil and J. T. Jensen. "Update on permanent contraception options for women". In: *Current Opinion in Obstetrics & Gynecology* 27 (6 2015), pp. 465–470.

[10] M. A. Barone et al. "Safety of tubal ligation by minilaparotomy provided by clinical officers versus assistant medical officers: study protocol for a noninferiority randomized controlled trial in Tanzanian women". In: *Trials* 18 (1 2017).

[11] American College of Obstetricians and Gynaecologists Committee on Practice Bulletins - Gynecology. "ACOG Practice Bulletin No. 208: Benefits and Risks of Sterilization." In: *Obstetrics and gynecology* 133 (3 Mar. 2019), e194–e207.

[12] H B Peterson et al. "The risk of pregnancy after tubal sterilization: findings from the U.S. Collaborative Review of Sterilization." In: *American journal of obstetrics and gynecology* 174 (4 Apr. 1996), pp. 1161–1168.

[13] E. Westley et al. "A review of global access to emergency contraception". In: *International Journal of Gynecology & Obstetrics* 123 (1 2013), pp. 4–6.

[14] Babayemi O Olakunde et al. "Uptake of permanent contraception among women in sub-Saharan Africa: a literature review of barriers and facilitators." In: *Contraception* 99 (4 Apr. 2019), pp. 205–211.

[15] Jacqueline E Darroch et al. *Adding it up: Investing in contraception and maternal and newborn health, 2017*. Aug. 2022.

[16] Saifuddin Ahmed et al. "Maternal deaths averted by contraceptive use: an analysis of 172 countries". In: *The Lancet* 380 (9837 July 2012), pp. 111–125.

[17] Maryam Alfa-Wali and Samuel Osaghae. "Practice, training and safety of laparoscopic surgery in low and middle-income countries". In: *World Journal of Gastrointestinal Surgery* 9 (1 Jan. 2017), p. 13.

[18] A. Sarkar et al. "Assessing the barriers to postpartum tubal ligation among multiparous women". In: *Cureus* (2022).

[19] Anley Haile and Mesganaw Fantahun. "Demand for long acting and permanent contraceptive methods and associated factors among family planning service users, Batu Town, Central Ethiopia". In: *Ethiopian Medical Journal* 50 (1 2012), pp. 31–42.

[20] Tiffany E. Chao et al. "Systematic review of laparoscopic surgery in low- and middle-income countries: benefits, challenges, and strategies". In: *Surgical Endoscopy* 30 (1 Jan. 2016), pp. 1–10.

[21] The Lancet Commission on Global Surgery. "Association of Rural Surgeons of India Karad Consensus Statement on Surgical System Strengthening in Rural India". In: *Healthcare* 7 (2 June 2019), pp. 7–9.

[22] Brady Hooley et al. "Health insurance coverage in low-income and middle-income countries: progress made to date and related changes in private and public health expenditure". In: *BMJ Global Health* 7 (5 May 2022), e008722.

[23] Sanjay K. Mohanty et al. "Pattern and correlates of out-of-pocket payment (OOP) on female sterilization in India, 1990-2014". In: *BMC Women's Health* 20 (1 Jan. 2020), pp. 1–13.

[24] World Health Organization. *Guidelines for health care equipment donations*. 1997.

[25] Lora Perry and Robert Malkin. "Effectiveness of medical equipment donations to improve health systems: How much medical equipment is broken in the developing world?" In: *Medical and Biological Engineering and Computing* 49 (7 July 2011), pp. 719–722.

[26] Central Bureau of Health Intelligence (CBHI). *National Health Profile*. 2022.

[27] Pragya Singh, Kaushalendra Kumar Singh, and Pooja Singh. "Factors explaining the dominion status of female sterilization in India over the past two decades (1992-2016): A multilevel study". In: *PLoS ONE* 16 (3 Mar. 2021).

[28] Anjali Bansal, Laxmi Kant Dwivedi, and Balhasan Ali. "The trends of female sterilization in India: an age period cohort analysis approach". In: *BMC Women's Health* 22 (1 Dec. 2022), pp. 1–12.

[29] R. M. Oosting et al. "Availability, procurement, training, usage, maintenance and complications of electrosurgical units and laparoscopic equipment in 12 African countries". In: *BJS Open* 4 (2 Apr. 2020), pp. 326–331.

[30] Federico Gheza et al. "Affordable Laparoscopic Camera System (ALCS) Designed for Low- and Middle-Income Countries: A Feasibility Study". In: *World Journal of Surgery* 42 (11 Nov. 2018), pp. 3501–3507.

[31] Jeffrey R. Lukish and Jasmine Ellis-Davy. "A novel low cost minimally invasive surgical system allows for the translation of modern pediatric surgical technology to low- and middle-income nations". In: *Journal of Pediatric Surgery* 57 (6 June 2022), pp. 1099–1103.

[32] Jenna L. Mueller et al. "An Accessible Laparoscope for Surgery in Low- and Middle- Income Countries". In: *Annals of Biomedical Engineering* 49 (7 July 2021), pp. 1657–1669.

[33] Ioannis Chatzipapas et al. "Using a Mobile Smartphone to Perform Laparoscopy". In: *Journal of Minimally Invasive Gynecology* 25 (5 July 2018), pp. 912–915.

[34] Sagar Jawale, Gnanaraj Jesudian, and Prakash Agarwal. "Mini-invasive Surgery Rigid video laparoscope: a low-cost alternative to traditional diagnostic laparoscopy and laparoscopic surgery". In: (2019).

[35] N. Aruparayil et al. "Clinical effectiveness of gasless laparoscopic surgery for abdominal conditions: systematic review and meta-analysis". In: *Surgical Endoscopy* 35 (12 2021), pp. 6427–6437.

[36] Jeffrey M. Goldberg and Walter G. Maurer. "A Randomized Comparison of Gasless Laparoscopy and CO2 Pneumoperitoneum". In: *Obstetrics & Gynecology* 90 (3 Sept. 1997), pp. 416–420.

[37] Pamela L. Johnson and Karen S. Sibert. "Laparoscopy. Gasless vs. CO2 pneumoperitoneum." In: *The Journal of Reproductive Medicine* 42 (5 May 1997), pp. 255–259.

[38] M. Marriott Webb et al. "The RAIS Device for Global Surgery: Using a Participatory Design Approach to Navigate the Translational Pathway to Clinical Use". In: *IEEE Journal of Translational Engineering in Health and Medicine* 10 (2022).

[39] Aryaman Gupta et al. "KeyLoop: Mechanical Retraction of the Abdominal Wall for Gasless Laparoscopy". In: *Surgical Innovation* 29 (1 Feb. 2022), pp. 88–97.

[40] Anurag Mishra et al. "Evaluation of Gasless Laparoscopy as a Tool for Minimal Access Surgery in Low-to Middle-Income Countries: A Phase II Noninferiority Randomized Controlled Study". In: *Journal of the American College of Surgeons* 231 (5 Nov. 2020), p. 511.

[41] S. J. Neuhaus, A. Gupta, and D. I. Watson. "Helium and other alternative insufflation gases for laparoscopy: A review". In: *Surgical Endoscopy* 15 (6 2001), pp. 553–560.

[42] V. Cottin, B. Delafosse, and J. P. Viale. "Gas embolism during laparoscopy: A report of seven cases in patients with previous abdominal surgical history". In: *Surgical Endoscopy* 10 (2 1996), pp. 166–169.

[43] L. Bains et al. "Gasless laparoscopic surgery-a technique requiring multidisciplinary collaboration to improve equitable access to surgery worldwide". In: *Surgical Innovation* 30 (1 2022), pp. 131–133.

[44] Haitham Shoman et al. "Safety and efficiency of gasless laparoscopy: A systematic review protocol". In: *Systematic Reviews* 9 (1 Apr. 2020), pp. 1–6.

[45] Keisuke Araki et al. "Abdominal wall retraction during laparoscopic cholecystectomy". In: *World journal of surgery* 17 (1 Jan. 1993), pp. 105–107.

[46] Daijo Hashimoto et al. "Laparoscopic cholecystectomy: an approach without pneumoperitoneum". In: *Surgical Endoscopy* 7 (1 Jan. 1993), pp. 54–56.

[47] Naoya Ikeda et al. "Simple technique for gasless transumbilical single-incisional laparoscopic-assisted appendectomy". In: *Langenbeck's Archives of Surgery* 399 (3 Jan. 2014), pp. 359–366.

[48] Maurício V. Brun et al. "Use of a new device for gasless endosurgery in a laparoscopic diaphragmatic hernia repair ex vivo canine model: A pre-clinical study". In: *Veterinary Medicine and Science* 8 (2 Mar. 2022), pp. 460–468.

[49] L. Angelini et al. "Combination of subcutaneous abdominal wall retraction and optical trocar to minimize pneumoperitoneum-related effects and needle and trocar injuries in laparoscopic surgery". In: *Surgical endoscopy* 11 (10 1997), pp. 1006–1009.

[50] H. Tintara et al. "Simplified abdominal wall-lifting device for gasless laparoscopy". In: *International Journal of Gynecology and Obstetrics* 61 (2 May 1998), pp. 165–170.

[51] Shigeo Akira et al. "Gasless laparoscopic surgery using a new intra-abdominal fan retractor system: an experience of 500 cases". In: *Journal of Nippon Medical School = Nippon Ika Daigaku zasshi* 72 (4 Aug. 2005), pp. 213–216.

[52] Dong Bo Wu et al. "Preliminary study on the application of an umbrella-like abdominal wall-lifting device in gasless laparoscopic surgery". In: *Journal of Laparoendoscopic and Advanced Surgical Techniques* 23 (3 Mar. 2013), pp. 246–249.

[53] Jared Ostdiek and Carl Nelson. "Compliant device for abdominal wall lifting in gasless laparoscopy". In: *Journal of Medical Devices, Transactions of the ASME* 7 (2 June 2013).

[54] Dongbo Wu et al. "Spindle-like abdominal wall-lifting device in gasless laparoscopic surgery in animal experiments". In: *Minimally Invasive Therapy & Allied Technologies* 23 (6 Dec. 2014), pp. 357–360.

[55] Y. Izumi, T. Kawano, and T. Iwai. "Development and clinical application of semi-loop-shaped retractor for gasless laparoscopic surgery". In: *Surgical Endoscopy and Other Interventional Techniques* 17 (9 Sept. 2003), pp. 1488–1493.

[56] C N Gutt et al. "Systems and instruments for laparoscopic surgery without pneumoperitoneum." In: *Surgical endoscopy* 11 (8 Aug. 1997), pp. 868–74.

[57] H Nishii et al. "Laparoscopic surgery by abdominal wall lifting using original lifting bars". In: *Surgical laparoscopy & endoscopy* 7 (2 Apr. 1997), pp. 124–8.

[58] Daniel Kruschinski. "Atlas of Lift-Laparoscopy : The New Concept of Gasless Laparoscopy". In: (May 2007).

[59] Marco P. Viani et al. "Gasless laparoscopic gastrostomy". In: *Journal of laparoendoscopic surgery* 5 (4 1995), pp. 245–249.

[60] Fu Hsing Chang et al. "Laparoscopic myomectomy of large symptomatic leiomyoma using airlift gasless laparoscopy: a preliminary report". In: *Human reproduction (Oxford, England)* 11 (7 1996), pp. 1427–1432.

[61] H. Nakamura et al. "Fishing-rod-type abdominal wall lifter for gasless laparoscopic surgery". In: *Surgical endoscopy* 10 (9 1996), pp. 944–946.

[62] T. E. Udwadia et al. "Vacuum-assisted abdominal wall lift for minimal-access surgery: A porcine model study". In: *Surgical Endoscopy and Other Interventional Techniques* 19 (8 Aug. 2005), pp. 1113–1119.

[63] Keisuke Naito et al. "Development of minimally invasive lifting device using extension and flexion of pneumatic soft actuator for laparoscopic surgery". In: *2017 International Symposium on System Integration* 1 (Feb. 2018), pp. 565–570.

[64] G. Schaller, V. Engelke, and B. C. Manegold. "Mechanical augmentation of the peritoneal cavity in laparoscopic surgery — a new instrument set". In: *Minimally Invasive Therapy & Allied Technologies* 5 (1 Jan. 2009), pp. 21–24.

[65] N. Aruparayil et al. "Gasless laparoscopy in rural India-registry outcomes and evaluation of the learning curve". In: *Surgical Endoscopy* (2023). DOI: 10.1007/S00464-023-10392-4.

[66] C. Watkins et al. "Comparison of thoracic and abdominal cavity volumes during abdominal co2 insufflation and abdominal wall lift". In: *Veterinary Surgery* 42 (5 2012), pp. 607–612.

[67] D. Pizzol et al. "Laparoscopy in low-income countries: 10-year experience and systematic literature review". In: *International Journal of Environmental Research and Public Health* 18 (11 2021), p. 5796.

[68] William S. Bolton et al. "Gasless Laparoscopic Surgery for Minimally Invasive Surgery in Low-Resource Settings: Methods for Evaluating Surgical Field of View and Abdominal Wall Lift Force". In: *Surgical Innovation* 28 (4 Aug. 2021), pp. 513–515.

[69] Sean A. Pierre et al. "High Definition Laparoscopy: Objective Assessment of Performance Characteristics and Comparison with Standard Laparoscopy". In: *Liebertpub* 23 (3 Mar. 2009), pp. 523–528.

[70] G. Panta, A. Richardson, and I. C. Shaw. "Effectiveness of autoclaving in sterilizing reusable medical devices in healthcare facilities". In: *The Journal of Infection in Developing Countries* 13 (10 2019), pp. 858–864.

[71] Krishna Kumar et al. "Trends of adult height in India from 1998 to 2015: Evidence from the National Family and Health Survey". In: (2021).

[72] Asunción Álvarez and Tom Ritchey. "Applications of General Morphological Analysis From Engineering Design to Policy Analysis". In: *Acta Morphologica Generalis AMG* 4 (1 2015).

[73] T. E. Udwadia. "Diagnostic laparoscopy: A 30-year overview". In: *Surgical Endoscopy and Other Interventional Techniques* 18 (1 Jan. 2004), pp. 6–10.

[74] Rishabh Sehgal and Ronan A. Cahill. "Advanced laparoscopic surgery for colorectal disease: NOTES/NOSE or single port?" In: *Best Practice & Research Clinical Gastroenterology* 28 (1 Feb. 2014), pp. 81–96.

[75] John S. Harris. "New Product Profile Chart." In: *Chemical and Engineering News* 39 (16 Apr. 1961), pp. 110–118.

[76] Max B. Schäfer et al. "Steerable Flexible Laparoscope to Facilitate Camera Guidance During Minimally Invasive Procedures". In: *Current Directions in Biomedical Engineering* 8 (2 Aug. 2022), pp. 57–60.

[77] Dave Litwiller. "CCD vs. CMOS: Facts and Fiction". In: *Photonics spectra* 35.1 (2001), pp. 154–158.

[78] R. Tejas, Pavan Macherla, and N. Shylashree. "Image Sensor—CCD and CMOS". In: *Lecture Notes in Electrical Engineering* 887 (2023), pp. 455–484.

[79] S. Holland et al. "Fully depleted, back-illuminated charge-coupled devices fabricated on high-resistivity silicon". In: *IEEE Transactions on Electron Devices* 50 (1 2003), pp. 225–238.

[80] W. N. Ross et al. "Imaging with organic indicators and high-speed charge-coupled device cameras in neurons: some applications where these classic techniques have advantages". In: *Neurophotonics* 2 (2 2014), p. 021005.

[81] A. E. Makkey. "Design and simulation of 140 dB dynamic range and 20 uVrms readout noise CMOS image sensor". In: *Menoufia Journal of Electronic Engineering Research* 30 (2 2021), pp. 45–50.

[82] R. Roy, C. M. Lampert, and I. Stoyneva. "When dinosaurs fly: the role of firm capabilities in the 'avianization' of incumbents during disruptive technological change". In: *Strategic Entrepreneurship Journal* 12 (2 2018), pp. 261–284.

[83] Robert J. Gove. "CMOS image sensor technology advances for mobile devices". In: *High Performance Silicon Imaging: Fundamentals and Applications of CMOS and CCD Sensors* (Jan. 2020), pp. 185–240.

[84] Gordon Roberts. "The camera". In: *Mastering Photography*. London: Macmillan Education UK, 1995, pp. 22–40.

[85] Lu Yuan and Jian Sun. "High-quality image reconstruction from RAW and JPEG image pair". In: *Proceedings of the IEEE International Conference on Computer Vision* (2011), pp. 2158–2165.

[86] R. Wu, Y. Qin, and H. Hua. "Improved illumination system of laparoscopes using an aspherical lens array". In: *Biomedical Optics Express* 7 (6 2016), p. 2237.

[87] Savannah M. Alvarado et al. "Practical strategies for improving clinical photography of dark skin". In: *Journal of the American Academy of Dermatology* 86 (1 Jan. 2022), e21–e23.

[88] Blain Brown. *Motion picture and video lighting*. CRC Press, 2012, pp. 44–54.

[89] Xiaolong Liu. "Optical design of an in vivo laparoscopic lighting system". In: *Journal of Biomedical Optics* 22 (12 Dec. 2017), p. 1.

[90] Dikshya Chhetri et al. "Design and Development of Simple and Low-cost Light Source for Laparoscopic Surgery." In: *Journal of Nepal Health Research Council* 20 (2 Nov. 2022), pp. 550–554.

[91] J. J. Mundinger and K. W. Houser. "Adjustable correlated colour temperature for surgical lighting". In: *Lighting Research and Technology* 51 (2 Apr. 2019), pp. 280–290.

[92] L. Tian et al. "High-performance light-emitting diodes encapsulated with silica-filled epoxy materials". In: *ACS Applied Materials & Interfaces* 5 (18 2013), pp. 8968–8981.

[93] M. E. Raypah et al. "Variation of thermal resistance with input current and ambient temperature in low-power SMD led". In: *Microelectronics International* 35 (1 2018), pp. 1–11.

[94] S. Muthu, F. J. P. Schuurmans, and M. D. Pashley. "Red, green, and blue LEDs for white light illumination". In: *IEEE Journal of Selected Topics in Quantum Electronics* 8 (2 2002), pp. 333–338.

[95] D Raul and K Ghosh. "Performance of chip-on-board and surface-mounted high-power LED luminaires at different relative humidities and temperatures". In: *Lighting Research & Technology* 51.8 (2019), pp. 1249–1262.

[96] L. Pohl et al. "Mixed detailed and compact multi-domain modelling to describe cob leds". In: *Energies* 13 (16 2020), p. 4051.

[97] Z Zhou et al. "LED chip-on-board package with high colour rendering index and high luminous efficacy". In: *Lighting Research & Technology* 50.3 (2018), pp. 482–488.

[98] Monika Chaudhary and Priyanshu Sharma. "Abdominal obesity in India: analysis of the National Family Health Survey-5 (2019–2021) data". In: *The Lancet Regional Health - Southeast Asia* 14 (July 2023), p. 100208.

[99] Kate Morse, Amanda Williams, and Jason Gardosi. "Fetal growth screening by fundal height measurement". In: *Best Practice & Research Clinical Obstetrics & Gynaecology* 23 (6 Dec. 2009), pp. 809–818.

[100] S Agarwal et al. "Birth weight patterns in rural undernourished pregnant women." In: *Indian pediatrics* 39 (3 Mar. 2002), pp. 244–53.

[101] Oliver A Bauchau and James I Craig. "Euler-Bernoulli beam theory". In: *Structural analysis*. Springer, 2009, pp. 173–221.

[102] A. Bekmurzayeva et al. "Surface modification of stainless steel for biomedical applications: revisiting a century-old material". In: *Materials Science and Engineering: C* 93 (2018), pp. 1073–1089.

[103] D. Li et al. "Powder injection molding 440c stainless steel". In: *The International Journal of Advanced Manufacturing Technology* 49 (1-4 2010), pp. 105–110.

[104] M. Wu et al. "Microstructures, mechanical properties, and fracture behaviours of metal-injection moulded 17-4ph stainless steel". In: *Metals and Materials International* 21 (3 2015), pp. 531–537.

[105] S. V. Sajadifar et al. "Performance of thermo-mechanically processed aa7075 alloy at elevated temperatures—from microstructure to mechanical properties". In: *Metals* 10 (7 2020), p. 884.

[106] P. Zhang et al. "Evaluation of low cycle fatigue performance of selective laser melted titanium alloy ti–6al–4v". In: *Metals* 9 (10 2019), p. 1041.

[107] Y. S. A. Jabbari. "Physico-mechanical properties and prosthodontic applications of co-cr dental alloys: a review of the literature". In: *The Journal of Advanced Prosthodontics* 6 (2 2014), p. 138.

[108] HJ Rack and David Kalish. "The strength, fracture toughness, and low cycle fatigue behavior of 17-4 PH stainless steel". In: *Metallurgical and Materials Transactions B* 5 (1974), pp. 1595–1605.

[109] A. Ambroziak, M. T. Solarczyk, and A. Biegus. "Numerical and analytical investigation of aluminium bracket strengthening". In: *Archives of Civil Engineering* 64 (2 2018), pp. 37–54.

[110] Nagendra G Tanikella, Ben Wittbrodt, and Joshua M Pearce. "Tensile strength of commercial polymer materials for fused filament fabrication 3D printing". In: *Additive Manufacturing* 15 (2017), pp. 40–47.

[111] S. Hasçelik and S. Özerinç. "Mechanical properties of nylon parts produced by fused deposition modelling". In: *International Journal of Modern Manufacturing Technologies* 13 (2 2021), pp. 34–38.

[112] Ruben Bayu Kristiawan et al. "A review on the fused deposition modeling (FDM) 3D printing: Filament processing, materials, and printing parameters". In: *Open Engineering* 11.1 (2021), pp. 639–649.

[113] I. Farina et al. "High-performance nylon-6 sustainable filaments for additive manufacturing". In: *Materials* 12 (23 2019), p. 3955.

[114] S. Gomez et al. "Impact of maturity stages, shrink-wrap packaging and storage temperature on shelf life and quality of pineapple fruit". In: *Journal of Horticultural Research* 31 (1 2023), pp. 35–46.

[115] A. Bardelcik and M. J. Worswick. "The effect of element formulation on the prediction of boost effects in numerical tube bending". In: *AIP Conference Proceedings* (2005).

[116] D. A. Oliveira and M. J. Worswick. "Tube bending and hydroforming of aluminium alloy s-rails". In: *International Journal of Material Forming* 2 (3 2009), pp. 197–215.

[117] F. Huang, Y. Li, and J. Liang. "Study on the forming limit of rectangular-ribbed profile (□-shaped section) in rotary bending with flexible core die". In: *Proceedings of the Institution of Mechanical Engineers, Part B: Journal of Engineering Manufacture* 237 (3 2022), pp. 353–363.

[118] Matteo Strano. "Automatic tooling design for rotary draw bending of tubes". In: *The International Journal of Advanced Manufacturing Technology* 26 (2005), pp. 733–740.

[119] Donald G Dansereau et al. "A wide-field-of-view monocentric light field camera". In: *Proceedings of the IEEE conference on computer vision and pattern recognition*. 2017, pp. 5048–5057.

[120] S. Ledesma et al. "Artificial intelligence to design a mask insensible to the distance from the camera to the scene objects". In: *IEEE Access* 7 (2019), pp. 79934–79943.

[121] Ken Parulski et al. "Creation and evolution of ISO 12233, the international standard for measuring digital camera resolution". In: *Electronic Imaging* 34 (2022), pp. 1–7.

[122] Dietman Wueller. "Standardization of Image Quality Analysis – ISO 19264". In: *Image Engineering* 10 (2017), pp. 1–6.

[123] Norman Koren. "Compensating MTF Measurements for Chart Quality Limitations". In: *Electronic Imaging* 10 (2019), pp. 305–1.

[124] M. A. Azam et al. "Smoke removal and image enhancement of laparoscopic images by an artificial multi-exposure image fusion method". In: *Soft Computing* 26 (16 2022), pp. 8003–8015.

[125] Ryohei Miyazaki and Sumio Hoka. "What is the predictor of the intraoperative body temperature in abdominal surgery?" In: *Journal of anesthesia* 33 (2019), pp. 67–73.

[126] Camelia Cerbu and Horatio Teodorescu-Draghicescu. "Aspects on modelling the mechanical behaviour of aluminium alloys with different heat treatments". In: *Journal of Computational and Applied Mechanics* 12 (2 2017), pp. 85–98.

[127] A. Arti, A. Nagar, and N. Nidhi. "Morphometric ct- scan study of abdominal aorta". In: *International Journal of Health Sciences* (2022), pp. 4889–4896.

[128] L. Lyu et al. "Effects of inner muscle resistance exercise on stress urinary incontinence: a randomized clinical controlled trial". In: *Journal of Physical Therapy Science* 33 (10 2021), pp. 748–752.